

DEVELOPMENT OF UNSTEADY MODELS FOR FLAPPING WINGS'
CONTROLLER DESIGN APPROACH

A THESIS SUBMITTED TO
THE GRADUATE SCHOOL OF NATURAL AND APPLIED SCIENCES
OF
MIDDLE EAST TECHNICAL UNIVERSITY

BY

FİLİZ ORMANCI

IN PARTIAL FULLFILLMENT OF THE REQUIREMENTS
FOR
THE DEGREE OF MASTER OF SCIENCE
IN
AEROSPACE ENGINEERING

FEBRUARY 2016

Approval of the thesis:

**DEVELOPMENT OF UNSTEADY MODELS FOR FLAPPING WINGS'
CONTROLLER DESIGN APPROACH**

submitted by **FİLİZ ORMANCI** in partial fulfillment of the requirements for the degree of **Master of Science in Aerospace Engineering Department, Middle East Technical University** by,

Prof. Dr. Gülbin Dural Ünver _____
Director, Graduate School of **Natural and Applied Sciences**

Prof. Dr. Ozan Tekinalp _____
Head of Department, **Aerospace Engineering**

Assoc. Prof Dr. Dilek Funda Kurtuluş _____
Supervisor, **Aerospace Engineering Dept., METU**

Assist. Prof Dr. Kutluk Bilge Arıkan _____
Co-supervisor, **Dept. of Mechatronics Engineering, Atılım University**

Examining Committee Members:

Prof. Dr. Ozan Tekinalp _____
Aerospace Engineering Dept., METU

Assoc. Prof Dr. Dilek Funda Kurtuluş _____
Aerospace Engineering Dept., METU

Assist. Prof. Dr. Kutluk Bilge Arıkan _____
Dept of Mechatronics Engineering, Atılım University

Assoc. Prof. Dr. Serhat Çakır _____
Dept. of Physics, METU

Assist. Prof. Dr. Nilay Sezer Uzol _____
Aerospace Engineering Dept., METU

Date: 03.02.2016

I hereby declare that all information in this document has been obtained and presented in accordance with academic rules and ethical conduct. I also declare that, as required by these rules and conduct, I have fully cited and referenced all material and results that are not original to this work.

Name, Last Name: Filiz ORMANCI

Signature:

ABSTRACT

DEVELOPMENT OF UNSTEADY MODELS FOR FLAPPING WINGS' CONTROLLER DESIGN APPROACH

Ormancı, Filiz

M.Sc., Department of Aerospace Engineering

Supervisor: Assoc. Prof. Dr. Dilek Funda Kurtuluş

Co-Supervisor: Assist. Prof. Dr. Kutluk Bilge Arıkan

February 2016, 112 pages

Among a wide variety of micro air vehicles (MAV) due to their sizes, shapes, mechanisms and remoting technique; insect scaled flapping wing vehicles offer potential advantages like; higher agility for collision avoidance by rapid maneuvering compared to fixed wing MAVs, less noise compared to rotary wing MAVs, number of similar species in nature to imitate while modeling. Therefore, they are mainly in favor for defense applications.

Main scope of the thesis is to develop an unsteady model capable of calculating aerodynamic forces and moments for insect flight. Additionally, the total forces and moments are calculated at the body center of mass by rigid body dynamics equations. By this way, during the motion of the wings, the instantaneous angle and angular acceleration of the flapping body is found. These values are used in control applications to stabilize the system.

Body maneuvers are possible when right and left wings are moving with different input frequencies and amplitudes. Different cases of time dependent wing motions which are sweeping, heaving and pitching can be tested by the current analytical

model. In this thesis, after analytical modelling, both a testing apparatus for analyzing only roll attitude and for analyzing all rotational body dynamics are designed. These wing systems can be used to test the model for real-time control applications.

Keywords: Analytical Model for Flapping Wings, Unsteady Panel Method, Micro Aerial Vehicles, Attitude Control Insect Flight

ÖZ

ÇIRPAN KANAT KONTROL SİSTEMİ İÇİN GELİŞTİRİLMİŞ ZAMANA BAĞLI ANATİLİK MODEL TASARIMLARI

Ormancı, Filiz

Yüksek Lisans, Havacılık ve Uzay Mühendisliği Bölümü

Tez Yöneticisi: Doç. Dr. Dilek Funda Kurtuluş

Ortak Tez Yöneticisi: Yrd. Doç. Dr. Kutluk Bilge Arıkan

Şubat 2016, 112 sayfa

Mikro hava araçları boyutlarına, şekillerine, mekanizma tasarımlarına ve kontrol tekniklerine göre çeşitlilik göstermektedir. Bunlar arasında çırpan kanatlı mikro hava araçları birçok avantaja sahiptir, örneğin sabit kanatlı mikro hava araçlarına göre daha hızlı manevra kabiliyetine sahip, döner kanatlı mikro araçlara göre ise daha az sesle çalışan bu mekanizmalar için bir diğer avantaj, model tasarımı yapılırken doğada esinlenecek birçok benzer tür olmasıdır. Bu sayede savunma sanayisi için önem taşıyan araçlar olmuşlardır.

Bu çalışmanın asıl amacı; mikro boyuttaki çırpan kanat sistemi için kanadın hareketinden dolayı oluşan kuvvet ve momentleri hesaplamaktır. Buna ek olarak katı cisim dinamiği denklemlerine göre gövde hareket merkezindeki toplam kuvvet ve momentler hesaplanır. Böylece kanat hareketi boyunca anlık açı ve açısal ivme değerlerine ulaşılır. Bu değerler kontrol uygulamalarında gövdeyi kararlı bir harekete ulaştırmak için kullanılır.

Sağ ve sol kanada farklı hareket girdileri verilmesiyle gövdenin manevra yapması sağlanır, yalnız bu durumda gövde hareketi kararsız hale gelecektir. Çırpma, süpürme

ve yunuslama gibi kanadın farklı hareket türleri bu çalışmadaki analitik model ile test edilebilir. Bu tez kapsamında hem sadece yalpalama hareketi hem de gövdenin 3-Dönme eksenini etrafındaki hareketini incelemek amacıyla 2 test düzeneği tasarlanmıştır. Bu test düzenekleri analitik modelin gerçek zamanlı gövde yönelim kontrolünü test etmek için kullanılabilir.

Anahtar Kelimeler: Çırpan Kanat Analitik Modeli, Zamana Bağlı Panel Metodu, Mikro Hava Araçları, Çırpan Kanat Gövde Yönelim Kontrolü

To anyone who needs☺

ACKNOWLEDGEMENTS

I would like to state my deepest gratitude and also my respect to my supervisor, Assoc. Prof. Dr. Dilek Funda Kurtuluş for her guidance, support and valuable suggestions in every step of my study. Her motivation and attitude have always encouraged me to work harder. I would also thank to my co-supervisor, Assoc. Prof. Dr. Kutluk Bilge Arıkan for his assistive suggestions throughout my thesis.

I also thank my jury members Prof. Dr. Ozan Tekinalp, Assist. Prof. Dr. Nilay Sezer Uzol and Assoc. Prof. Dr. Serhat Çakır for reviewing my thesis.

It is my pleasure to express my special thanks to financial support of the National and Scientific Technological Council of Turkey, 1001 Program, Project 213M327. Also this study was supported by TUBA-GEBIP award 2012-18.

I would like to thank my friends from METU Aerospace Engineering and HAVELSAN Inc. who always keep me motivated to my work when something goes wrong in my code or my calculations.

Specially, I owe my thanks to Özgün Dülger, Yücel Çımtay, Metehan Yayla and Mustafa Batuhan Akıncı for their helps with their detailed knowledge of the computer programs that I need to use.

I am grateful to my friends, Gülay Şenol and Yudum Çömez from TUBITAK Project for sharing their results and offering an opportunity to test my model.

Additionally, the flexible work hours of HAVELSAN Inc. really helped me to plan my work on my thesis so that I can have enough time for my research.

Finally, I would like to express my deepest appreciation to my family for allowing me to realize my own potential. The greatest gift anyone has ever given me was the unconditional support that my family provided me over the years.

TABLE OF CONTENTS

ABSTRACT	v
ÖZ	vii
ACKNOWLEDGEMENTS	x
TABLE OF CONTENTS	xi
LIST OF FIGURES	xiv
LIST OF TABLES	xix
LIST OF SYMBOLS	xxi
LIST OF ABBREVIATIONS	xxiii
CHAPTERS	
1. INTRODUCTION	1
1.1 Introduction to MAVs	1
1.2 Major Objectives	1
1.3 Layout of the Thesis	2
2. LITERATURE SURVEY	3
2.1 Earlier Aerodynamic Models for Flapping Wings	3
2.2 Unsteady Panel Method	6
2.3 Control Applications	8
3. ANALYTICAL MODEL	13
3.1 Sudden Acceleration of an Airfoil	13
3.2 Different Cases of Flapping Motion	15
3.3 Unsteady Panel Method for Flapping Motion	18
3.3.1 Velocity Potentials and Velocities along Motion Directions	19
3.3.2 Kelvin Condition	23
3.3.3 Kutta Condition	24
3.3.4 Unsteady Bernoulli Equation	24
3.3.5 Unsteady Force Integration	25
4. ATTITUDE DYNAMICS OF FLAPPING BODY	27
4.1 Rotation Matrices for Left Wing	27
4.2 Rotation Matrices for Right Wing	28

5. SIMULINK MODEL	31
5.1 Wing Aerodynamics Module of Present Simulink Model	31
5.2 Rigid Body Dynamics Module of Present Simulink Model	34
6. DESIGN AND MANUFACTURING OF DYNAMICS TESTING MECHANISM	35
6.1 Solid Design for Rolling Control Mechanism.....	35
6.2 Final Design of Testing Mechanism and Manufacturing Procedure.....	38
6.3 Roll Dynamics Control Algorithm	41
7. RESULTS AND DISCUSSION	45
7.1 Basic Sweeping Model with Sudden Acceleration Algorithm.....	45
7.2 Flat Plate Airfoil Coordinates.....	48
7.3 Results for Heaving Calliphora Wing	49
7.3.1 Comparison of Force Coefficients from CFD and Simulink Model due to Heaving Frequency	50
7.3.2 Comparison of Force Coefficients from CFD and Simulink Model due to Number of Span wise Sections.....	56
7.3.3 Comparison of Force Coefficients from CFD and Simulink Model due to Hover and Forward Flight Cases.....	60
7.3.3.1 Comparison of 2-D Flow Pattern and Total Force Coefficients for Near Hover Cases of Calliphora for Second Case	62
7.3.3.2 Comparison of 2-D Flow Pattern and Total Force Coefficients for Forward Flight Cases of Calliphora for Second Case	65
7.3.3.3 Comparison of 2-D Flow Pattern and Total Force Coefficients for Near Hover Cases of Calliphora for First Case.....	67
7.3.4 Comparison of Sectional Pressure Distributions from CFD and Simulink	71
7.3.4.1 Pressure Distribution Comparison with CFD Results for 10th period data of First Case for Hover ($A=41.52^\circ$, $f=11.2\text{Hz}$).....	71
7.3.4.2 Pressure Distribution Comparison with CFD Results for 4th period data of Second Case for Hover ($A=85.90^\circ$, $f=5.85\text{Hz}$).....	78

7.3.4.3 Pressure Distribution Comparison with CFD Results for 4th period data of Second Case for Forward Flight ($A=85.90^\circ$, $f=5.85\text{Hz}$).....	84
7.4 Results for Heaving Flat Wing.....	94
7.5 Discussion	98
8. CONCLUSION.....	103
8.1 General Conclusions	103
8.2 Recommendations for Further Studies.....	104
REFERENCES.....	107

LIST OF FIGURES

Figure 2.1 Control requirements for hovering insects, hummingbirds and flapping-wing robots [30].	9
Figure 3.1 Body and Inertial Coordinates	13
Figure 3.2 Types of different Flapping Cases	15
Figure 3.3 Flapping motion kinematic definition (Flat Plate)	19
Figure 3.4 Flapping motion kinematic definition (Arbitrary Aifoil)	19
Figure 3.5 Vortex Panel – Discrete Vortex [25]	21
Figure 3.6 Wake patterns for sudden acceleration and flapping cases respectively [24]	25
Figure 5.1 For Iterator Subsystem to select parameters for current station	31
Figure 5.2 Time Iteration Flow-chart for calculation of variables due to wing kinematics and geometry	33
Figure 5.3 Rigid Body Dynamic Analysis due to different Kinematic Inputs on Flapping Wings	34
Figure 6.1 Design for roll dynamics including two symmetrical flapping mechanisms	35
Figure 6.2 Four-bar Mechanism used for Flapping System	36
Figure 6.3 Preliminary Design of mechanism and parts of the four bar mechanism	36
Figure 6.4 Roll Dynamic Testing Mechanism for Two-wing Flapping System	37
Figure 6.5 Designed Rode Types for Rotational Motion of Mechanisms	37
Figure 6.6 Spherical Bearing Assembly	38
Figure 6.7 Final Mechanism Design for examining body rotations along 3 axes using Spherical Bearing (Ball and Socket)	38
Figure 6.8 Example of a Double- Rotor Mechanism for Body Attitude Dynamics [43]	39
Figure 6.9 Plexi Parts and Bearings used in 4-bar mechanisms and Plexi Calliphora Wing	39
Figure 6.10 Servo attachment and 2-Different 4-bar types	40
Figure 6.11 Parts used in Rolling Mechanism	40

Figure 6.12 IMU attachment design.....	41
Figure 6.13 Schematic of Attitude Dynamics Control.....	43
Figure 7.1 Time dependent Circulation and Force Values for Sudden Acceleration of Flat Plate Case ($\alpha = 5^\circ, \Delta t U_\infty / c = 0.25$).....	45
Figure 7.2 Time dependent Circulation and Force Values for Periodic Sweeping of Flat Plate Case ($\alpha = 5^\circ, \Delta t U_\infty / c = 0.25$).....	46
Figure 7.3 Time Dependent Total Lift on the Wing by Periodic Sweeping Motion .	47
Figure 7.4 Total Span wise Lift Distribution by Periodic Sweeping Motion	47
Figure 7.5 Different Sections of Calliphora Wing Shape	48
Figure 7.6 Sectional Polylines defined in CFD for pressure distribution of First Case (10 th period of the motion with $A=41.52^\circ, f=11.2\text{Hz}$) (blue: 1 st half upstroke; magenta: downstroke; orange: 2 nd half upstroke)	51
Figure 7.7 Sectional Polylines defined in CFD for pressure distribution of Second Case (4 th period of the motion with $A=85.90^\circ, f=5.85\text{Hz}$) (blue: 1 st half upstroke; magenta: downstroke; orange: 2 nd half upstroke)	51
Figure 7.8 Linear Flapping Velocities of Three Different Calliphora Sections ($A=41.52^\circ, f=11.2\text{Hz}$)	52
Figure 7.9 Linear Flapping Velocities of Three Different Calliphora Sections ($A=85.90^\circ, f=5.85\text{Hz}$)	53
Figure 7.10 Comparison of Lift Coefficient for the First Case 10 th period ($A=41.52^\circ, f=11.2\text{ Hz}$) in Hover (# of span wise sections: red:11, green:5, magenta:3)	53
Figure 7.11 Comparison of Drag Coefficient for the First Case 10 th period ($A=41.52^\circ, f=11.2\text{ Hz}$) in Hover (# of span wise sections: red:11, green:5, magenta:3).....	54
Figure 7.12 Comparison of Lift Coefficient for the Second Case 4 th period ($A=85.90^\circ, f=5.85\text{Hz}$) in Hover (# of span wise sections: red:11, green:5, magenta:3)	55
Figure 7.13 Comparison of Drag Coefficient For the Second Case 4 th period ($A=85.90^\circ, f=5.85\text{Hz}$) in Hover (# of spanwise sections: red:11, green:5, magenta:3)	56
Figure 7.14 Calliphora Wing with 3 Span-wise Sections	57
Figure 7.15 Calliphora Wing with 5 Span-wise Sections	58
Figure 7.16 Calliphora Wing with 11 Span-wise Sections	59

Figure 7.17 Comparison of Lift Coefficient for the Second Case 4th period ($A=85.90^\circ$, $f=5.85\text{Hz}$) in Forward Flight ($U=-3\text{m/s}$) (# of span wise sections: red:11, green:5, magenta:3)	60
Figure 7.18 Comparison of Drag Coefficient for the Second Case 4th period ($A=85.90^\circ$, $f=5.85\text{Hz}$) in Forward Flight ($U=-3\text{m/s}$) (# of span wise sections: red:11, green:5, magenta:3)	61
Figure 7.19 Flow Pattern obtained by mid-section (blue line) of Calliphora Wing ($A=85.90^\circ$, $f=5.85\text{Hz}$, $U=0$ [m/s])	62
Figure 7.20 Flow Pattern obtained mid-section (blue line) of Calliphora Wing ($A=85.90^\circ$, $f=5.85\text{Hz}$, $U=-0.1$ [m/s])	62
Figure 7.21 Flow Pattern obtained by mid-section (blue line) of Calliphora Wing ($A=85.90^\circ$, $f=5.85\text{Hz}$, $U=-0.2$ [m/s])	63
Figure 7.22 Flow Pattern obtained by mid-section (blue line) of Calliphora Wing ($A=85.90^\circ$, $f=5.85\text{Hz}$, $U=-0.3$ [m/s])	63
Figure 7.23 Comparison of Total Lift Coefficient on Calliphora having different near hover velocities ($A=85.90^\circ$, $f=5.85\text{Hz}$) ($U=0, -0.1, -0.2, -0.3$ [m/s])	64
Figure 7.24 Comparison of Total Drag Coefficient on Calliphora having different near hover velocities ($A=85.90^\circ$, $f=5.85\text{Hz}$) ($U=0, -0.1, -0.2, -0.3$ [m/s])	64
Figure 7.25 Flow Pattern obtained by mid-section (blue line) of Calliphora Wing ($A=85.90^\circ$, $f=5.85\text{Hz}$, $U=-2$ [m/s])	65
Figure 7.26 Flow Pattern obtained by mid-section (blue line) of Calliphora Wing ($A=85.90^\circ$, $f=5.85\text{Hz}$, $U=-3$ [m/s])	65
Figure 7.27 Flow Pattern obtained by mid-section (blue line) of Calliphora Wing ($A=85.90^\circ$, $f=5.85\text{Hz}$, $U=-4$ [m/s])	66
Figure 7.28 Comparison of Total Lift Coefficient on Calliphora having different forward velocities ($A=85.90^\circ$, $f=5.85\text{Hz}$) ($U=-2, -3, -4$ [m/s])	66
Figure 7.29 Comparison of Total Drag Coefficient on Calliphora having different forward velocities ($A=85.90^\circ$, $f=5.85\text{Hz}$) ($U=-2, -3, -4$ [m/s])	67
Figure 7.30 Flow Pattern obtained by mid-section (blue line) of Calliphora Wing ($A=41.52^\circ$,	67
Figure 7.31 Flow Pattern obtained by mid-section (blue line) of Calliphora Wing ($A=41.52^\circ$, $f=11.2\text{ Hz}$, $U=-0.1$ [m/s])	68

Figure 7.32 Flow Pattern obtained by mid-section (blue line) of Calliphora Wing ($A=41.52^\circ$, $f=11.2$ Hz, $U= -0.2$ [m/s])	68
Figure 7.33 Flow Pattern obtained by mid-section (blue line) of Calliphora Wing ($A=41.52^\circ$, $f=11.2$ Hz, $U= -0.3$ [m/s])	69
Figure 7.34 Comparison of Total Lift Coefficient on Calliphora having different near hover velocities ($A=41.52^\circ$, $f=11.2$ Hz) ($U=0, -0.1, -0.2, -0.3$ [m/s])	70
Figure 7.35 Comparison of Total Drag Coefficient on Calliphora having different near hover velocities ($A=41.52^\circ$, $f=11.2$ Hz) ($U=0, -0.1, -0.2, -0.3$ [m/s])	70
Figure 7.36 Pressure Distribution Comparison at 0.905 [sec]	71
Figure 7.37 Pressure Distribution Comparison at 0.915 [sec]	72
Figure 7.38 Pressure Distribution Comparison at 0.94 [sec]	73
Figure 7.39 Pressure Distribution Comparison at 0.975 [sec]	74
Figure 7.40 Pressure Distribution Comparison at 0.965 [sec]	75
Figure 7.41 Pressure Distribution Comparison at 0.925 [sec] at CL max	76
Figure 7.42 Pressure Distribution Comparison at 0.97 [sec] at CL min.....	77
Figure 7.43 Pressure Distribution Comparison at 0.7 [sec]	78
Figure 7.44 Pressure Distribution Comparison at 0.725 [sec]	79
Figure 7.45 Pressure Distribution Comparison at 0.77 [sec] at CL max	80
Figure 7.46 Pressure Distribution Comparison at 0.81[sec]	81
Figure 7.47 Pressure Distribution Comparison at 0.83 [sec]	82
Figure 7.48 Pressure Distribution Comparison at 0.845 [sec] at CL min.....	83
Figure 7.49 Pressure Distribution Comparison at 0.68 [sec]	84
Figure 7.50 Pressure Distribution Comparison at 0.70 [sec]	85
Figure 7.51 Pressure Distribution Comparison at 0.72 [sec]	86
Figure 7.52 Pressure Distribution Comparison at 0.73 [sec]	87
Figure 7.53 Pressure Distribution Comparison at 0.75 [sec]	88
Figure 7.54 Pressure Distribution Comparison at 0.77 [sec] at CL max	89
Figure 7.55 Pressure Distribution Comparison at 0.79 [sec]	90
Figure 7.56 Pressure Distribution Comparison at 0.80 [sec]	91
Figure 7.57 Pressure Distribution Comparison at 0.82 [sec]	92
Figure 7.58 Pressure Distribution Comparison at 0.84 [sec] at CL min.....	93
Figure 7.59 Flat Wing with 3 Span-wise Sections	95

Figure 7.60 Flat Wing with 5 Span-wise Sections	95
Figure 7.61 Flat Wing with 11 Span-wise Sections	96
Figure 7.62 Comparison of Lift Coefficient for the First Case 10 th period (A=41.52 °, f=11.2 Hz) in Hover due to Span-wise Wing Shape	97
Figure 7.63 Comparison of Drag Coefficient for the First Case 10 th period (A=41.52 °, f=11.2 Hz) in Hover due to Span-wise Wing Shape	98
Figure 7.64 Iso-vorticity contours for hover visualized by CFD (green: cw, red: ccw)	99
Figure 7.65 Iso-vorticity contours for forward flight visualized by CFD (green: cw, red: ccw)	100

LIST OF TABLES

Table 3-1 Velocity Potential Equations for Flat Plate under uniform free stream and pure sweeping motion cases	16
Table 3-2 Balance of the bound circulation effect with wake circulation at each iteration step and the motion kinematics.....	17
Table 3-3 Kelvin Condition for 3 iteration steps	17
Table 3-4 Velocity Potential and velocities along X and Z directions for constant vortex distribution	20
Table 3-5 Velocity Potential and velocities along X and Z directions for linear increasing vortex distribution.....	20
Table 3-6 Velocity Potential and velocities along X and Z directions for discrete vortices	20
Table 3-7 Final Form of Expressions for Velocity Potential, and Velocities along X and Z directions for panel vortices [25]	21
Table 3-8 Final Form of Expressions for Velocity Potential, and Velocities along X and Z directions for discrete vortices [25]	22
Table 3-9 Velocity Potential and Velocity equations for panel and discrete vortices with influence coefficients [25]	22
Table 7-1 Calliphora Wing Parameters.....	50
Table 7-2 Chord values, Radial Distances and Unit lengths for Calliphora Wing for Case 1	57
Table 7-3 Chord values, Radial Distances and Unit lengths for Calliphora Wing for Case 2.....	58
Table 7-4 Chord values, Radial Distances and Unit lengths for Calliphora Wing for Case 3.....	59
Table 7-5 Flat Plate Wing Parameters	94
Table 7-6 Chord values, Radial Distances and Unit lengths for Flat Wing for Case 1	95
Table 7-7 Chord values, Radial Distances and Unit lengths for Flat Wing for Case 2	95

Table 7-8 Chord values, Radial Distances and Unit lengths for Flat Wing for Case 3
..... 96

LIST OF SYMBOLS

A	Amplitude of Horizontal Oscillation
b	Span
c	Chord
C_D	Drag Coefficient
C_L	Lift Coefficient
C_s	Side Force Coefficient
f	Frequency of Horizontal Oscillation
f_L	Flapping Angle of Left Wing
f_R	Flapping Angle of Right Wing
i	Collocation Point Counter
l	Wake Number Counter
n	Number of Panels
\hat{n}	Normal Vector to Airfoil Surface
P	Pressure
P_∞	Upstream Pressure
p_L	Pitching Angle of Left Wing
p_R	Pitching Angle of Right Wing
r	Displacement Vector
r_a	Vector from Body Axis Origin to point on airfoil surface
R_L	Rotation Matrix for Left Wing
R_R	Rotation Matrix for Right Wing
u	Wake Velocity in X direction
w	Wake Velocity in Z direction
s_L	Sweeping Angle of Left Wing
s_R	Sweeping Angle of Right Wing

U_{∞}	Upstream Velocity
α	Angle of Attack
γ	Strength and Orientation of Bound Circulation on Wing
γ_w	Strength and Orientation of Circulation in Wake
Γ_w	Wake Circulation
Γ	Bound Circulation
θ	Rotation about the Y axis
ρ	Density
Φ	Velocity Potential
Ψ	Rotation about the Z axis
ω	Body Angular Velocity Vector
Ω	Flapping Rotational Velocity
\emptyset	Rotation about the X axis
\ominus	Rotation Vector (Φ, θ, Ψ)

LIST OF ABBREVIATIONS

AOA	Angle of Attack
BC	Boundary Condition
BEM	Blade Element Method
CFD	Computational Fluid Dynamics
DOF	Degree of Freedom
IMU	Inertial Measurement Unit
LIPCA	Lightweight Piezo-composite Curved Actuator
LQR	Linear Quadratic Regulator
MAV	Micro Aerial Vehicle
METU	Middle East Technical University
PID	Proportional, Integral, Derivative
TÜBİTAK	Scientific and Technological Research Council of Turkey
ULVPC	Unsteady Lattice Vortex Panel Code

CHAPTER 1

INTRODUCTION

1.1 Introduction to MAVs

The micro-aerial vehicles (MAV) are mainly designed based on three types of lift generations; fixed, rotary and flapping wings. Since there are many examples of living species carrying a mechanism for the flapping motion, it has been mainly an experimental research area to study on by scientists. In addition to this, there are numerical methodologies for the steady state and unsteady flapping motion for the designed or imitated man-made flapping vehicles.

Developing an unsteady model for flapping wings is a main requirement for manufacturing a MAV since corrective maneuvers are needed for control part. It is still a challenge to achieve to input variable flapping, sweeping and pitching angles and velocities over the flapping cycle to obtain desired thrust and lift forces while minimizing the required power for flapping wings at realistic frequencies and amplitudes. To do this, time dependent forces and moments due to important unsteady effects have to be found.

To design a MAV with suitable kinematic inputs for the wings and stable body dynamics attitude; angles and angular velocities are controlled by feedback control system. For control systems, real-time analytic models are required which is the main aim of this study.

1.2 Major Objectives

The Major objectives of the current study are;

- To develop an unsteady model for calculation of aerodynamic forces on the wings due to different kinematic and geometric inputs.
- To obtain rigid body dynamic forces and moments at the body center of gravity along a rotation axis.
- To design a suitable symmetric double wing mechanism and body rotation mechanism for feedback control algorithms using a design tool.
- To manufacture the designed mechanisms for the future test applications.

1.3 Layout of the Thesis

In Chapter 2, the literature review of different types of analytical models and their ways of calculating aerodynamic forces for different airfoil motions are presented. Many scientists have been working on developing a time dependent models for different wing kinematics and verified their work with different tools and experiments.

Chapter 3 is about the theory of present analytic model developed. Due to kinematic and geometric inputs, 2-D analysis of wing's unsteady motion is studied. All the values are updated due to time dependent velocity inputs in 2 translation and 1 rotation dimensions. By this way, the span-wise integrated total forces due to pressure distribution acting on the wing is found.

Chapter 4 is about rigid body dynamic analysis. The time dependent total forces and moments due to two wing system are found in body center of gravity to analyze the body attitude.

Chapter 5 is about Simulink blocks used to build present model.

In Chapter 6, the solid design and manufacturing procedure of two wing testing system to be used for future applications is represented.

Finally in Chapter 7, the results of analytic model are compared with CFD results.

CHAPTER 2

LITERATURE SURVEY

2.1 Earlier Aerodynamic Models for Flapping Wings

Many scientists analyzed motion of different flying insects and birds and obtained empirical coefficients which support prescribed models. Brodsky [1] used high speed filming of a specific insect in a wind tunnel and observed the vortex pairs. He discussed shape of vortex wake structure of flow depending on wing frequency, without wing pair interaction. Vortices are produced and shed respectively during pronation and supination. Before his work, Spedding [2] had followed same procedure for bats and birds. He worked on wake of many species like jackdaw *Corvus moedula* and kestrel *Falco tinnunculus* by multiple image stereo photographs in his series of articles. He estimated the rate of momentum generated in the wake for induced power requirement from the wake measurements. He obtained significant results for unsteady models and energetic predictions for design of flapping motion. Rayner [3] postulated a vortex ring model for slow-flying birds and analyzed so called “gait change” (sharp discontinuity in wing beat kinematics during kinematic flight), gave suggestions on number of ways for power reduction. He also outlined a flight model by conversion factor on classical momentum jet theory for both insects and birds.

Early aerodynamic methodologies for blade motion includes many quasi steady models such as; momentum theory, blade element analysis, vortex wake models, hybrid models (blade element and momentum, blade element and vortex), lifting line and lifting surface (panel method) theories. Fogh [4] stated that the steady state approach does not fit properly with the natural flyers; this gives rise to research unsteady models which added mass and unsteady circulatory effects are included. However quasi steady models which are derived by steady analysis for instant time

are helpful for comparison with unsteady cases. The modeling methodologies found in literature for unsteady, 3-D motion of the wing varies based on different kinematics, boundary conditions, unsteady effects included, conservation rules and solution types.

Steady state theories are used to compute lift and drag coefficients due to difference in geometry and speed of the wing as a snapshot for an instant, such models are transformed into quasi steady models depending on wing kinematics. Blade element method (BEM) is one of the most famous approaches to calculate the lift by discretizing the wing in span-wise strips and compute summation on aerodynamic force distribution. Ellington [5] used these static conditions and assumed that the instantaneous values that are equal to steady ones in his blade element analysis. Blade element theory ignores the vorticity approach; however, the relative velocity is found by superposing heaving velocity and bound and wake induced velocities.

Momentum theory of Rankine-Froude is another quasi steady model which assumes the beating plane of flapping motion as actuator disc. Osborne [6] used this method to calculate induced velocity. Change in momentum due to acceleration of the surrounding air generates thrust to balance the weight and drag forces. In this method, flow is uniform across cross sectional “disc” area. With the contribution of Bernoulli equation, momentum theory results that vertical velocity attained in far wake is twice the velocity induced at the disc.

Hybrid momentum method is combination of Momentum theory and BEM including consideration of unsteady wake effects is another quasi steady model. Kawachi [7] developed another hybrid method which is the combination of circulation theory and BEM. Compared to classical momentum theory based on uniform induced flow over rotor disc, he divided the rotor disc in annular sections and analyzed asymmetric flow field based on momentum balance considering apparent mass effect. Azuma and Watanabe [40] applied this method for the dragonflies modifying the quasi steady models like BEM and momentum theory with the local circulation method which is previously developed for rotary wings. The effect of the periodic shed vortices are included by Theodorsen function [27].

Lifting Line theory is based on trailing edge vortices and such twisting and bending of span-wise quantities are taken into account, however, kinematic approach is weak. Betteridge and Archer [8] worked on lifting line theory with actuator disc theory to predict induced flow and optimize lift with a quasi-steady approach. Phlips [9] used lifting line theory with unsteady approach and calculated forces and power curves due to wing geometry and motion kinematics, obtained results compatible with Rayner's experimental study [3].

Lifting surface (vortex lattice/panel) method takes wing geometry and wake representation into account compared to lifting line method. Sunada et al [21] used this method on flat plate for clap-and-fling mechanisms and modified their fluid dynamic model according to sinusoidal pitching and plunging experiments in water which resulted larger forces compared to calculations due to vortex capture phenomenon.

Analytical studies on flapping wings are mainly based on sinusoidal pitch and plunge motion. Theodorsen [27] derived a function based on quasi-steady methods and he included added mass and wake effects; however, the leading edge vortex contribution and aerodynamic coupling between motions were missing. His work is based on lift and moment calculation of aileron and additional application for flutter. Garrick [26] modeled an extension to Theodorsen's theory and derived propulsive forces on oscillating thin airfoil due to harmonic plunging motion using energy conservation. He also proved that the results of frequency based model of Theodorsen fit with Wagners' [28] time based analysis due to vortex distribution in the wake generated by the arbitrary oscillations of the airfoil. Lift generation time lag for sudden accelerated airfoil due to wake effects was calculated by Wagner [28]. Küssner [39] obtained this lag due to unsteady gust effects.

Beddoes [10] performed an indicial lift model by deriving a transverse function for time dependent pitching motion. He approached the airfoil response to change in induced velocity and calculated the blade loads for arbitrary induced velocity with Duhamel Integration.

Zbikowski [11] worked on another indicial model depending on velocity potential and solution of ordinary differential equation for nonconstant free stream, and used two main techniques which are unsteady modeling of attached flow for helicopter blades and leading edge suction analogy in both time and frequency domain. Since insect scale flapping motion leads very high angle of attacks, separation of both leading and trailing edges hold key for accurate modeling. Ansari et al. [12] used conformal mapping transformations to model 2D flow around airfoil by BEM and both flow separations.

All these analytical models approaches the results for forces and moments due to motion of a wing however some of them have limited ability to model 6 DOF motion or steadiness is not at desired level. Developments show that Unsteady Panel Methods for Flapping Airfoil is one of the best ways to obtain accurate results. Panel methods are such techniques to solve incompressible potential flow equation for thick geometries. The 2D airfoil surface is divided into line segments or boundary elements and vortex sheets are placed on these panels.

2.2 Unsteady Panel Method

Smith [20] summarized the main advantages of unsteady aerodynamic panel method and compared with the quasi steady models and stated that the method includes detailed analysis on trailing wake and dynamics effects. As Vest and Katz [23] stated, this method is unique in its ability to handle a time-dependent and even deformable flapping wings. There are many studies depending on unsteady panel methods for the flapping wing motion in the literature.

Kamali and Ravesh [14] developed a computer code for unsteady panel method for the flow analysis and obtained results for design coefficients (for NACA 2410 and NACA 2412) and trailing edge wake shape for different flight conditions. Jimenez and Lopez [15] developed a computational model with Hess-Smith panel method (for NACA 4415) and used this aerodynamic model for the control mechanism. They updated the airfoil shape (coordinates of the aileron part) and feeding the control system with the forces and moments calculated for updated shape. Persson et al. [16]

compared their panel method and Navier stokes solution for the 3-D flapping wing (for $\alpha=0^\circ, 5^\circ, 10^\circ$) and emphasized the importance of supporting any inviscid model with a viscous simulation for high fidelity wing design. Anmar [17] developed a numerical method for arbitrary unsteady motion of thin airfoil, and applied for sudden change in angle of attack while airfoil is oscillating with a high frequencies and obtained influence of nonlinear wake on oscillation amplitude, wake rollup and aerodynamic forces (for NACA 0008). Mantia and Dabnichki simulated the harmonic oscillations of NACA 0012 airfoil in water and calculated the hydrodynamic forces with unsteady boundary element (panel) method. They mainly focused on added mass effect [18-19].

Smith [20] used realistic wing kinematics with 3-D panel methods including flexible wing structure by the finite element method and emphasized the importance of wake contribution for unsteady cases. Sunada et al. [21] used this method on flat plate for clap-and-fling mechanisms and modified their fluid dynamic model according to sinusoidal pitching and plunging experiments in water which resulted larger forces compared to calculations due to vortex capture phenomenon.

Vest and Katz [22-23] worked on iterative procedure for 3-D panel methods due to trailing wake shape of deforming geometries and different avian flight types and compared high and low frequency of flapping motion cases. They also developed a fluid dynamic model depending on deformable trailing edge vortices by solving the Laplace equations with the boundary conditions due to wing kinematics and combining with the Kelvin's theorem. The model was applied to wings with high advance ratios and pigeon wing (twisted) in a wind tunnel and averaged lift results matched with the experimental data within an error bound. Katz and Plotkin [24] obtained formulation for different cases of 3-D motion of flat plate wing.

Prosser [25] performed a MATLAB model for unsteady panel method with chain of functions and used NACA 0006 airfoil shape with different chord lengths (1m, 0.2m, 0.04m, the last one is compatible with MAVs). He compared the force coefficients obtained with FLUENT simulation and they match up other than a phase shift which caused by the difference between cycle-averaged and instantaneous forces.

Due to time varying 3-D wing kinematics, unsteady loads for various angular motion frequencies can be obtained by the unsteady panel method. Choosing the suitable coordinate system for calculations is very important for modeling the input motion and corresponding force dynamics. Positions, linear and angular velocities and time dependent derivations are defined due to new coordinate systems, and updated during the motion.

In this thesis, first the analytic model is developed, which is based on trailing edge wake vortices whose effect is balanced by the influence of bound vortex on the wing at a position at any time. For the incompressible flow, the continuity equation is time independent; therefore, there is a need for time dependent boundary conditions to model unsteady aerodynamics. Two main boundary conditions for the model are; zero normal velocity at body surface and no flow sufficiently far away from the body. In addition to these, Kelvin and Kutta conditions provide two more equations to obtain wake circulation. When all these coordinate transformations, formulations and boundary conditions are used with the suitable kinematic description of any motion of wing, the resultant vortex distributions can be obtained. By this way, pressure distribution, lift and drag forces are found.

Since the first model used only one collocation point on the chord, results do not fulfill the expectations. Because of this, a second model is developed which is based on Unsteady Panel Approach using many airfoil coordinates and placing collocation points in the middle of each two coordinate points over the surface.

2.3 Control Applications

The natural fliers have their own biological stabilization ability; for example, the tiny wasp stabilizes itself with the viscous drag on its body, extended long legs help the mosquito fly stable and woolly aphid has a fibrous coat for this purpose. In addition to these, Robotic fliers have different stabilization strategies: Harvard robot has external stabilization using wire guides; Cornell robot flies stable with its large sails; Mentor robot has sensory feedback control. Damping time scale and reaction time

needed analysis for flight stabilization were performed for these species and mechanisms [30].

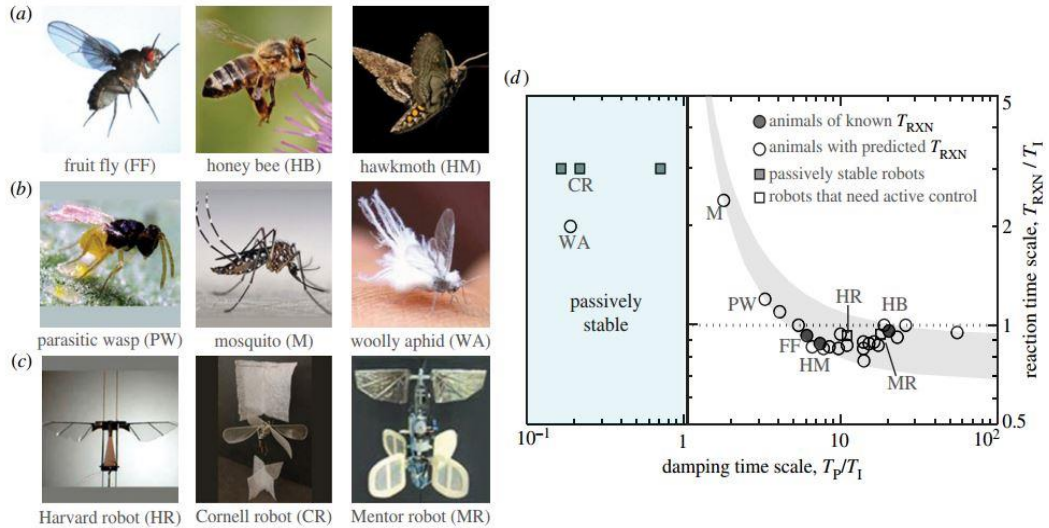


Figure 2.1 Control requirements for hovering insects, hummingbirds and flapping-wing robots [30].

For both natural fliers and micro flapping vehicles generating lift force sufficient for body mass is not enough, but they need a balanced forces and torques during their flying period. Sensory neurons and motor neurons of the flight muscles of flying animals overcome with this problem [31]. However, robotic fliers have trouble in their balance without passive stabilization with a body drag or active control with a sufficiently rapid reaction [30].

Teoh et al. [33] worked on vertical take-off stabilization of the Harvard RoboBee, which is an insect-scale flapping-wing robot using the piezo-actuators having 230 V at RoboBee's resonant frequency (105 Hz) to accelerate upward and 20mm damper. Their (proportional derivative) PD controller gathers the position information by a serial port and calculates feedback power at 10 KHz.

Cheng et al. [31] obtained mathematical model for Calliphora like flying prototype and used analytical estimations for the stability derivatives and control derivatives using quasi-steady aerodynamics. They worked on closed loop control feedback algorithm for wing asymmetry and generated torque along roll, pitch, and yaw axes,

considering the body in 3 ellipsoid rigid parts and calculating their moment of inertia.

Chang et al. [32] provided limit values for sensing rate and time delay between sensing and feedback motion. Their stabilization of flapping flight pitching motion is based on discrete time delayed linear control algorithm in the nonlinear regime without any prediction.

Fearing et al. [34] modeled a micromechanical flying insect and using force sensors mounted on the wing spars and modifying the wing stroke patterns by closed loop wing controllers for reaction to wing forces. They used “daughter cards” which includes magnetic sensors, gyroscope and accelerometer. Yan et al. [37] developed closed loop control algorithm for Berkeley MFI design project with the optical position sensors.

Similarly, Karásek et al. [35] developed a control mechanism to generate moments for attitude stabilization of their hummingbird prototype modulating wing twist, flapping amplitude and mean wing position. They stated that increasing the wing motion amplitude produces roll moment, moving wing offset forward backward creates pitch moment and changing mean wing position along opposite directions results in yaw moment on the body.

Orlowski et al. [36] developed an open loop pitch control of a flapping wing micro-air vehicle using a tail that is able to rotate about its pitch axis and control mass that is able to translate in longitudinal and vertical directions which provide additional generalized coordinates and derivatives for the model.

Thomson et al. [44] developed 3 channel PID controller in LabVIEW and used on a National Instruments (NI) CompactRIO Real-Time Controller (cRIO-9002) for flapping mechanism to track desired roll, pitch, yaw angles and tuned the control gains with experimental values. Duan and Li [45] developed a novel nonlinear control method for flapping body attitude control based on Active Disturbance Rejection Control (ADRC) and used nonlinear PD controller with rotational accelerometers. Lindsey et al [46] controlled altitude, roll and pitch attitude independently in a PID controller by changing the flapping amplitudes of left and

right wings for rig and un-rig cases for piezo actuated flapping body and they also included the Gaussian Noise. They additionally studied indirect yaw control with pitch and roll angles.

Deng et al [47] used LQR strategy for three mean torques and mean lift by four single input- single output subsystems and achieved stabilization despite the sensor noises. They also used pseudo inverse method to compute inputs of actuators for trajectory tracking. Bhatia et al. [48] used controller based on LQR and determine the control inputs as wing kinematic inputs with external disturbances (gust effect) for a flapping wing MAV.

In addition, Zhang et al. [49] stated that PID methods precise to track the trajectories for large control inputs, while LQR strategy overcomes with large flapping amplitudes. They designed both PID and LQR controllers and implemented on a 72 MHz cortex M3 board.

There are two main challenges for controller design; one is coupled motions and the other is nonlinear terms in aerodynamic model; however, first can be solved by dynamic inversion or computed torque control, and second can be solved by adaptive approximation techniques.

All these developments in stabilization and control mechanism of attitude dynamics for flapping micro air vehicles set light to the future developments. However, there are still many challenges to overcome which are power storage, compact hardware, light materials for construction, efficient mechanism design and to understand the unsteady aerodynamics of flapping motion better. Therefore control algorithms and analytic unsteady models support the developments of each other. [33]

CHAPTER 3

ANALYTICAL MODEL

3.1 Sudden Acceleration of an Airfoil

Considering time dependent motions of the wing in 6 DOF, different modifications of the velocity potential equation are possible to obtain. Some of them are given by Katz and Plotkin [24]. They also give detailed solution for sudden acceleration case with a single collocation point model.

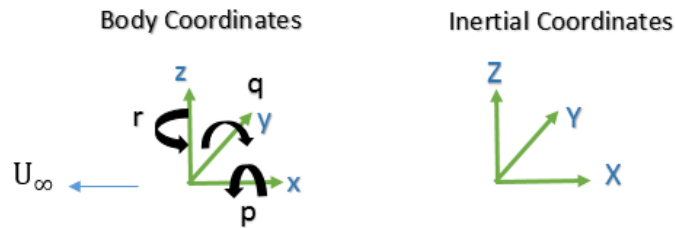


Figure 3.1 Body and Inertial Coordinates

The body fixed frame is shown as (x, y, z) when the inertial frame is shown as (X, Y, Z) as shown in Figure 3.1. At starting point they coincide and for the case $t > 0$ the location of (x, y, z) with respect to the inertial frame is shown as $R_0(t)$ and its orientation is shown as $\Theta(t)$.

$$R_0(t) = (X_0, Y_0, Z_0) \quad (3.1)$$

$$\Theta(t) = (\Phi, \theta, \Psi) \quad (3.2)$$

The calculation of the wing forces due to trailing edge vortices given in the Katz and Plotkin's book is repeated by MATLAB iterative code and the result for sudden acceleration of flat plate are found as the results given in the book. In this model the bound circulation is calculated on the wing just for one collocation point.

For this case the x component of the free-stream velocity is U_∞ , therefore the location vector gets the form $R_0(t) = (X_0, Y_0, Z_0) = (-U_\infty t, 0, 0)$. The wing motion and the freestream velocity are opposite to each other, X component of wing velocity is defined as $-U_\infty$, and since there is no rotation, orientation vector gets the form $\Theta(t)=(0,0,0)$.

The wake around the wing is assumed as inviscid, incompressible and irrotational; therefore the continuity equation is;

$$\nabla^2 \Phi = 0 \quad (\Phi (X, Y, Z)) \quad (3.3)$$

Two boundary condition used for this approach is; normal velocity being zero at wing surface and wake rate approaching zero too far from the wing. These conditions are represented as;

$$(\nabla \Phi + \mathbf{v}) \cdot \mathbf{n} = 0 \quad (3.4)$$

$$\lim_{|\mathbf{R}-\mathbf{R}_0| \rightarrow \infty} \nabla \Phi = 0, \quad \mathbf{R}=(\mathbf{X}, \mathbf{Y}, \mathbf{Z}) \quad (3.5)$$

In addition to these, due to Kelvin condition, the angular momentum is conserved in a potential wake field. Hence, the circulation remains constant for the circle enclosing the wing, and the wake is conserved.

$$\frac{d\Gamma}{dt} = 0 \quad (\text{for any } t) \quad (3.6)$$

The kinematic velocity of the wake due to wing motion is expressed as;

$$\mathbf{v} = -[\mathbf{V}_0 + \mathbf{v}_{\text{rel}} + \boldsymbol{\Omega} \times \mathbf{r}] \quad (3.7)$$

Here V_0 is velocity of the origin of the x, y, z system $(\dot{X}_0, \dot{Y}_0, \dot{Z}_0)$, r is position vector (x, y, z) and Ω is vector of angular velocities around x, y, z axes (p, q, r). Surface normal vector $\mathbf{n}=\mathbf{n}(X, Y, Z, t)$ is changing time dependently. And the relative velocity defined in body coordinates (x, y, z) is expressed as $\mathbf{v}_{\text{rel}}=(\dot{x}, \dot{y}, \dot{z})$, and included in the kinematic velocity [24].

Sudden acceleration of the flat plate case is a good starting point for studying unsteady phenomena. Basically, the model based on the influence coefficients for circulation terms for one collocation point was most basic form of panel methods.

The iterative code is obtained for periodic sweeping motion using MATLAB. The bound circulation value at any time on the airfoil is balanced by the wake circulations at $\frac{3}{4}$ of chord as in sudden acceleration case. Other cases like sinusoidal pitching and plunging motions can be defined kinematically and used in the unsteady boundary condition equations.

3.2 Different Cases of Flapping Motion

There are 3 main unsteady motion of the wing and sudden effects like gust effect as illustrated as Figure 3.2.

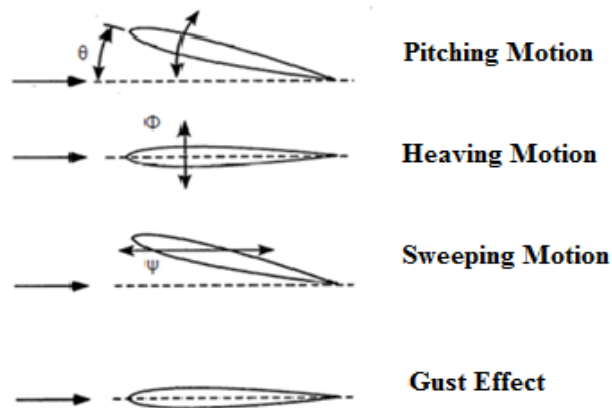


Figure 3.2 Types of different Flapping Cases

First the kinematic description of motion is obtained by determining; vector between body fixed frame and inertial frame. $(R_0(t) = (X_0, Y_0, Z_0))$, instantaneous orientation $(\Theta(t) = (\Phi, \theta, \Psi))$ and angular velocities $(\dot{\Theta}(t) = (p, q, r))$.

Due to continuity equation for incompressible, irrotational and inviscid flow (Equation 3.3) and boundary condition of zero normal flow on the wing surface

(Equation 3.4) and coordinate transformation equations, the resultant expression for airfoil motion can be obtained

Boundary conditions are updated due to these kinematics including components of unsteady motion. By this way, it is possible to model pure plunging, sweeping and pitching motions, and coupled form of these motions. Moreover, a translational motion of the airfoil is added by the linear velocity of total system.

Table 3-1 Velocity Potential Equations for Flat Plate under uniform free stream and pure sweeping motion cases

Flat Plate under uniform free stream	Flat Plate under pure sweeping motion
$\mathbf{V}_0 = (\dot{X}_0, \dot{Y}_0, \dot{Z}_0) = (-U_\infty, 0, 0)$	$\mathbf{V}_0 = (0, 0, 0)$
$\boldsymbol{\Omega}=0$ (no rotation)	$\boldsymbol{\Omega}=(0,0, \dot{\Psi})$
$\mathbf{n}=(\sin\alpha,0,\cos\alpha)$	$\mathbf{n}=(\sin\alpha,0,\cos\alpha)$
$(\nabla\Phi - \mathbf{V}_0 - \mathbf{v}_{rel} - \boldsymbol{\Omega} \times \mathbf{r}) \cdot \mathbf{n} = (\frac{\partial\Phi}{\partial x} + U_\infty, 0, \frac{\partial\Phi}{\partial z}) \cdot (\sin\alpha, 0, \cos\alpha) = 0$	$(\nabla\Phi - \mathbf{V}_0 - \mathbf{v}_{rel} - \boldsymbol{\Omega} \times \mathbf{r}) \cdot \mathbf{n} = (\frac{\partial\Phi}{\partial x} + \dot{\Psi}y, \frac{\partial\Phi}{\partial y} - \dot{\Psi}x, \frac{\partial\Phi}{\partial z}) \cdot (\sin\alpha, 0, \cos\alpha) = 0$
$\frac{\partial\Phi}{\partial z} = -(U_\infty + \frac{\partial\Phi}{\partial x}) \tan\alpha \approx -U_\infty \alpha$	$\frac{\partial\Phi}{\partial z} = (\dot{\Psi}y + \frac{\partial\Phi}{\partial x}) \tan\alpha$

Developing an appropriate wake model is the second part after kinematic description of the system. In the wake analysis, it is predicted that downwash velocity due to bound circulation at a chord-wise position of airfoil, downwash velocity of the wake circulation and the velocity component of the kinematic motion are balanced depending on their directions for any time instant. The chord-wise position is taken as $\frac{3}{4}$ chord as previously performed by many scientists [24-25].

At each iteration time, a new wake vortex is formed and previous one is remaining far apart since there is a translational velocity of flat plate for the first case. Similarly, for the second case, due to linear velocity which is angular sweeping velocity times the radius of rotation, distances of each wake to the reference point, and their corresponding induced velocities changes. Table 3-1 is giving the expressions for flat

plate with uniform freestream and pure sweeping cases and Table 3-2 is illustrating boundary condition equation the first three iteration steps.

Moreover, according to Kelvin Condition angular momentum due to circulation is conserved. ($\frac{d\Gamma}{dt}=0$). This supplies second equation for each time step to obtain two unknowns which are bound circulation and wake circulation. Table 3-3 is illustrating Kelvin Condition equation the first three iteration steps.

Table 3-2 Balance of the bound circulation effect with wake circulation at each iteration step and the motion kinematics

Iteration Time	Boundary condition
t_1	$\frac{-\Gamma(t_1)}{2\pi(c/2)} + \frac{\Gamma_{W1}}{2\pi[(c/4) + (U_\infty \Delta t / 2)]} = -U_\infty \alpha$ $(\mathbf{w}_b + \mathbf{w}_w = -\mathbf{U}_\infty \alpha)$
t_2	$\frac{-\Gamma(t_2)}{2\pi(c/2)} + \frac{\Gamma_{W2}}{2\pi[(c/4) + (U_\infty \Delta t / 2)]} + \frac{\Gamma_{W1}}{2\pi[(c/4) + (U_\infty 3\Delta t / 2)]} = -U_\infty \alpha$
t_3	$\frac{-\Gamma(t_3)}{2\pi(c/2)} + \frac{\Gamma_{W3}}{2\pi[(c/4) + (U_\infty \Delta t / 2)]} + \frac{\Gamma_{W2}}{2\pi[(c/4) + (U_\infty 3\Delta t / 2)]} + \frac{\Gamma_{W1}}{2\pi[(c/4) + (U_\infty 5\Delta t / 2)]} = -U_\infty \alpha$

Table 3-3 Kelvin Condition for 3 iteration steps

Iteration Time	Kelvin Condition
t_1	$\frac{d\Gamma}{dt} = \Gamma(t_1) + \Gamma_{W1} = 0$
t_2	$\Gamma(t_2) + \Gamma_{W2} + \Gamma_{W1} = 0$
t_3	$\Gamma(t_3) + \Gamma_{W3} + \Gamma_{W2} + \Gamma_{W1} = 0$

For the pure sweeping case, the velocity U_∞ is replaced with time derivative of harmonically changing sweeping angle multiplied by radius of rotation. Previously constant linear velocity in sudden acceleration case is now time dependent.

A point to consider here is that the angle of attack for pure sweeping case is constant during the motion. That is, the angle is positive when going to one way and negative when turning back.

Solving Boundary Condition and Kelvin Condition Equations for two unknowns ($\Gamma(t_i), \Gamma_{Wi}$) at each step with the additional wake circulation for each iteration, unsteady bound circulation on the airfoil is obtained.

The lift and drag forces can be found by the following formulas;

$$\mathbf{L} = \rho \left[\mathbf{U}_\infty \Gamma(t) + \frac{\partial \Gamma(t)}{\partial t} * c \right] \quad (3.8)$$

$$\mathbf{D} = \rho \left[\mathbf{w}_w(x, t) \Gamma(t) + \frac{\partial \Gamma(t)}{\partial t} * c * \alpha \right] \quad (3.9)$$

Although this approach gives insight to unsteady analytic modeling, it failed to satisfy the expectations since only one collocation point is not enough for different airfoil geometries. Therefore, Panel Method analysis took its place to overcome these problems.

3.3 Unsteady Panel Method for Flapping Motion

Similar to the previous algorithm, first the wing motion must be kinematically defined as in Figure 3.3.

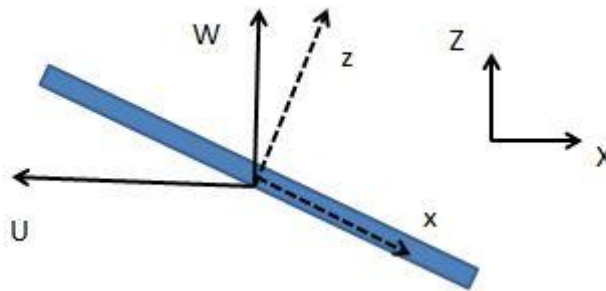


Figure 3.3 Flapping motion kinematic definition (Flat Plate)

Similarly for the wings with different profiles, we can calculate all the updated values of variables in distributed manner as illustrated in Figure 3.4.

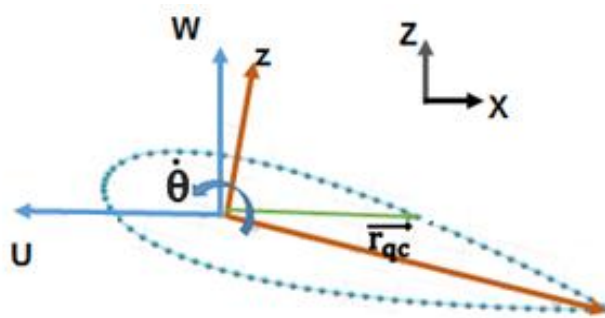


Figure 3.4 Flapping motion kinematic definition (Arbitrary Airfoil)

Katz and Plotkin [24] obtained the expressions for velocity potential, and the velocities along X and Z directions for sink, doublet and vortex distributions or their combinations. In this approach, constant and linear increasing vortex distribution expressions are used and they are given in the Tables 3-4, 3-5 and 3-6.

3.3.1 Velocity Potentials and Velocities along Motion Directions

Table 3-4 and 3-5 show the velocity potential and velocities along X and Y directions for constant and linear increasing cases for vortex distributions.

Table 3-4 Velocity Potential and velocities along X and Z directions for constant vortex distribution

	Constant Vortex Distribution
Vortex Distribution	$\gamma(x) = \gamma$
Velocity Potential	$\Phi = -\frac{\gamma}{2\pi} \int_{x_1}^{x_2} \tan^{-1} \frac{z}{x - x_0} dx_0$
Velocity along X	$u = \frac{\gamma}{2\pi} \int_{x_1}^{x_2} \tan^{-1} \frac{z}{(x - x_0)^2 + z^2} dx_0$
Velocity along Z	$w = -\frac{\gamma}{2\pi} \int_{x_1}^{x_2} \tan^{-1} \frac{x - x_0}{(x - x_0)^2 + z^2} dx_0$

Table 3-5 Velocity Potential and velocities along X and Z directions for linear increasing vortex distribution

	Linear increasing Vortex Distribution
Vortex Distribution	$\gamma(x) = \gamma_1 * x, \gamma_1 : \text{const}$
Velocity Potential	$\Phi = -\frac{\gamma}{2\pi} \int_{x_1}^{x_2} x_0 * \tan^{-1} \frac{z}{x - x_0} dx_0$
Velocity along X	$u = \frac{\gamma}{2\pi} \int_{x_1}^{x_2} \tan^{-1} \frac{x_0 * z}{(x - x_0)^2 + z^2} dx_0$
Velocity along Z	$w = -\frac{\gamma}{2\pi} \int_{x_1}^{x_2} \tan^{-1} \frac{x_0 * (x - x_0)}{(x - x_0)^2 + z^2} dx_0$

And also for the discrete vortices they are formulized as in the Table 3-6.

Table 3-6 Velocity Potential and velocities along X and Z directions for discrete vortices

$\Phi = -\frac{\gamma}{2\pi} \tan^{-1} \frac{Z - Z_0}{X - X_0}$
$u = \frac{\gamma}{2\pi} \frac{Z - Z_0}{(X - X_0)^2 + (Z - Z_0)^2}$

$$w = -\frac{\gamma}{2\pi} \frac{X - X_0}{(X - X_0)^2 + (Z - Z_0)^2}$$

Prosser [25] defined the vortex distribution as; $\gamma(x) = \gamma_0 + \gamma_1 * x$, and obtained integrals which can be derived by using constant and linear increasing forms of the expressions of velocity potential and velocities.

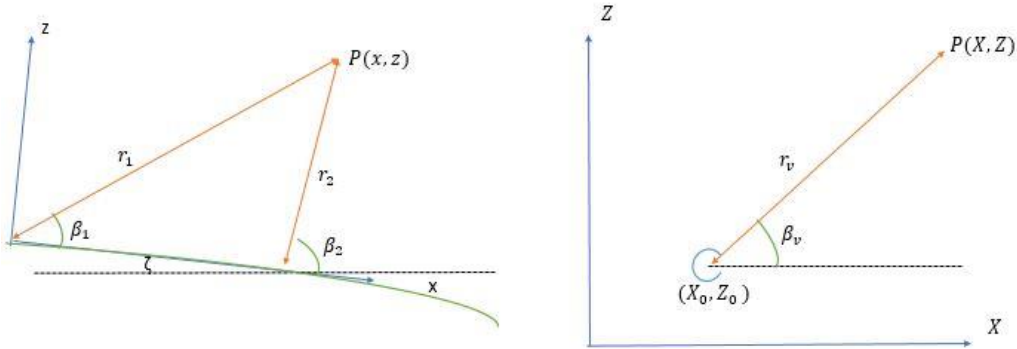


Figure 3.5 Vortex Panel – Discrete Vortex [25]

According to these the resultant equations for the panel vortices and the discrete vortices get the form as in Tables 3-7 and 3-8;

Table 3-7 Final Form of Expressions for Velocity Potential, and Velocities along X and Z directions for panel vortices [25]

$\Phi_p = -\frac{\gamma_j}{2\pi} \left(\left[x * \beta_1 - (x - d)\beta_2 + z \ln \left(\frac{r_1}{r_2} \right) \right] - \frac{1}{d} \left[xz \ln \left(\frac{r_1}{r_2} \right) - \frac{zd}{2} + \frac{x^2 - z^2}{2} \beta_1 - \frac{x^2 - z^2 - d^2}{2} \beta_2 \right] \right) - \frac{\gamma_{j-1}}{2\pi} \left(xz \ln \left(\frac{r_1}{r_2} \right) - \frac{zd}{2} + \frac{x^2 + z^2}{2} \beta_1 - \frac{x^2 - z^2 - d^2}{2} \beta_2 \right)$
$u_p = -\frac{\gamma_j}{2\pi d} \left[z \ln \left(\frac{r_2}{r_1} \right) + (x - d)(\beta_2 - \beta_1) \right] + \frac{\gamma_{j+1}}{2\pi d} \left[z \ln \left(\frac{r_2}{r_1} \right) + x(\beta_2 - \beta_1) \right]$
$w_p = -\frac{\gamma_j}{2\pi d} \left[(x - d) \ln \left(\frac{r_2}{r_1} \right) - d + z(\beta_2 - \beta_1) \right] + \frac{\gamma_{j+1}}{2\pi d} \left[x \ln \left(\frac{r_2}{r_1} \right) + d - z(\beta_2 - \beta_1) \right]$

Table 3-8 Final Form of Expressions for Velocity Potential, and Velocities along X and Z directions for discrete vortices [25]

$\Phi_d = -\frac{\gamma}{2\pi} \tan^{-1} \beta_v$
$u_d = \frac{\gamma}{2\pi} \left[\frac{z - z_0}{r_v^2} \right]$
$w_d = -\frac{\gamma}{2\pi} \left[\frac{x - x_0}{r_v^2} \right]$

As seen from Tables 3.7 and 3.8, these equations are linear equations in terms of vortex values. They can be represented by constant coefficients as given by Prosser [25] (Table 3-9);

Table 3-9 Velocity Potential and Velocity equations for panel and discrete vortices with influence coefficients [25]

$u_p = a_p \gamma_j + b_p \gamma_{j+1}$	$u_d = e \gamma$
$w_p = c_p \gamma_j + d_p \gamma_{j+1}$	$w_d = f \gamma$
$\Phi_p = g \gamma_j + h \gamma_{j+1}$	$\Phi_d = q \gamma$

Here only the terms a_p, b_p, c_p, d_p need coordinate transformations since other coefficients are already given in inertial coordinates.

$$\begin{bmatrix} a \\ b \\ c \\ d \end{bmatrix} = \begin{bmatrix} \cos(\zeta) & 0 & \sin(\zeta) & 0 \\ 0 & \cos(\zeta) & 0 & \sin(\zeta) \\ -\sin(\zeta) & 0 & \cos(\zeta) & 0 \\ 0 & -\sin(\zeta) & 0 & \cos(\zeta) \end{bmatrix} \begin{bmatrix} a_p \\ b_p \\ c_p \\ d_p \end{bmatrix} \quad (3.10)$$

As defined in sudden acceleration approach, normal component of the velocity at the surface is zero and this is expressed as;

$$(\nabla\Phi + v) \cdot n = 0 \quad (3.11)$$

If we insert the kinematic velocity defined as $v = -[V_0 + v_{rel} + \Omega \times r]$ to the Equation 3.11;

$$(\nabla\Phi - \mathbf{V}_a - \boldsymbol{\Omega} \times \mathbf{r}) \cdot \mathbf{n} = 0 \quad (3.12)$$

This equation is solved for any mid panel - collocation points on the wing surface. Any point on the wing surface has velocity components (X-Z) with respect to inertial frame. The X-Z components of surface normal vector is expressed as n_x and n_z .

If p time interval is passed, for n collocation points on the wing, the velocity equation becomes;

$$\sum_{j=1}^n [(a_j \gamma_j + b_j \gamma_{j+1}) n_x + (c_j \gamma_j + d_j \gamma_{j+1}) n_z] + \sum_{l=1}^p [e_l \gamma_l n_x + f_l \gamma_l n_z] - (U + \dot{\theta} r_z) n_x - (W - \dot{\theta} r_x) n_z = 0 \quad (3.13)$$

For all the vortex panels (n), there are 2 unknowns which are endpoints vortex values. Therefore, for each collocation points there are n equations but $2n+1$ unknowns. Due to continuity of the bound vortex distribution, the circulation at the end connection points of the sequential vortices must have the same values. This reduces the unknown number to $n+2$. Since Kelvin condition provides 1 more equation the equation number increases to $n+1$. However, $n+2$ unknowns need $n+2$ equations to solve; therefore 1 more equation is needed. Kutta condition provides this final equation and makes the system solvable.

These two conditions are given in detail in Sections 3.3.2 and 3.3.3.

3.3.2 Kelvin Condition

According to conservation of wake the circulation encircling the wing does not change. Therefore, the bound circulation is equal to the sum of the circulation due wake vortices.

Therefore for p time period total circulation is;

$$\Gamma_p = (\oint \gamma(s) ds)_p + \sum_{l=1}^{p-1} \gamma_l + \gamma_p \quad (3.14)$$

$$\Gamma_p - \Gamma_{p-1} = 0 \quad (3.15)$$

$$(\oint \gamma(s) ds)_p - (\oint \gamma(s) ds)_{p-1} + \gamma_p = 0 \quad (3.16)$$

The bound circulation is composed of linearly increasing vortex panels;

$$\left(\sum_{j=1}^{n+1} \gamma_j\right)_p - \left(\sum_{j=1}^{n+1} \gamma_j\right)_{p-1} + \gamma_p = 0 \quad (3.17)$$

3.3.3 Kutta Condition

There is no discontinuity at the top and bottom point of the trailing edge, therefore the circulation value at the trailing edge gets zero value.

$$\gamma_1 + \gamma_{n+1} = 0 \quad (3.18)$$

Equations 3.13, 3.17 and 3.18 are used to obtain coefficient matrices to have system of equations in the form $AX=B$. A matrix has $(n+2) \times (n+2)$ dimension and composed of the coefficients of γ and γ_p , X matrix includes the unknown terms and its dimension is $(n+2) \times 1$ and matrix B includes all known terms of kinematic and geometric definitions and its dimension is $(n+2) \times 1$ too.

Using this panel algorithm, a model is developed in MATLAB Simulink Base, and wake velocity and velocity potential are calculated at each collocation points.

3.3.4 Unsteady Bernoulli Equation

After finding velocity of the wake, the pressure is calculated using Bernoulli Equation with additional time dependency term. As Katz & Plotkin [24] derives, all formulas are transformed into body fixed coordinate system.

$$\frac{P_\infty - P}{\rho} = \frac{1}{2} \left[\left(\frac{\partial \phi}{\partial x} \right)^2 + \left(\frac{\partial \phi}{\partial z} \right)^2 \right] + \frac{\partial \phi}{\partial t} \quad (3.19)$$

$$\frac{P_\infty - P}{\rho} = \frac{1}{2} \left[\left(\frac{\partial \phi}{\partial x} \right)^2 + \left(\frac{\partial \phi}{\partial z} \right)^2 \right] - (V_a - \Omega \times r_a) \nabla \Phi + \frac{\partial \phi}{\partial t} \quad (3.20)$$

Here the potential term included both panel potential (Φ_p) and discrete potential (Φ_d).

For hovering micro air vehicles the lift force is important to balance the gravity force, and the drag force is important for control maneuvers. In addition to these forces, the moment around $\frac{3}{4}$ chord is calculated by the below integrals.

3.3.5 Unsteady Force Integration

The pressure distribution on the airfoil surface is integrated to obtain lift and drag forces and moment about the quarter chord.

$$F'_x = -\oint P(s) \hat{n} \cdot \hat{i} ds \quad (3.21)$$

$$F'_z = -\oint P(s) \hat{n} \cdot \hat{k} ds \quad (3.22)$$

$$M'_{qc} = -\oint P(s) \vec{r}_{qc} \times \hat{n} ds \quad (3.23)$$

Here \vec{r}_{qc} is the vector drawn from the $\frac{3}{4}$ chord to wing surface.

All these circulation, pressure, forces and moments are updated at the end of each time period and the new wake field is obtained [25].

Since the vortices are free to move in the wake field, their position are also updated by the velocity induced on them. By this way the wake pattern can be obtained too.

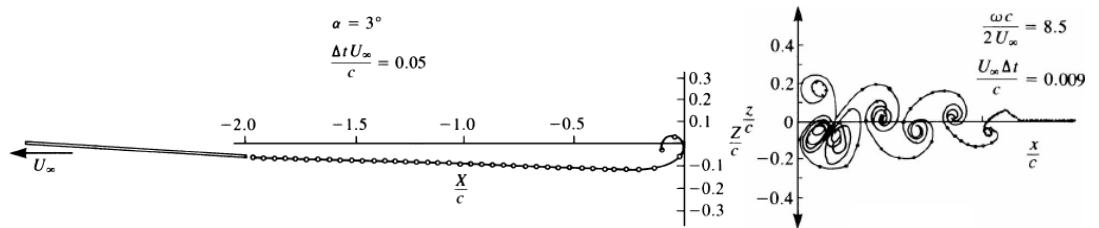


Figure 3.6 Wake patterns for sudden acceleration and flapping cases respectively [24]

After these all procedure, an external integration is needed to obtain total forces and moments on the wing after calculation of section-wise distributions. Simulink for subsystem is used to collect the data array for all forces, and summed after multiplying with unit span length. By this way, the total unsteady forces on the

flapping wing is obtained due to motion kinematics, airfoil geometry, span-wise wing shape, number of collocation points, unit time and number of span-wise sections.

CHAPTER 4

ATTITUDE DYNAMICS OF FLAPPING BODY

To design a flapping mechanism, rigid body dynamics due to wing(s) kinematics must be modeled. First the unsteady aerodynamic forces on the wings are calculated by the various methods found in literature; second effects of these forces at the body center are calculated in three dimensions to analyze body attitude dynamics.

4.1 Rotation Matrices for Left Wing

Time dependent values of yaw, pitch and roll angles (ϕ, θ, ψ) of the flapping wing body are obtained by the moments along rotation axes. To do this, the rotation matrices (R) for both right and left wings are used. For the left wing [42];

$$R_{fL} = \begin{bmatrix} 1 & 0 & 0 \\ 0 & \cos(f_L) & -\sin(f_L) \\ 0 & \sin(f_L) & \cos(f_L) \end{bmatrix} \quad (3.24)$$

$$R_{pL} = \begin{bmatrix} \cos(p_L) & 0 & -\sin(p_L) \\ 0 & 1 & 0 \\ \sin(p_L) & 0 & \cos(p_L) \end{bmatrix} \quad (3.25)$$

$$R_{sL} = \begin{bmatrix} \cos(s_L) & \sin(s_L) & 0 \\ -\sin(s_L) & \cos(s_L) & 0 \\ 0 & 0 & 1 \end{bmatrix} \quad (3.26)$$

$$R_L = R_{pL}R_{fL}R_{sL} \quad (3.27)$$

$R_L =$

$$\begin{bmatrix} \cos(p_L) \cos(s_L) + \sin(p_L) \sin(f_L) \sin(s_L) & \cos(p_L) \sin(s_L) - \sin(p_L) \sin(f_L) \cos(s_L) & -\sin(p_L) \cos(f_L) \\ -\cos(f_L) \sin(s_L) & \cos(f_L) \cos(s_L) & -\sin(f_L) \\ \sin(p_L) \cos(s_L) - \cos(p_L) \sin(f_L) \sin(s_L) & \sin(p_L) \sin(s_L) + \cos(p_L) \sin(f_L) \cos(s_L) & \cos(p_L) \cos(f_L) \end{bmatrix} \quad (3.28)$$

The transpose of Equation 3.28 is;

$$R_L^T = \begin{bmatrix} \cos(p_L) \cos(s_L) + \sin(p_L) \sin(f_L) \sin(s_L) & -\cos(f_L) \sin(s_L) & \sin(p_L) \cos(s_L) - \cos(p_L) \sin(f_L) \sin(s_L) \\ \cos(p_L) \sin(s_L) - \sin(p_L) \sin(f_L) \cos(s_L) & \cos(f_L) \cos(s_L) & \sin(p_L) \sin(s_L) + \cos(p_L) \sin(f_L) \cos(s_L) \\ -\sin(p_L) \cos(f_L) & -\sin(f_L) & \cos(p_L) \cos(f_L) \end{bmatrix} \quad (3.29)$$

Here the terms f, p and s are for flapping, pitching and sweeping motions of the wing respectively. Subscripts; L denotes left wing; R denotes right wing.

The angular velocities for the left wing are [42];

$$\omega = R_L \begin{bmatrix} 0 \\ 0 \\ \dot{s}_L \end{bmatrix} + R_{pL} R_{fL} \begin{bmatrix} \dot{f}_L \\ 0 \\ 0 \end{bmatrix} + R_{pL} \begin{bmatrix} 0 \\ \dot{p}_L \\ 0 \end{bmatrix} \quad (3.30)$$

$$\omega = \begin{bmatrix} p_{Left} \\ q_{Left} \\ r_{Left} \end{bmatrix} = \begin{bmatrix} -\cos(p_L) \dot{f}_L - (\sin(p_L) \cos(f_L)) \dot{s}_L \\ \dot{p}_L - \sin(f_L) \dot{s}_L \\ -\sin(p_L) \dot{f}_L + (\cos(p_L) \cos(f_L)) \dot{s}_L \end{bmatrix} \quad (3.31)$$

4.2 Rotation Matrices for Right Wing

For the right wing the rotation matrices are [42];

$$R_{fR} = \begin{bmatrix} 1 & 0 & 0 \\ 0 & \cos(f_R) & \sin(f_R) \\ 0 & -\sin(f_R) & \cos(f_R) \end{bmatrix} \quad (3.32)$$

$$R_{pR} = \begin{bmatrix} \cos(p_R) & 0 & -\sin(p_R) \\ 0 & 1 & 0 \\ \sin(p_R) & 0 & \cos(p_R) \end{bmatrix} \quad (3.33)$$

$$R_{sR} = \begin{bmatrix} \cos(s_R) & -\sin(s_R) & 0 \\ \sin(s_R) & \cos(s_R) & 0 \\ 0 & 0 & 1 \end{bmatrix} \quad (3.34)$$

$$R_R = R_{pR} R_{fR} R_{sR} \quad (3.35)$$

$$R_R = \begin{bmatrix} \cos(p_R) \cos(s_R) + \sin(p_R) \sin(f_R) \sin(s_R) & -\cos(p_R) \sin(s_R) + \sin(p_R) \sin(f_R) \cos(s_R) & -\sin(p_R) \cos(f_R) \\ \cos(f_R) \sin(s_R) & \cos(f_R) \cos(s_R) & \sin(f_R) \\ \sin(p_R) \cos(s_R) - \cos(p_R) \sin(f_R) \sin(s_R) & -\sin(p_R) \sin(s_R) - \cos(p_R) \sin(f_R) \cos(s_R) & \cos(p_R) \cos(f_R) \end{bmatrix} \quad (3.36)$$

The transpose of Equation 3.36 is;

$$R_R^T = \begin{bmatrix} \cos(p_R) \cos(s_R) + \sin(p_R) \sin(f_R) \sin(s_R) & \cos(f_R) \sin(s_R) & \sin(p_R) \cos(s_R) - \cos(p_R) \sin(f_R) \sin(s_R) \\ -\cos(p_R) \sin(s_R) + \sin(p_R) \sin(f_R) \cos(s_R) & \cos(f_R) \cos(s_R) & -\sin(p_R) \sin(s_R) - \cos(p_R) \sin(f_R) \cos(s_R) \\ -\sin(p_R) \cos(f_R) & \sin(f_R) & \cos(p_R) \cos(f_R) \end{bmatrix} \quad (3.37)$$

Here the transformation matrices R_L^T and R_R^T are used to translate the forces and moments of the left and right wings calculated due to kinematic and geometric inputs. By this way, the difference in the Euler angles and angular accelerations are found and will be used for stabilization analysis and change in frequency of the motion of any wing is found which is needed for stabilization analysis.

CHAPTER 5

SIMULINK MODEL

5.1 Wing Aerodynamics Module of Present Simulink Model

In the first part of present Simulink model (Flapsim), the unsteady aerodynamic forces on the wing is calculated. Initial step of the Simulink model was writing a script for initial calculations due to geometry of the airfoil. MATLAB Simulink provides opportunity to define callbacks. By this way, the model runs the script once at the beginning of the simulation. In this init function the airfoil coordinates are used to calculate initial positions of collocation points in X and Z directions, trailing edge and quarter chord locations, panel lengths, panel angles, panel normal vectors and influence coefficients. Also the upstream conditions are included in this script.

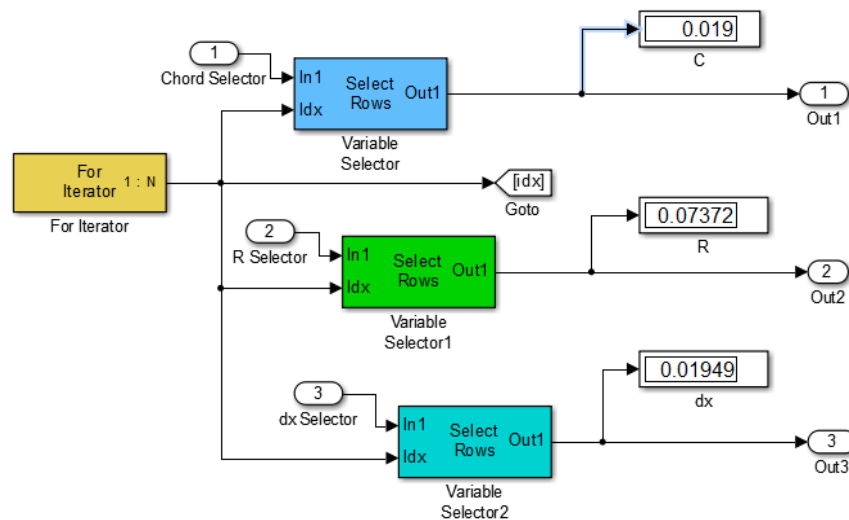


Figure 5.1 For Iterator Subsystem to select parameters for current station

Then the simulation model is placed in for iterator Subsystem shown in Figure 5.1., whose inputs are defined also in an init function as a vector and its dimension

depends on how many sections will be used. These vectors are station-wise chord lengths, radius from the rotation center, and unit span length. Each element of these vectors are selected one by one in time iteration. For example for $t=0$, the lift values for all stations are obtained and integrated to find the total lift force on the wing. In the For Iterator Subsystem, 3 Variable Selector block are used to select these parameters.

After the init function and the outer For Iterator Subsystem are built; a Time Iterator Subsystem is modelled. The inputs for this Subsystem are defined in init function and selected by for iteration. In configuration parameters tab, the solver is defined as fixed step ode1 (Euler) with step size defined in the init function.

The time dependent velocities are calculated during runtime with a user defined function block. Inputs are basically; time, radial position of station, amplitude and frequency. The output velocity vector includes linear velocities of the airfoil in X and Z directions and rotational velocity along its quarter chord. Since the model is mainly tested for flapping motion, the other velocities are taken as zero; however, the model is capable of translating in X direction and pitching motion.

The next step is to update all time dependent values due to kinematic inputs. The airfoil can be initially positioned due to initial pitch angle, then the locations are updated according to this using another user defined function block. The current panel and collocation points, influence coefficients, new trailing edge and quarter chord locations are calculated.

Another block is used for calculations of circulations, velocity potentials and integrated sectional pressure forces. At each iteration time a new wake is formed at the current trailing edge position. And positions of all wakes are updated during time. By this way, the effect of all wake circulations on the bound circulation of each panel is calculated. Once the bound circulations, wake circulations and influence coefficients are obtained, the velocities in x and z directions, the velocity potentials and time derivative of velocity potentials are found with the effects of both vortex panels and wake vortices. Using unsteady Bernoulli Equation, the pressure values on

each vortex panel are calculated. After that, the panel drag and lift forces and moment about quarter chord are obtained integrating surface pressure.

During this procedure, the size of wake-related vectors is increasing with the step number; therefore, they are defined as persistent variables.

The final block is added for span wise force integration and it is chosen as Interpreted MATLAB Function. The total lift, drag and moment values on the wing are defined as global variables. Due to For iterator Subsystem index and a permanent time count, sectional forces and moment are multiplied with corresponding unit span length of station and summed. By this way, the total forces and moment on the wing due to different airfoil shapes and velocity input functions are found. Figure 5.2 is illustrating the whole procedure for calculation total forces the wing for a station-wise section.

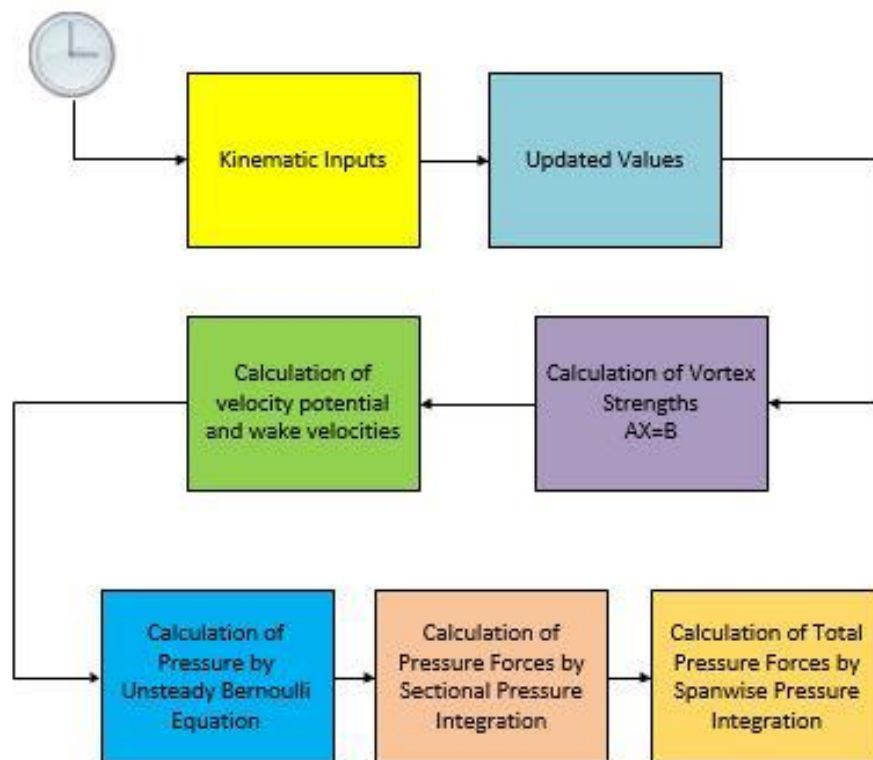


Figure 5.2 Time Iteration Flow-chart for calculation of variables due to wing kinematics and geometry

5.2 Rigid Body Dynamics Module of Present Simulink Model

Second part of the model is to obtain rigid body dynamic forces on the body center of gravity. Transformation matrices are coded in a specific block for both left and right wings. Different input frequencies and amplitudes may be defined for left and right wings; however the aerodynamic part for two different wings has to be separated for this purpose.

After calculating total forces and moments in all directions; MATLAB 6 DOF rigid body dynamics module can be used to obtain angles and angular accelerations of flapping body as shown in Figure 5.3. In this study, the model is developed for future stabilization applications of roll dynamic analysis of double-flapping wing system. Depending on Euler angles, and corresponding angular accelerations, the flapping motion amplitude and frequency can be controlled to stabilize the system.

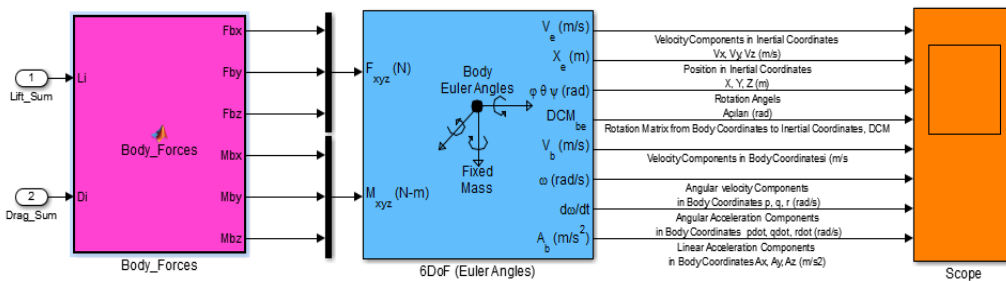


Figure 5.3 Rigid Body Dynamic Analysis due to different Kinematic Inputs on Flapping Wings

CHAPTER 6

DESIGN AND MANUFACTURING OF DYNAMICS TESTING MECHANISM

6.1 Solid Design for Rolling Control Mechanism

For experimental analysis of the roll dynamics of flapping body, a mechanism is designed using CATIA. To do this previously designed four-bar mechanism needed for flapping motion is used; however, this time the weight of the wing mechanisms is more important.

The flapping wing mechanisms are decided to attach from lateral surfaces of their supporting parts to bring the center of mass of the total moving body to rotation center. Also the height of the part under the bearing is increased to prevent flapping mechanisms to touch the ground.

Two symmetric flapping wing mechanisms are balanced around a rotational axis using 2 parallel plexiglass parts with free rotating bearings. The roll moment around this bearing is planned to be analyzed due to difference in frequencies and amplitudes of the motions of the wings.

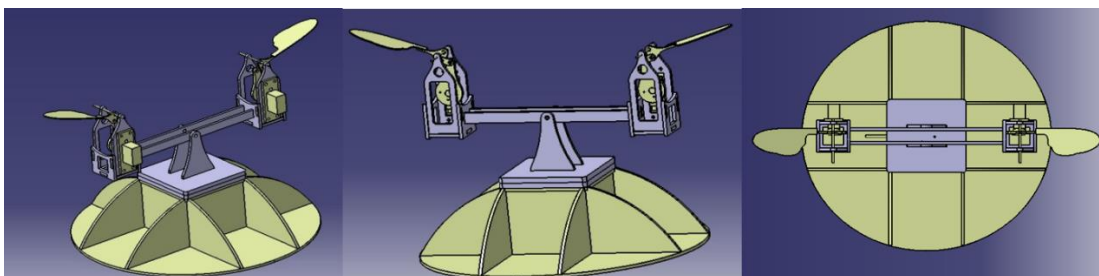


Figure 6.1 Design for roll dynamics including two symmetrical flapping mechanisms

In Figure 6.1 the final design for test mechanism for roll control is illustrated from 3-Different perspectives. The parts from supportive base and lateral components are taken out for weight reduction as seen in Figure 6.2.

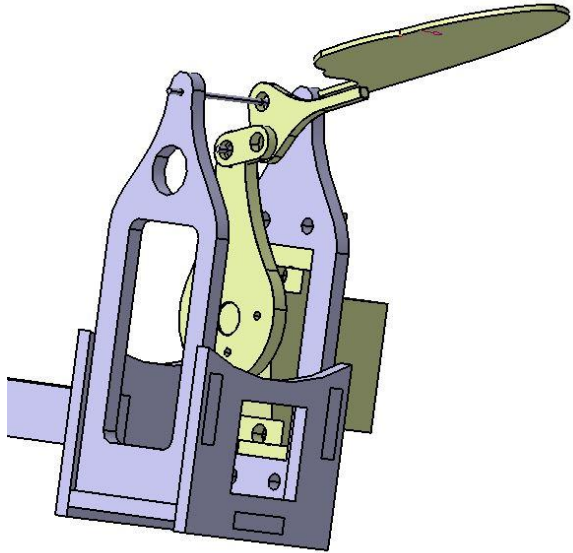


Figure 6.2 Four-bar Mechanism used for Flapping System

The four bar flapping wing mechanism used in this study is inspired and sized due to LIPCA actuated flapping device [29]. In Figure 6.3, the preliminary design with double-wing four bar mechanism with piezo-actuator is shown. However, it is decided to design a seesaw mechanism instead to make the rolling analysis easier.

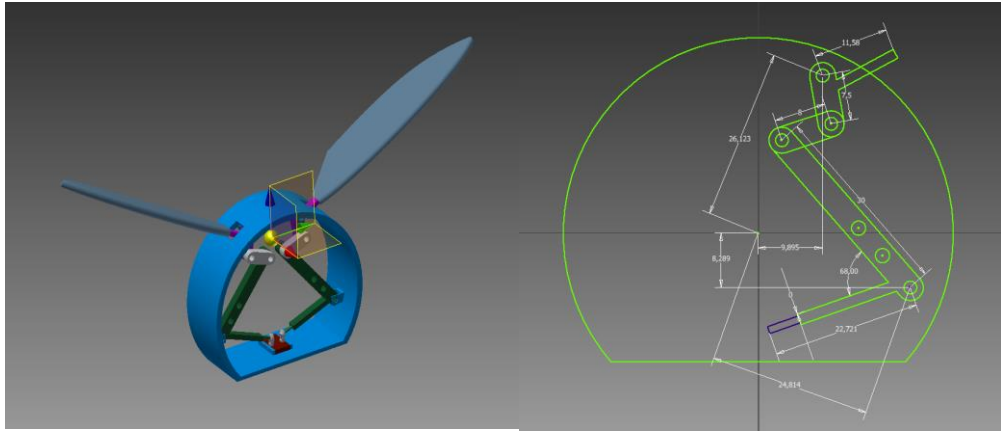


Figure 6.3 Preliminary Design of mechanism and parts of the four bar mechanism

The rolling mechanism consists of two parallel plexi parts as seen in Figure 6.4. A middle steel rod is used with two bearings and two segments to provide rotation and holding respectively.

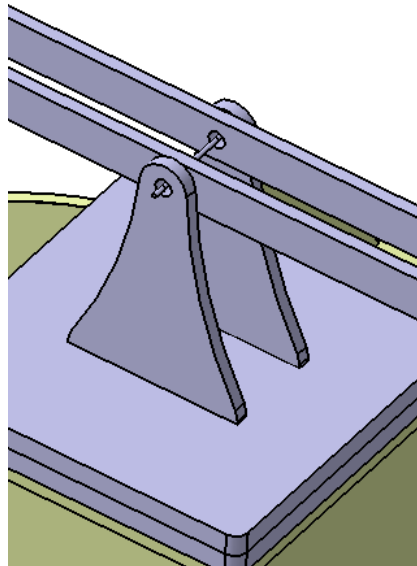


Figure 6.4 Roll Dynamic Testing Mechanism for Two-wing Flapping System

The points on the rods are determined for segments which help the mechanism not slide on the steel rods while flapping motion as seen in Figure 6.5.

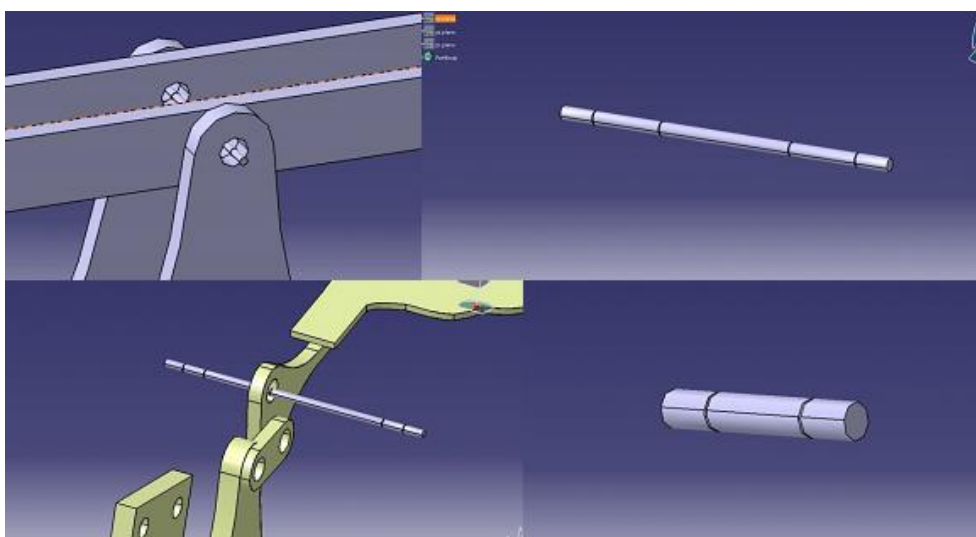


Figure 6.5 Designed Rode Types for Rotational Motion of Mechanisms

6.2 Final Design of Testing Mechanism and Manufacturing Procedure

Spherical Bearing, also known as ‘ball and socket’ joint, is a useful mechanism constraint for analyzing and control in 3 rotational dimensions. Figure 6.6 is illustrating this system and determined to use in double wing flapping mechanism as seen in Figure 6.7 as an assembly for testing roll, pitch and yaw attitude of body due to heaving, sweeping and pitching motion of the wings.

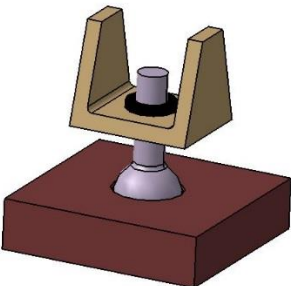


Figure 6.6 Spherical Bearing Assembly

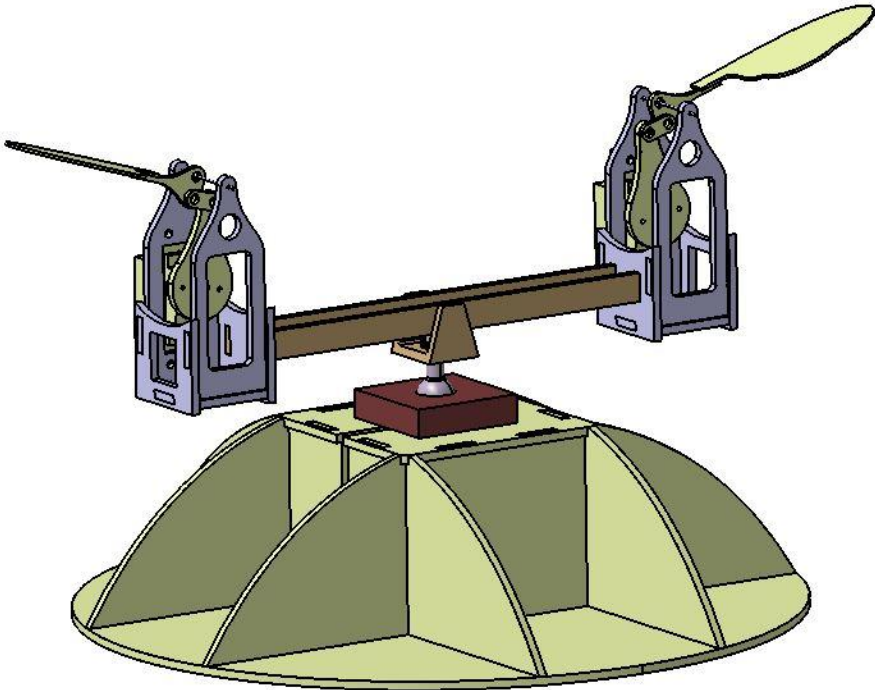


Figure 6.7 Final Mechanism Design for examining body rotations along 3 axes using Spherical Bearing (Ball and Socket)

The example for the design is observed at Atılım University [43] and given in Figure 6.8. However, it is designed for body dynamics attitude of 2 rotors system. Future plan for present work is to test the analytic code for flapping wings with 3 rotational motion control similar for double rotor system with the current design of double flapping wing systems.



Figure 6.8 Example of a Double- Rotor Mechanism for Body Attitude Dynamics [43] After solid modelling of each part of the mechanism, the 2-D face shapes are extracted and cut with the help of laser machine (Ayka Laser Technology) and its software (Phsoft 7.01). First the inner shapes are cut by selecting from the software, then the outer shapes are cut from plexi glass otherwise the part slides while cutting inner holes. The thickness for wings and four bar mechanism (Figure 6.11), supporting parts and rolling mechanism are determined as 1mm, 3mm and 5mm respectively. For each four bar mechanism 5 bearings having 4mm outer 1,5mm inner diameters are used as shown in Figure 6.11.



Figure 6.9 Plexi Parts and Bearings used in 4-bar mechanisms and Plexi Calliphora Wing

In Figure 6.12 the servo attachment is illustrated. The additional plexiglass part is used to screw the servo on the supporting part of flapping mechanism and first part of four bar mechanism for input motion which are shown as 1 and 2 in Figure 6.12.

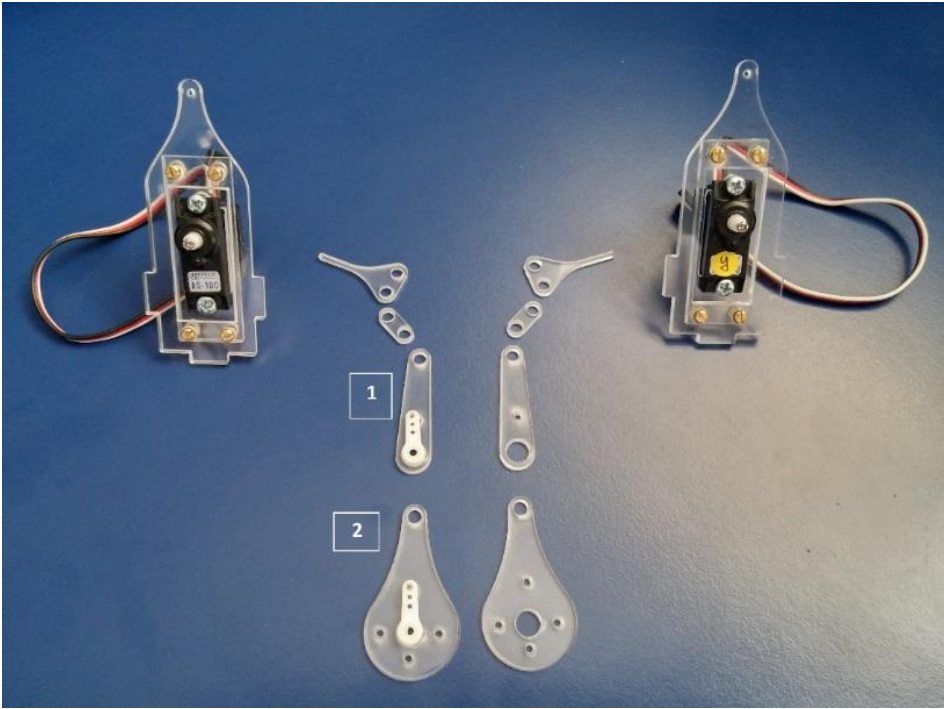


Figure 6.10 Servo attachment and 2-Different 4-bar types

For the rolling mechanism two symmetric seesaw parts (Figure 6.13) are manufactured and stuck from the inner sides of supporting assembly of flapping mechanisms.



Figure 6.11 Parts used in Rolling Mechanism

Preliminary design for IMU attachment is considered as shown in Figure 6.14 which is desired to move with seesaw mechanism to sense the rolling angle and corresponding acceleration.

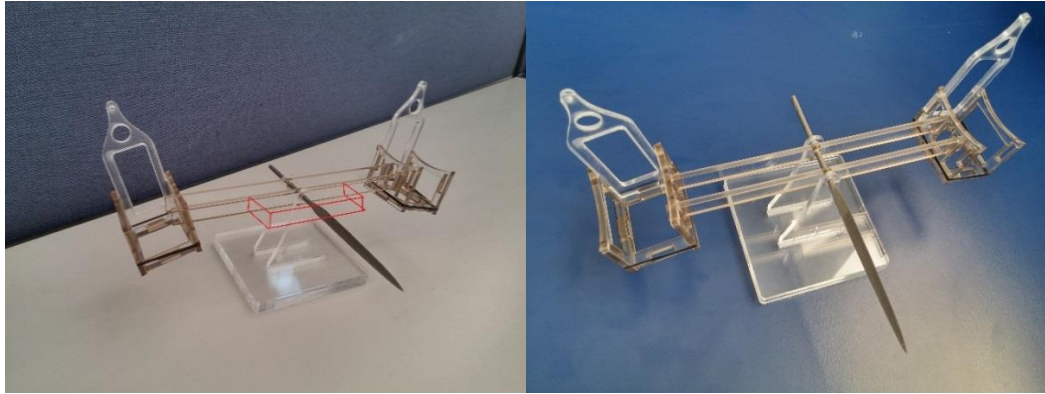


Figure 6.12 IMU attachment design

6.3 Roll Dynamics Control Algorithm

After forces and moments calculated by wing aerodynamics are translated to body roll center, the unstable behavior of the body can be stabilized by a control algorithm by estimating the frequency or amplitude differences required to balance the moments around a rotation axis.

The reference roll angle of the mechanism is known and the time dependent values of the angles and angular accelerations are measured using an IMU including a gyrometer and an accelerometer on it.

The transformation matrices obtained in Chapter 4 are for all 3-D angular motion of the body; however, for the roll analysis, many terms in the matrices are zero.

The average values of calculated or measured aerodynamic forces and moments are widely used for prediction of motion of FMAVs. This serves less complexity in computation for control strategies.

There are many different control algorithms used in previous studies for an implementation mainly based on PI, PD or PID for attitude control, tracking or

regulation. The more robust models depending on aerodynamic interactions use control methodologies like LQR.

PID controller calculates the error between the reference and instant value of the variables and decreases this error value. In the full form of PID; “Proportional” is standing for current error, “Integral” is for the sum of previous errors and “Derivative” is for prediction of future errors. These all three actions are performed to adjust the system attitude.

For LQR controllers, the system dynamics are represented by linear differential equations and a LQ problem is obtained by a quadratic (cost) function. This cost function is obtained by the sum of key measurements of desired values as given in Equation 3.3 where the Q and R are weighting matrices for state and control. The optimal control problem is finding the state input minimizing this performance index or cost function.

In Figure 6.13, the control algorithm planned to be used for rolling attitude testing apparatus is shown. The controller is open-loop which is also known as non-feedback controller since it computes the input of the system but not the direct feedback (output) due to current input state. For the present case, the inputs of the systems can be frequencies and amplitudes of the wings’ flapping motions. Hence, depending on the rolling angle difference from the reference, the change in motion inputs will be modeled.

When left and right wings are flapping with nominal amplitude values (A_{Rn}, A_{Ln}) , the roll moment of the body about rotation axis is found and measuring the current roll velocity of body, we decide change in amplitudes $(\delta A_R, \delta A_L)$ for stabilization with the current algorithm.

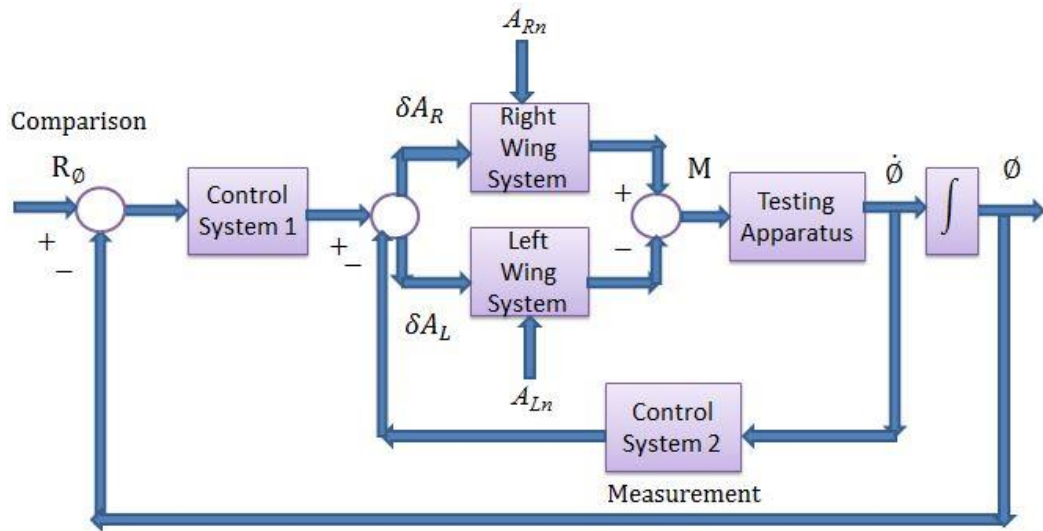


Figure 6.13 Schematic of Attitude Dynamics Control

R_ϕ : Reference Roll Angle for testing apparatus

ϕ : Roll Angle

$\dot{\phi}$: Roll velocity

M :The total roll moment around rotation axis

$\delta A_{R,L}$: Control input (amplitude) for Right and Left Wing Systems

$A_{Rn,Ln}$: Nominal Amplitudes of Right and Left Wing Systems

After modelling and testing rolling attitude with corresponding control algorithm, it is aimed to improve control algorithm for 3 rotational motions (roll, pitch and yaw). Both the Euler angles and angular velocities of the flapping body can be sensed by appropriate electronic device (inertial measurement unit) and the motion can be stabilized by real time control of wings' flapping frequencies and amplitudes.

CHAPTER 7

RESULTS AND DISCUSSION

7.1 Basic Sweeping Model with Sudden Acceleration Algorithm

Before starting to Unsteady Panel code, a simple model for a basic airfoil motion which is “sudden acceleration” is performed, which is mentioned in Section 3.1. The results of this model are illustrated in Figure 7.1 and nearly same as the results given by Katz & Plotkin [24].

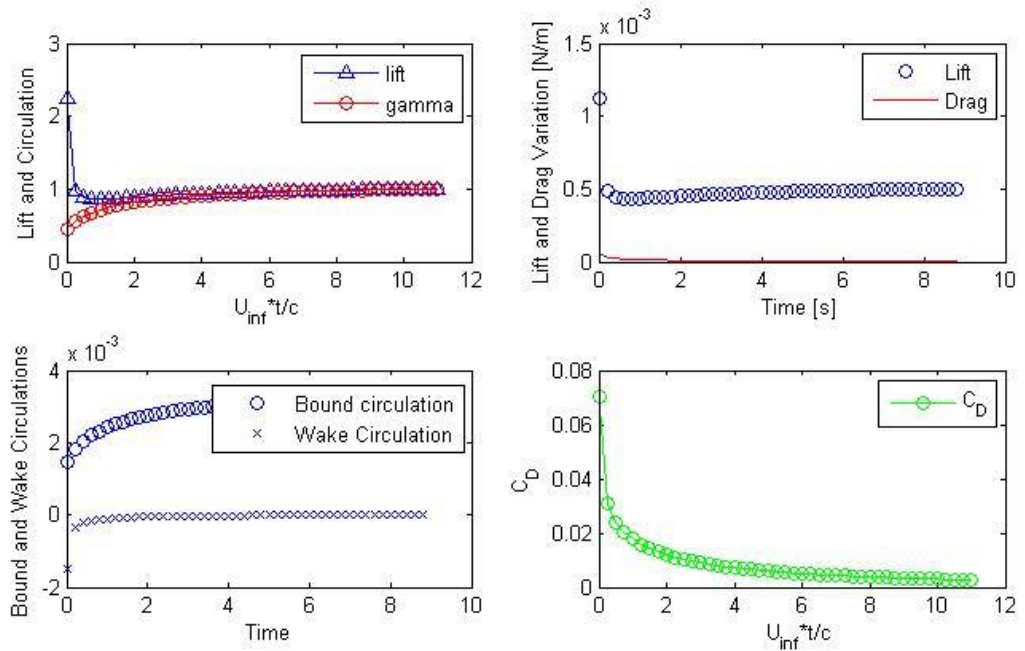


Figure 7.1 Time dependent Circulation and Force Values for Sudden Acceleration of Flat Plate Case ($\alpha = 5^\circ, \Delta t U_\infty / c = 0.25$)

The periodic sweeping case is analyzed by this sudden acceleration algorithm using only 1 collocation point at the quarter chord location. This case is given in detail in Section 3.2.

Defining a “for loop” for span-wise location of the section, the model for periodic sweeping case is developed in a MATLAB script. In Figure 7.2, the result for sweeping motion using sudden acceleration algorithm with single collocation point is shown.

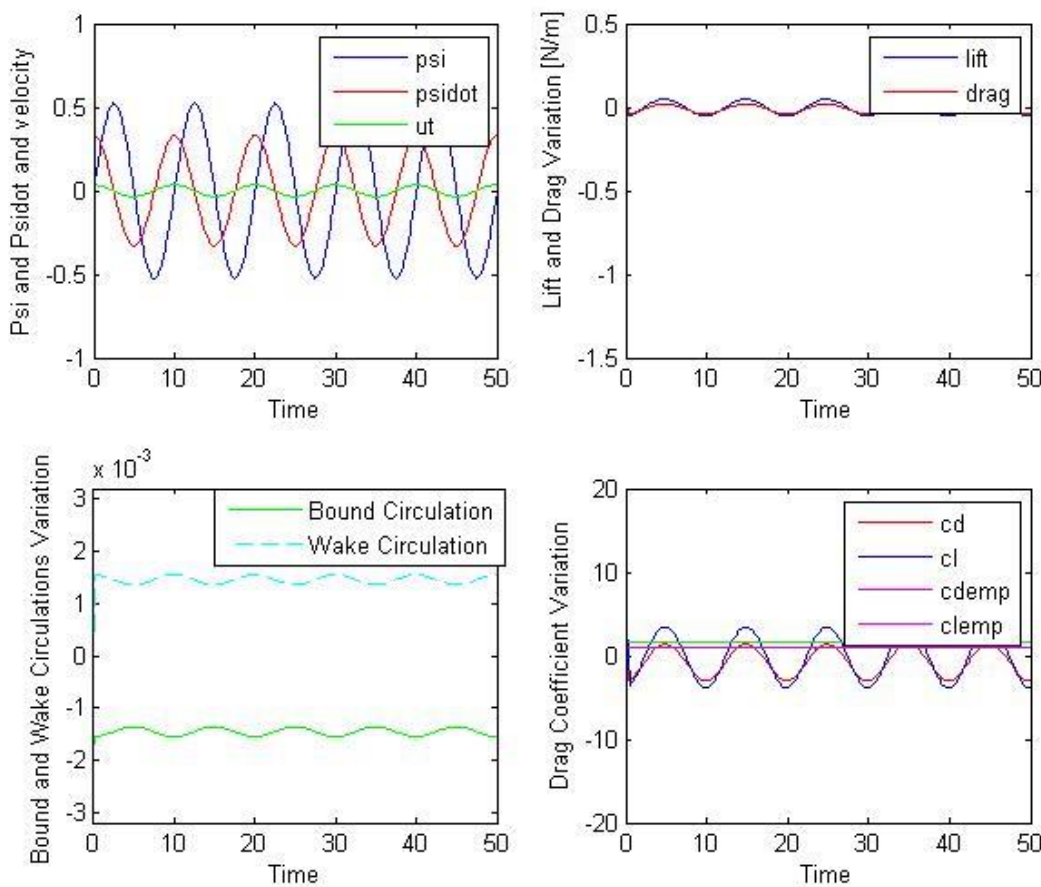


Figure 7.2 Time dependent Circulation and Force Values for Periodic Sweeping of Flat Plate Case ($\alpha = 5^\circ, \Delta t U_\infty / c = 0.25$)

After sectional calculation, in a time loop the forces are integrated and total lift force and span-wise distribution is obtained which are given by Figures 7.3 and 7.4.

Although single collocation point model gives good insight on modelling unsteady aerodynamics and understanding the influence coefficients used in algorithm, it is insufficient for an analysis model. Therefore, multiple collocation points-unsteady panel method is favorable for analyzing different kinematic and geometric inputs.

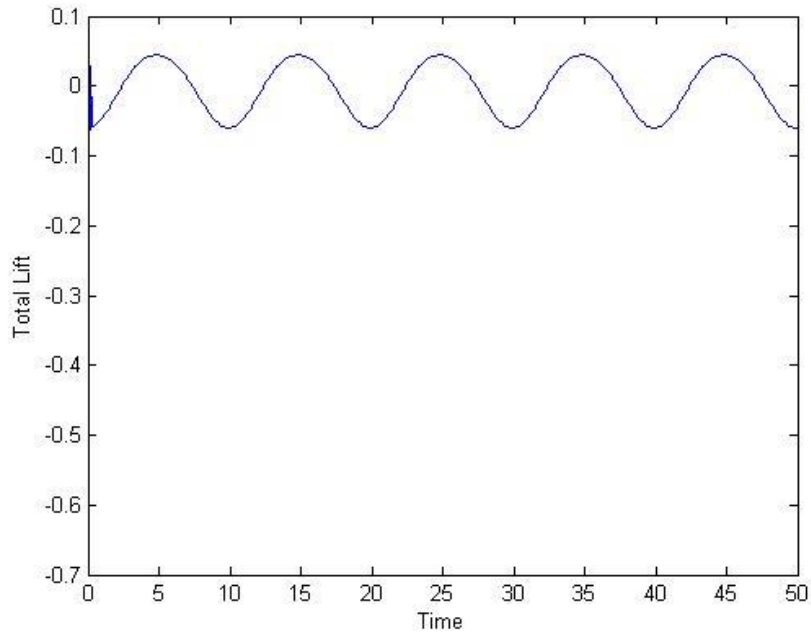


Figure 7.3 Time Dependent Total Lift on the Wing by Periodic Sweeping Motion

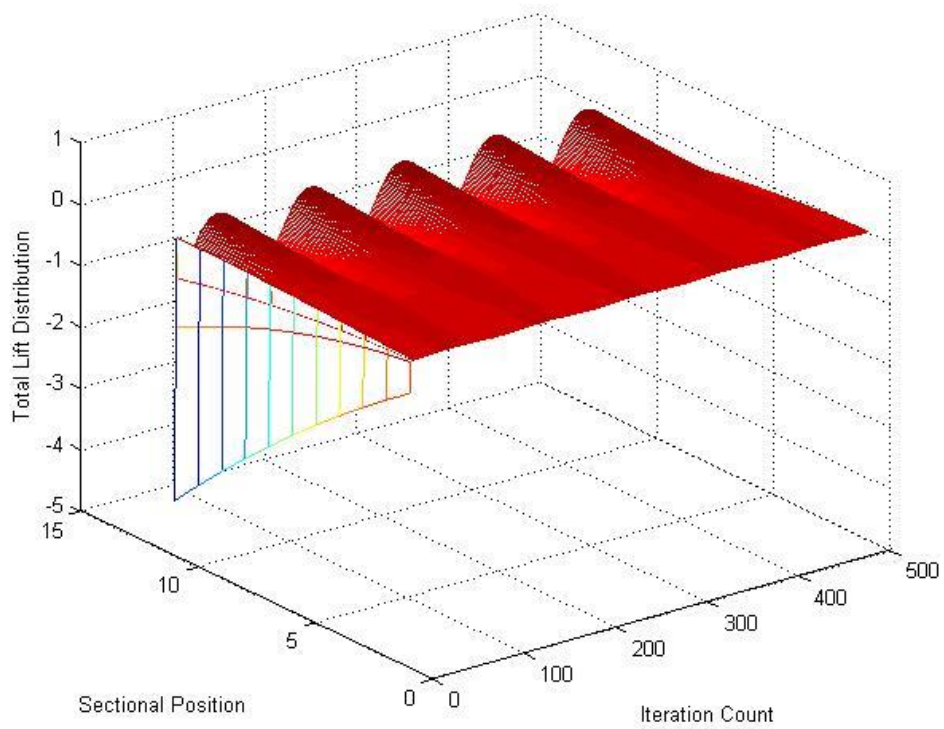


Figure 7.4 Total Span wise Lift Distribution by Periodic Sweeping Motion

7.2 Flat Plate Airfoil Coordinates

Determination of airfoil coordinates for a specific section of a wing is important part of Panel Algorithm. Flat plate section is nothing but a rectangle.

Since the sections of Calliphora have different chord lengths depending on its span-wise shape, the section surface coordinates differ as in Figure 7.5. However, the thickness of the section is same for all stations. This thickness is contributing to the pressure drag since the surface normal vector has chord-wise component at just these edges. The vertical force is similarly affected by upper and lower surfaces of the section.

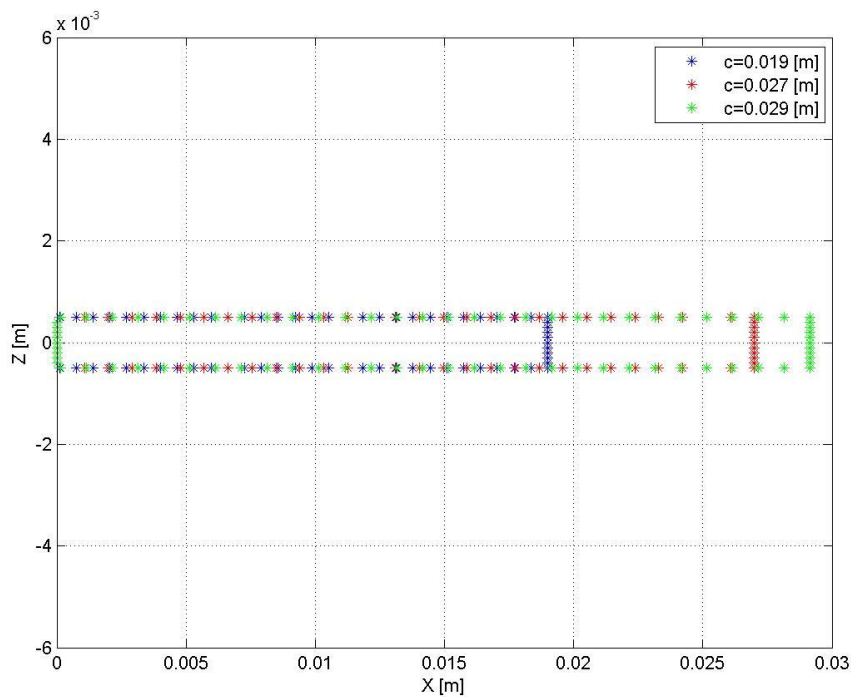


Figure 7.5 Different Sections of Calliphora Wing Shape

It is also important to identify the trailing edge point. For example for the case $c=0.029$ shown in Figure 7.5, the points $(0.029, 0.0005)$, $(0.029, 0)$ and $(0.029, -0.0005)$ are all examined as trailing edge point. In the panel algorithm it is the point that the wake is formed for the corresponding instant time. The results with selection of trailing edge point as $(0.029, 0.0005)$ and $(0.029, -0.0005)$ are favorable due to CFD results; however, selecting the point $(0.029, 0)$ resulted in diverged solution,

since it is not a sharp edge to satisfy the Kutta Condition. Also the trailing edge part can be re-shaped with a triangle ending to have sharp edge for better analysis with Panel algorithm.

Results are obtained for both Calliphora and Flat wings for a specific flapping motion defined as a sine function with two different amplitudes and frequencies. Then, the velocities are found as its first derivation as below.

$$X=A*\sin(\omega t) \quad (7.1)$$

$$V= R*A\omega*\cos(\omega t) \text{ for angular flapping motion} \quad (7.2)$$

$$V= A\omega*\cos(\omega t) \text{ for linear flapping motion} \quad (7.3)$$

The results of present analytic model are compared with results obtained from ANSYS. ANSYS uses CFD Solver which uses a numerical method solving Navier-Stokes Equations. In other words, it applies conservation of mass, momentum and energy equations. Due to complexity of the solution and large meshing numbers, it is computationally expensive. However, it is widely applicable and reliable tool.

The flapping motion is defined by user-defined function (UDF) using dynamic mesh option in CFD by the C code. The 3-D double precision pressure-based solver is used with Least Squares Cell Based method for computing gradient and standard pressure interpolation. Due to grid refinement, the 2 million mesh data set is chosen for comparison [41].

Since ANSYS uses laminar viscous flow, not only pressure forces but also contribution of viscous forces are included. As stated by Prosser [25] the viscous forces mainly act as drag in horizontal direction. Therefore the drag force is affected much more than lift in current comparison cases.

7.3 Results for Heaving Calliphora Wing

The model parameters for Calliphora wing both defined in present Simulink model and UDF functions of Fluent Analysis by Şenol [41], which the results are compared, are shown in Table 7-1.

Table 7-1 Calliphora Wing Parameters

Span	b= 0.05847 [m]
Surface Area	A=1.3752*10 ⁻³ [m ²]
Max Velocity	V=1.35 [m/s]
Density	ρ =1.225 [kg/m ³]

The lift coefficient is defined as;

$$C_L = \frac{L}{\frac{1}{2}\rho V^2 A} \quad (7.4)$$

The denominator of the Equation 7.4 is found as; 1.5351* 10⁻³N for Calliphora Wing Model. Therefore all force results found in Simulink model is divided by this value and multiplied with the trigonometric expression according to Figure 3.3 to compare with the results of aerodynamic force coefficients obtained by CFD.

To calculate the total forces, the wing is divided into 3, 5 and 11 subsections and aerodynamic forces are integrated using these stations for both Calliphora and Flat Plate Wings.

7.3.1 Comparison of Force Coefficients from CFD and Simulink Model due to Heaving Frequency

For two flapping cases (A=41.52°, f=11.2 Hz and A=85.90°, f=5.85 Hz) shown by Figure 7.6 and 7.7, the specific period data for pressure distribution are aimed to compare with CFD results. For the first case 10th period and for the second case 4th period are decided to use since CFD results are affected by impulsive start in earlier periods.

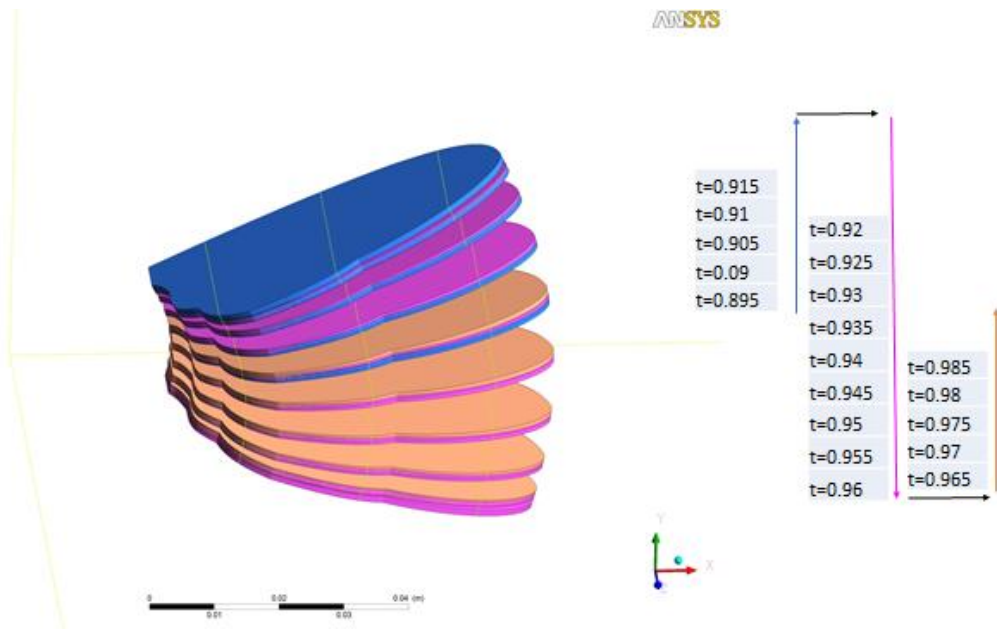


Figure 7.6 Sectional Polylines defined in CFD for pressure distribution of First Case (10th period of the motion with $A=41.52^\circ$, $f=11.2\text{Hz}$) (blue: 1st half upstroke; magenta: downstroke; orange: 2nd half upstroke)

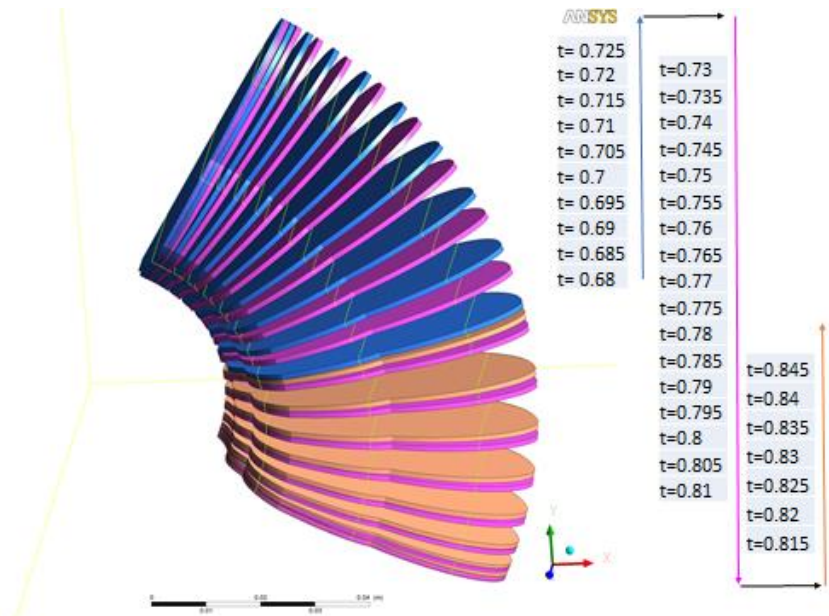


Figure 7.7 Sectional Polylines defined in CFD for pressure distribution of Second Case (4th period of the motion with $A=85.90^\circ$, $f=5.85\text{Hz}$) (blue: 1st half upstroke; magenta: downstroke; orange: 2nd half upstroke)

Figure 7.6 and 7.7 illustrates two flapping cases with the Calliphora wing. First, the linear flapping velocities of the polylines are compared to be same as Simulink model to reduce the error depending on locations. Then the sectional pressure distributions on these polylines are compared with the Simulink model. The time delay between the force results is considered and due to this the pressure distributions on corresponding sections are compared to verify the pressure forces.

Since velocity profiles are different at these sections, the pressure distributions also show alteration.

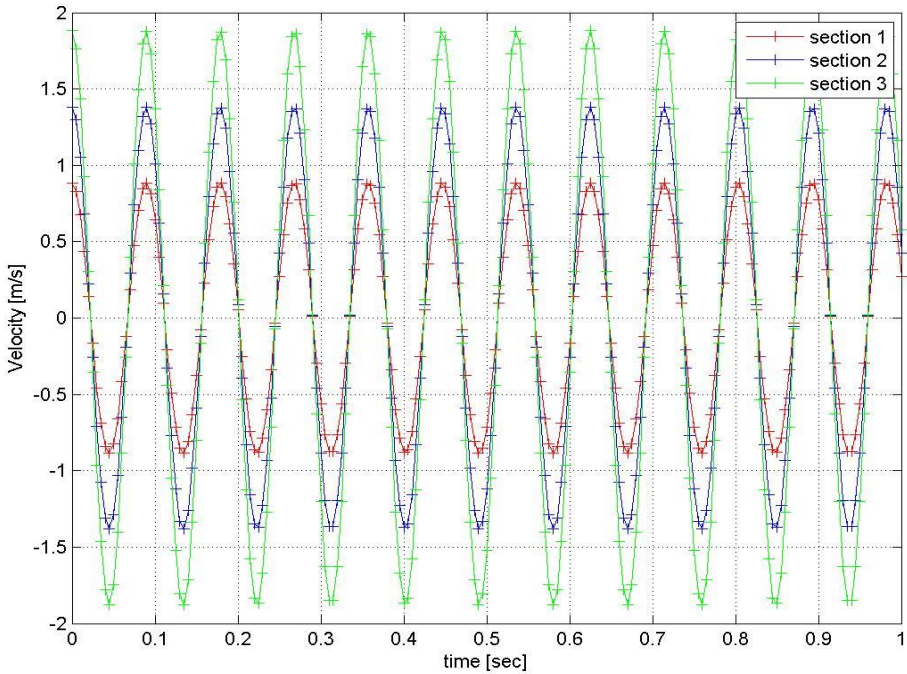


Figure 7.8 Linear Flapping Velocities of Three Different Calliphora Sections (A=41.52° , f=11.2Hz)

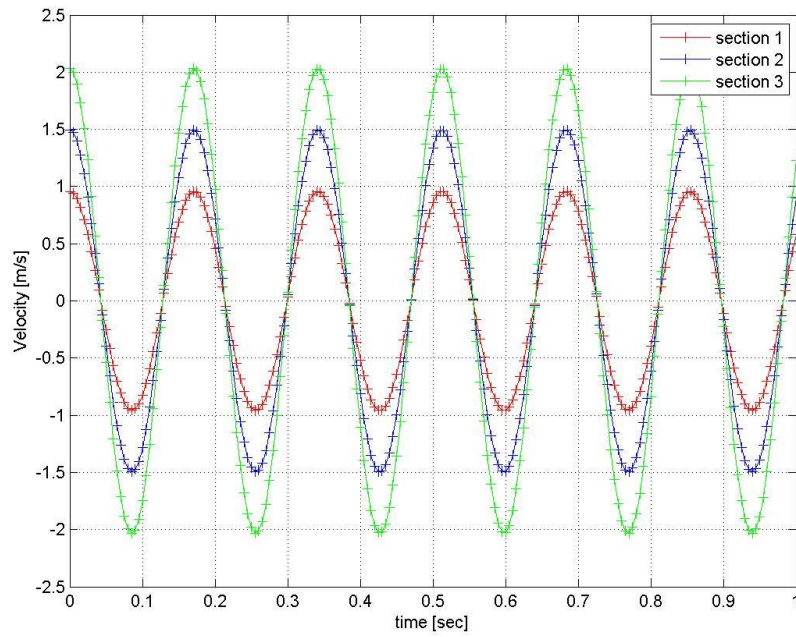


Figure 7.9 Linear Flapping Velocities of Three Different Calliphora Sections
($A=85.90^\circ$, $f=5.85\text{Hz}$)

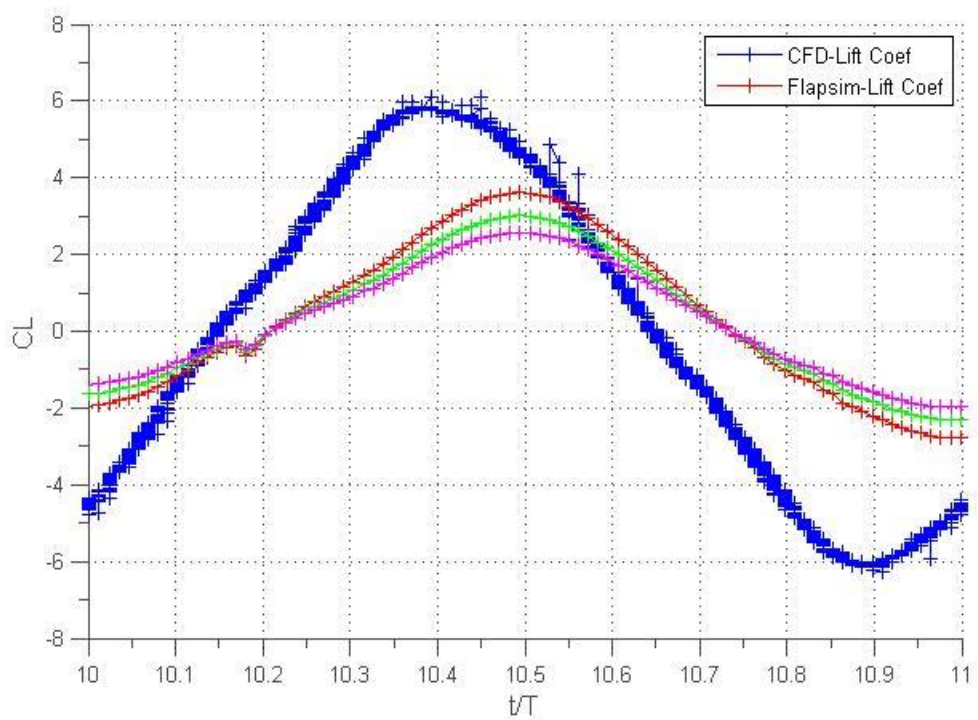


Figure 7.10 Comparison of Lift Coefficient for the First Case 10th period ($A=41.52^\circ$, $f=11.2\text{ Hz}$) in Hover (# of span wise sections: red:11, green:5, magenta:3)

The results for lift coefficients (Figure 7.10, 7.12) are more consistent with the CFD data with a time delay and the difference is more accountable; however, the drag results (Figure 7.11, 7.13) are more complicated to explain. Parasite drag, viscous forces dominating in chord-wise direction and trailing edge re-shape for Kutta Condition in Panel Method are main reasons in difference of drag results. Leading edge vortices are another reason for difference in force results, which will be taken into account as improvement of the model.

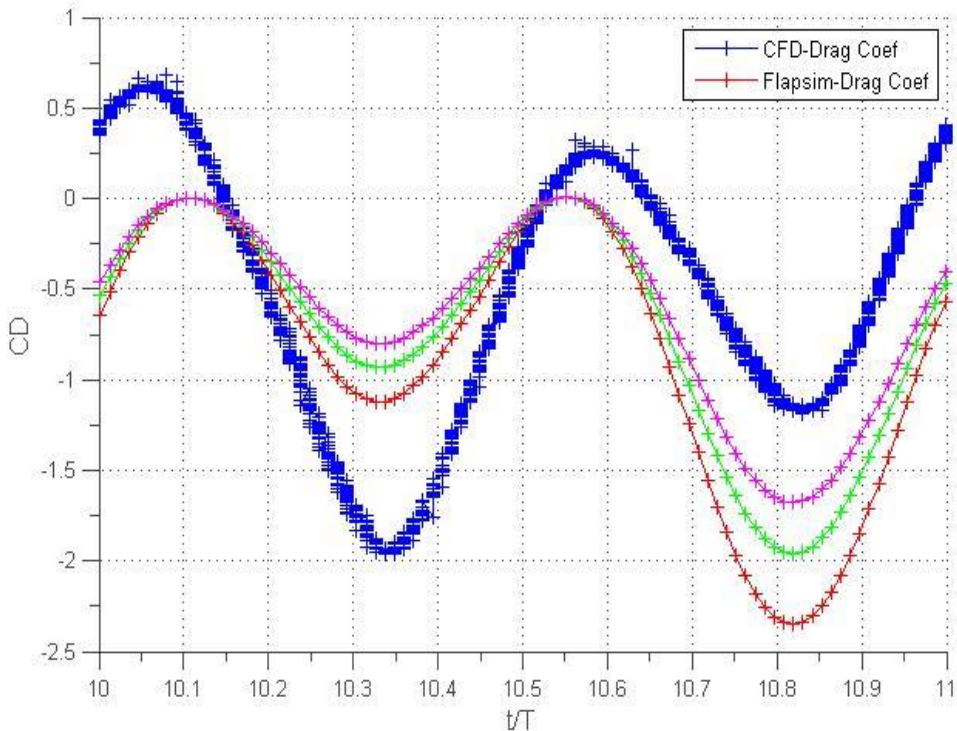


Figure 7.11 Comparison of Drag Coefficient for the First Case 10th period (A=41.52 °, f=11.2 Hz) in Hover (# of span wise sections: red:11, green:5, magenta:3)

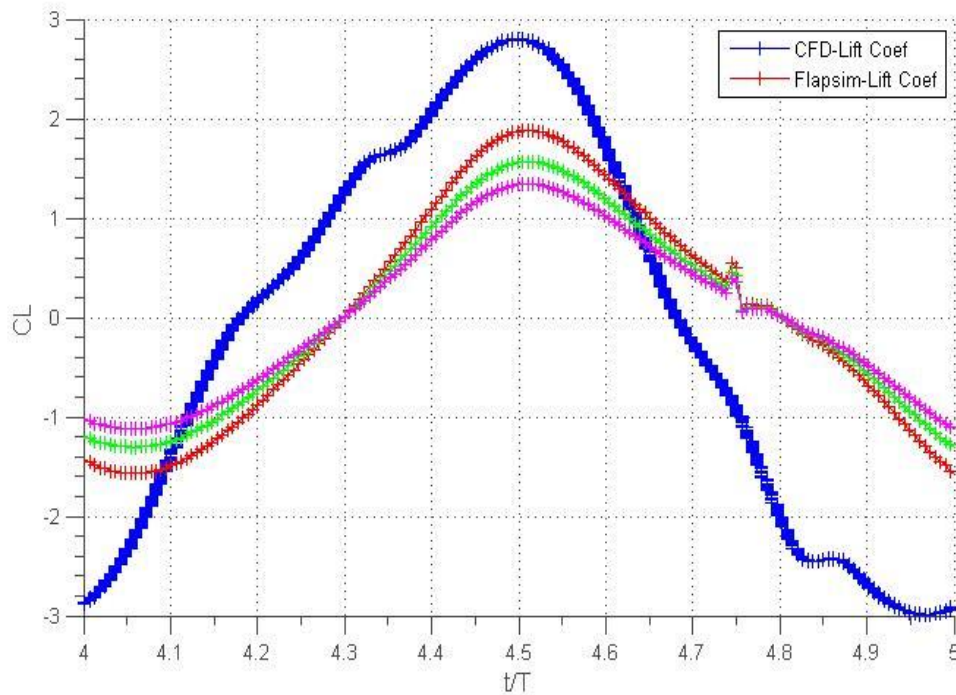


Figure 7.12 Comparison of Lift Coefficient for the Second Case 4th period ($A=85.90^\circ$, $f=5.85\text{Hz}$) in Hover (# of span wise sections: red:11, green:5, magenta:3)

For the first case, maximum value of the lift coefficient from is around 6 and for the second case it is nearly half of the first case. This shows us frequency is more effective on force production than flapping amplitude. Because although the amplitude is double the first case, in second case the reduction of frequency to half caused the force coefficients to reduce by half. Comparing the lift coefficients obtained by Simulink Model (Flapsim), the same reduction is observed; the coefficient is around 4 in first case and 2 for second one with the same time delay.

The lift response is a single peak and drag is smaller two peaks as previously experienced in literature and given by CFD results. However, the amplitudes of two drag peaks are seemed to be interchanged for the first case. The reason is difficult to explain since there are many effects in drag which is not scope of Panel Method Algorithm. For the second case, two drag peaks are seemed to have same amplitudes for both CFD results and Flapsim. Therefore, the first case amplitude differences may be caused by viscous effects.

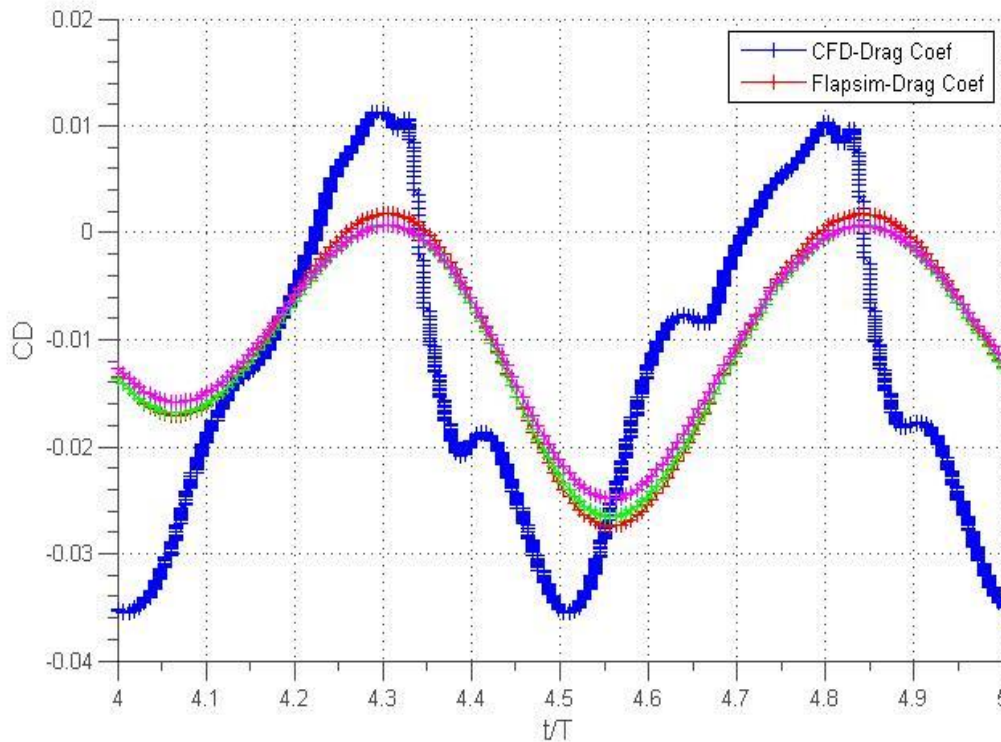


Figure 7.13 Comparison of Drag Coefficient For the Second Case 4th period ($A=85.90^\circ$, $f=5.85\text{Hz}$) in Hover (# of spanwise sections: red:11, green:5, magenta:3)

7.3.2 Comparison of Force Coefficients from CFD and Simulink Model due to Number of Span wise Sections

Since all the span-wise stations have different radial locations, they have different linear flapping velocities. Figures 7.6 and 7.7 are illustrating the section velocities for 3 span-wise stations for two comparison cases. Therefore, the pressure and force distributions on these sections differ. Figures 7.10, 7.11, 7.12 and 7.13 are also included results for different sections of Calliphora Wing which the parameters are given by Tables 7-2, 7-3 and 7-4.

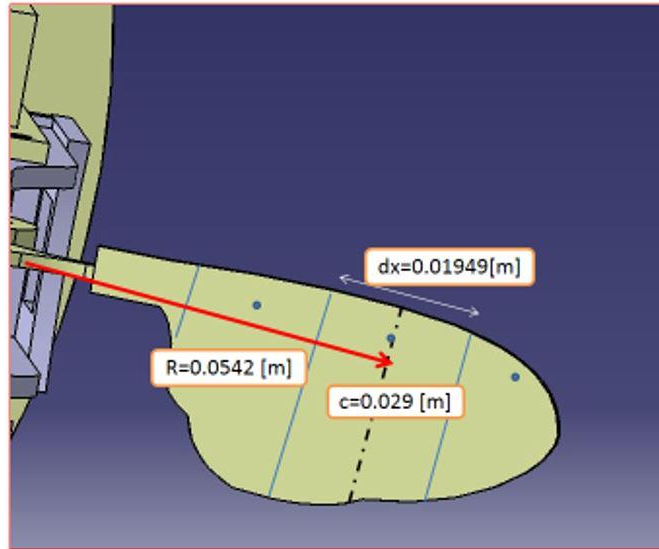


Figure 7.14 Calliphora Wing with 3 Span-wise Sections

Table 7-2 Chord values, Radial Distances and Unit lengths for Calliphora Wing for Case 1

Station #	1	2	3
c	0.03m	0.029m	0.019m
R	0.034m	0.054m	0.074m
dx	0.01949m (0.05847/3)	0.01949m	0.01949m

Table 7-2 gives the properties of 3-Different sections of Calliphora wing. As seen in Figure 7.14 the chord lengths and linear velocities due to radial location differ for each station. The chord length does not have strong effect on the results for calculation using panel method algorithm and even the 3 stations are sufficient to obtain mean chord value. However, each station has different linear velocities for radial flapping case. Due to this, the more the span-wise stations are taken on the wing, the more accurate the results will be. This consideration can be observed on lift graphs however for the drag values this is not much possible since drag forces are affected more strongly by the viscous forces and leading and trailing edge shapes. Also the drag forces include a parasite drag contribution which is not calculated.

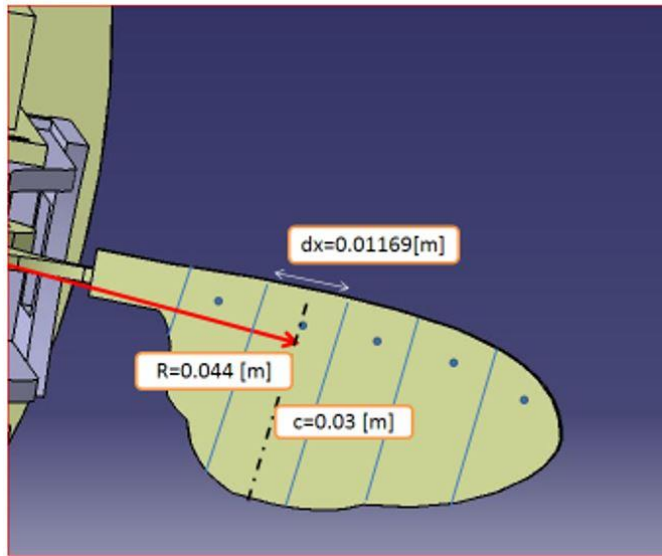


Figure 7.15 Calliphora Wing with 5 Span-wise Sections

Table 7-3 Chord values, Radial Distances and Unit lengths for Calliphora Wing for Case 2

Station #	1	2	3	4	5
c	00.021m	00.03m	0.029m	0.026m	0.016m
R	0.035m	0.044m	0.053m	0.062m	0.074m
dx	0.011694m (0.05847/5)	0.011694m	0.011694m	0.011694m	0.011694m

Table 7-3 gives the properties of 5 different sections of Calliphora wing as shown in Figure 7.15. Similarly, Table 7-4 gives the properties of 11 different sections of as shown in Figure 7.16. Therefore, the linear velocities and radial locations of stations are found due to these numbers of span-wise sections. It is possible to write a function for chord lengths with respect to span-wise location due to span-wise wing shape and determine the unit length between stations as an input variable. However, this study will be a part of real time control algorithm and the execution speed is very important. Therefore, the number of stations sufficient for accurate results has to be found.

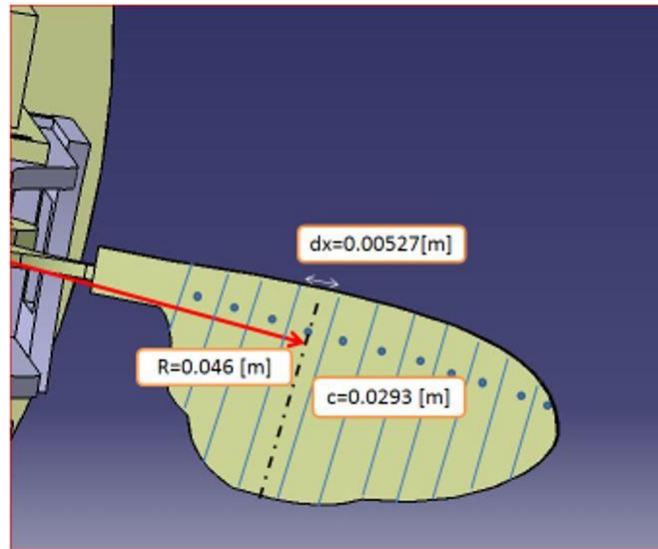


Figure 7.16 Calliphora Wing with 11 Span-wise Sections

Table 7-4 Chord values, Radial Distances and Unit lengths for Calliphora Wing for Case 3

Station #	1	2	3	4	5
c	00.02m	00.029m	0.0293m	0.0293m	0.0295m
R	0.031m	0.036m	0.041m	0.046m	0.051m
dx	0.005272m	0.005272m	0.005272m	0.005272m	0.005272m

6	7	8	9	10	11
0.029m	0.0285m	0.024m	0.022m	0.017m	0.010m
0.056m	0.061m	0.066m	0.071m	0.071m	0.081m
0.005272m	0.005272m	0.005272m	0.005272m	0.005272m	0.00527m

11 stations are determined to be sufficient since the results for lift forces are almost impossible to identify the differences between the results using higher numbers of stations. However, for the drag force results, it is difficult to reach the same conclusion since drag force is affected by many other factors in comparison with CFD results.

7.3.3 Comparison of Force Coefficients from CFD and Simulink Model due to Hover and Forward Flight Cases

The comparison due to Flight Condition (Hover and Forward Flight) with CFD is performed only for the second case. The force coefficients are closer to the CFD data compared to hover cases. Because in hover the leading edge effect cannot be ignored. Since the wing has rectangular sectional profiles, for pure plunge case (hover), the leading edge vortices are formed symmetrically as the trailing edge ones. Therefore, the results for force coefficients are nearly the half of CFD data.

Also for pure hover case trailing edge vortices are not following a path and the collision of fluid particles causes complicated flow pattern. However, in forward flight case, effect of the trailing edge vortices on pressure and force distributions on wing section dominates. Therefore, the results in forward flight case are closer to the data obtained by CFD, but still the viscous and parasite forces are missing.

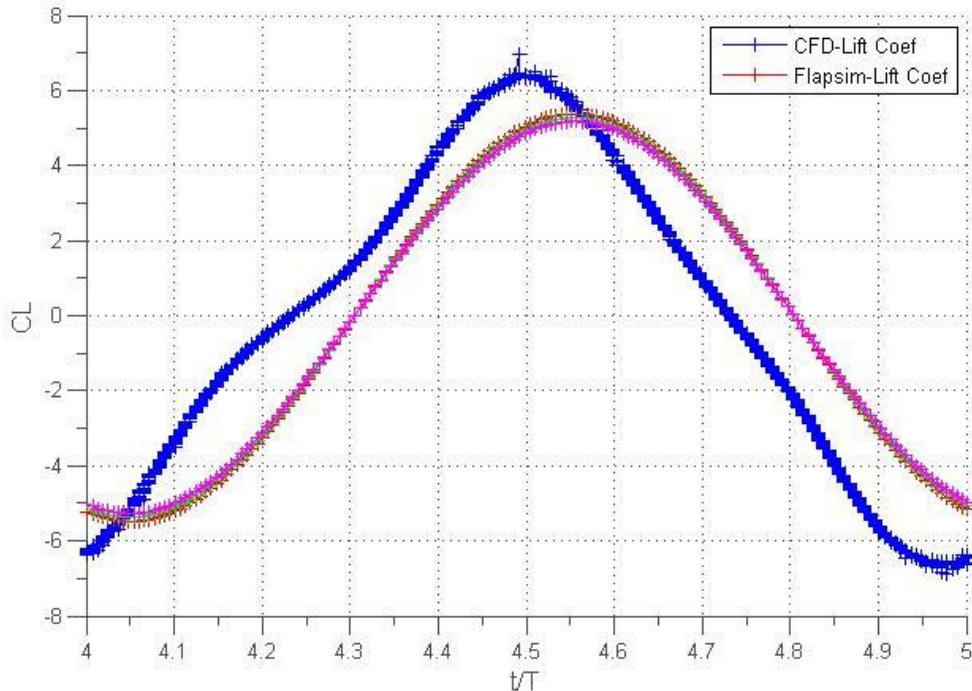


Figure 7.17 Comparison of Lift Coefficient for the Second Case 4th period (A=85.90°, f=5.85Hz) in Forward Flight (U=-3m/s) (# of span wise sections: red:11, green:5, magenta:3)

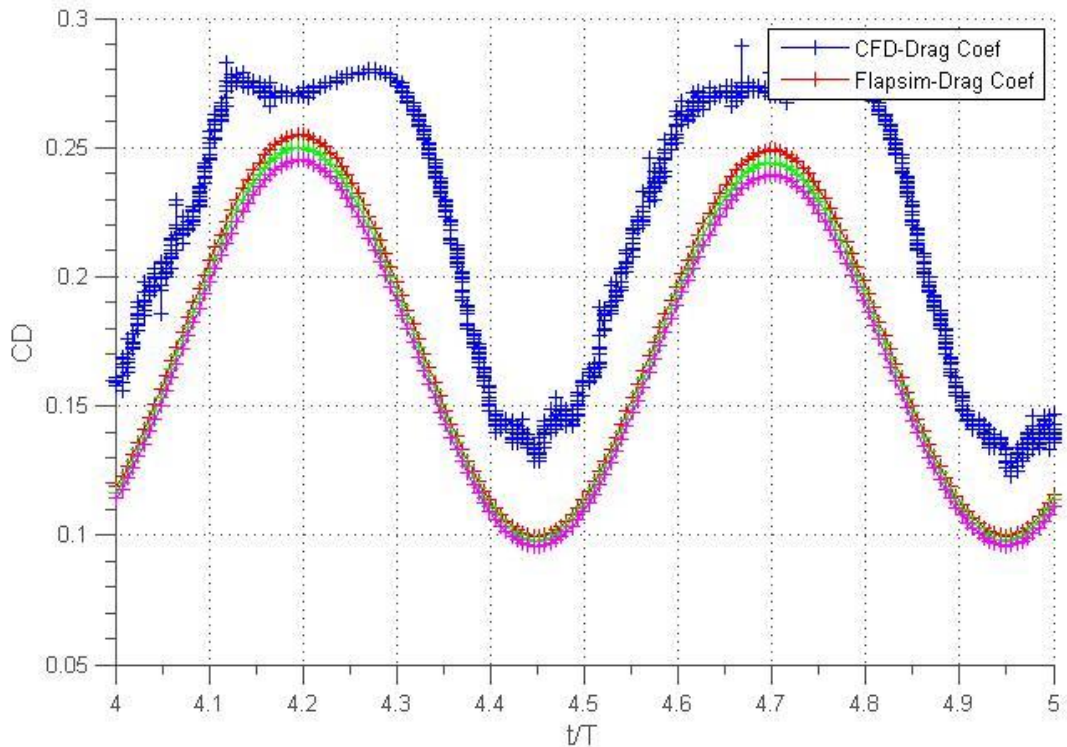


Figure 7.18 Comparison of Drag Coefficient for the Second Case 4th period ($A=85.90^\circ$, $f=5.85\text{Hz}$) in Forward Flight ($U=-3\text{m/s}$) (# of span wise sections: red:11, green:5, magenta:3)

As seen in Figure 7.17 and 7.18 the model is consistent with the CFD results. However, there are many unsteady effects to be considered such as; leading edge vortices, viscous effects, and added mass effects. Nevertheless, the model gives good insight on modelling the aerodynamics compatible with different flight conditions. The other effects can be provided with the tuning parameters for control applications but they are still in the list for future improvements of the present analytic model.

After comparing the results with CFD for the forward velocity -3m/s , the Simulink model is run to obtain a comparison between near hover and forward velocities. Also for these cases, the flow pattern code provided by Prosser [25] is run to observe the trailing edge wake vortices after 1 sec flapping motion.

7.3.3.1 Comparison of 2-D Flow Pattern and Total Force Coefficients for Near Hover Cases of Calliphora for Second Case

Figures 7.19, 7.20, 7.21, 7.22 are illustrating the flow pattern obtained by second flapping case for near hover forward velocity range. Similar code given in appendix by Prosser [25] is used for wake simulation.

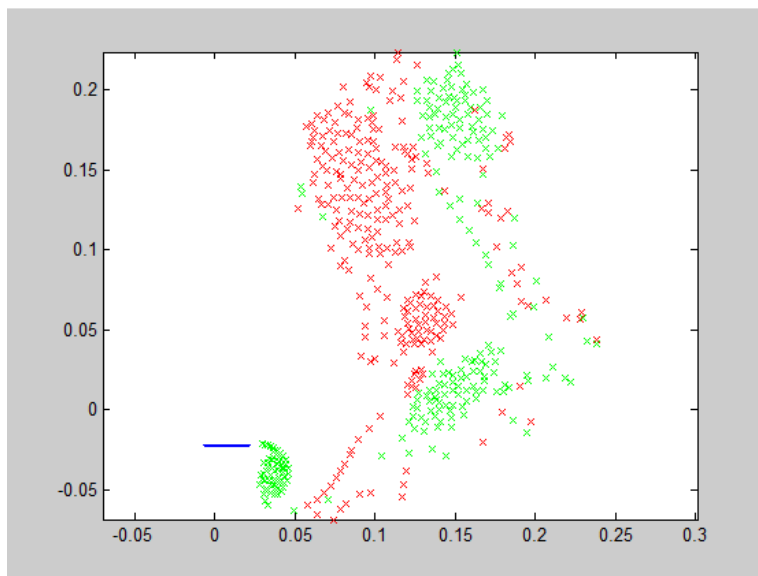


Figure 7.19 Flow Pattern obtained by mid-section (blue line) of Calliphora Wing ($A=85.90^\circ$, $f=5.85\text{Hz}$, $U=0$ [m/s])

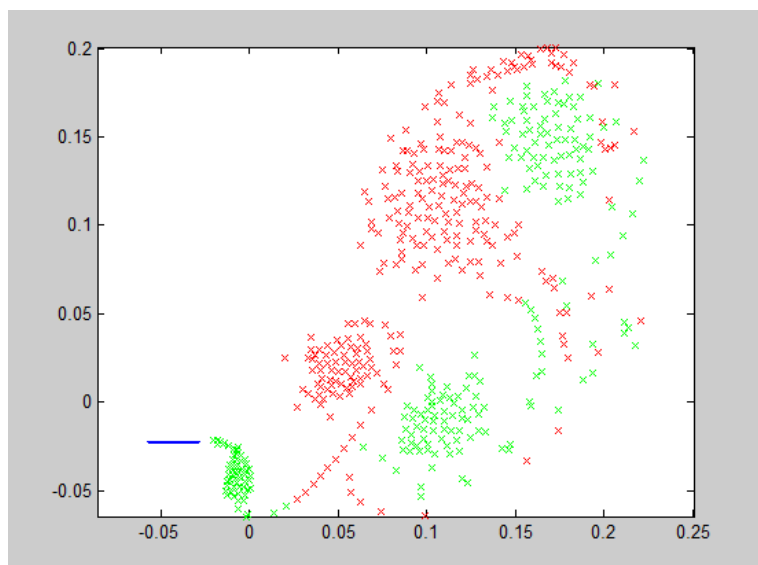


Figure 7.20 Flow Pattern obtained mid-section (blue line) of Calliphora Wing ($A=85.90^\circ$, $f=5.85\text{Hz}$, $U=-0.1$ [m/s])

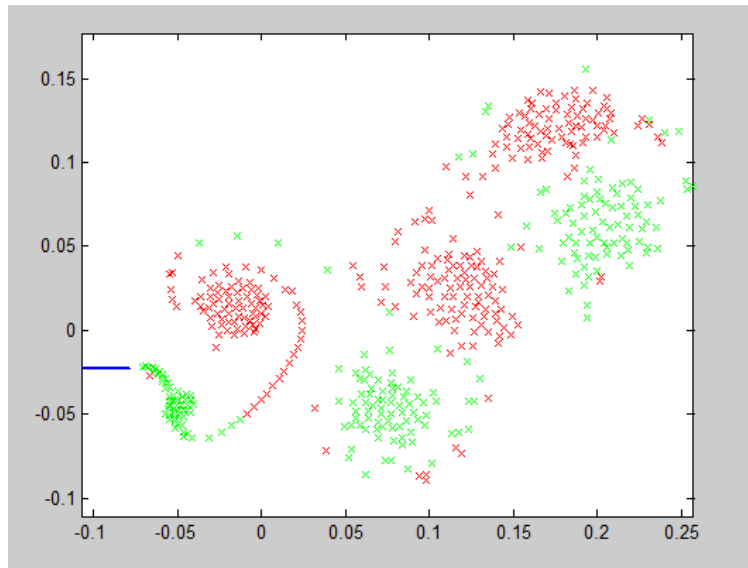


Figure 7.21 Flow Pattern obtained by mid-section (blue line) of Calliphora Wing
($A=85.90^\circ$, $f=5.85\text{Hz}$, $U=-0.2$ [m/s])

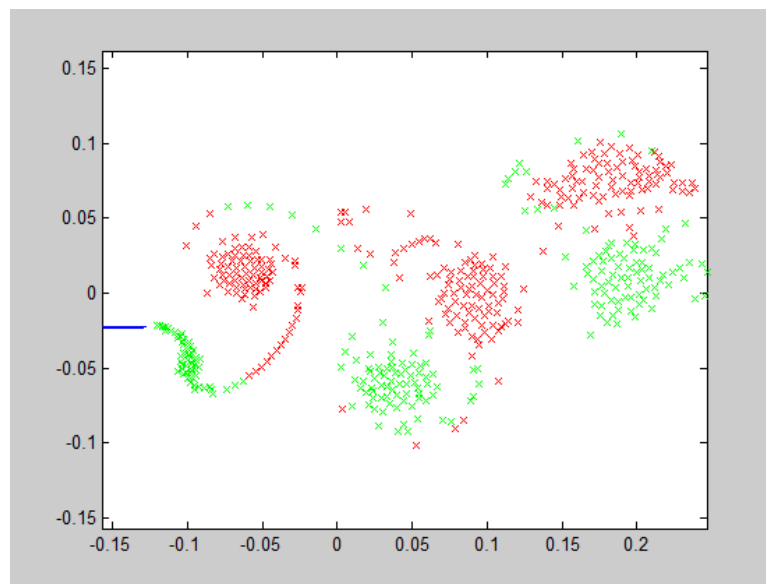


Figure 7.22 Flow Pattern obtained by mid-section (blue line) of Calliphora Wing
($A=85.90^\circ$, $f=5.85\text{Hz}$, $U=-0.3$ [m/s])

Figure 7.23 and 7.24 gives comparison of lift and drag force coefficients obtained due to near-hover forward velocities. Higher velocity results in higher peaks for lift graphs. Also the Figure 7.23 is illustrating the bumpiness at very earlier strokes in lift graph.

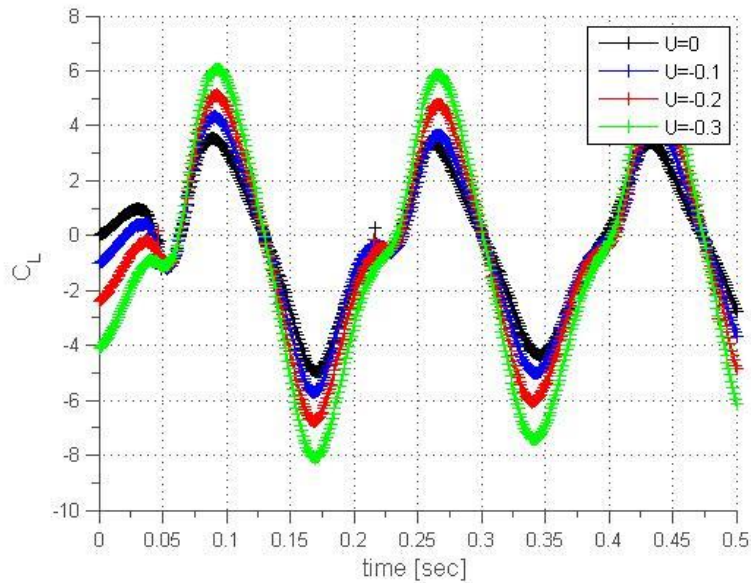


Figure 7.23 Comparison of Total Lift Coefficient on Calliphora having different near hover velocities ($A=85.90^\circ$, $f=5.85\text{Hz}$) ($U=0, -0.1, -0.2, -0.3$ [m/s])

The drag graphs have 2 peaks changing its amplitude periodically and have higher amplitudes for earlier strokes and peaks are getting equal after 4 strokes. The near-hover forward velocity affects the lower drag peaks only.

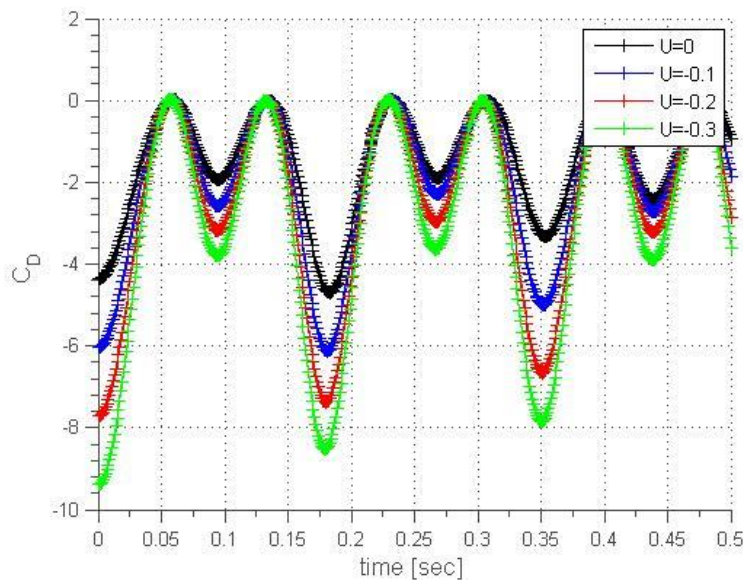


Figure 7.24 Comparison of Total Drag Coefficient on Calliphora having different near hover velocities ($A=85.90^\circ$, $f=5.85\text{Hz}$) ($U=0, -0.1, -0.2, -0.3$ [m/s])

7.3.3.2 Comparison of 2-D Flow Pattern and Total Force Coefficients for Forward Flight Cases of Calliphora for Second Case

Figures 7.25, 7.26 and 7.28 are illustrating the flow patterns for different forward velocities for the second case.

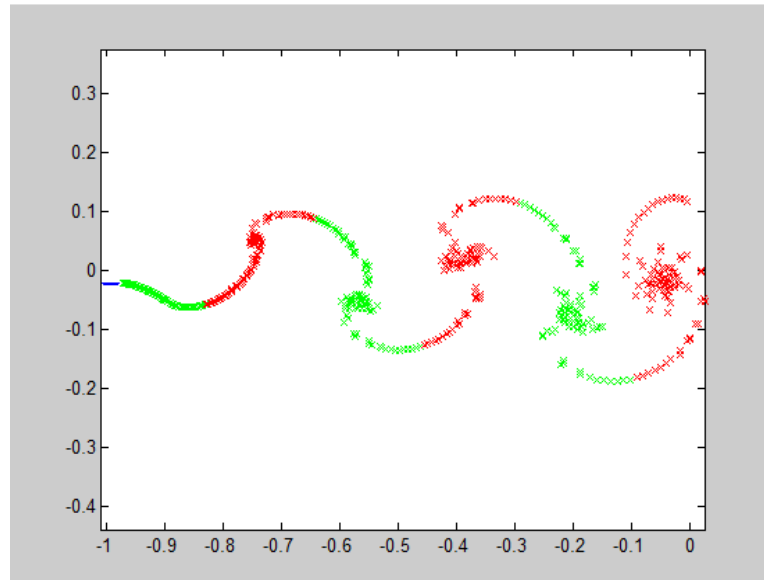


Figure 7.25 Flow Pattern obtained by mid-section (blue line) of Calliphora Wing
($A=85.90^\circ$, $f=5.85\text{Hz}$, $U= -2$ [m/s])

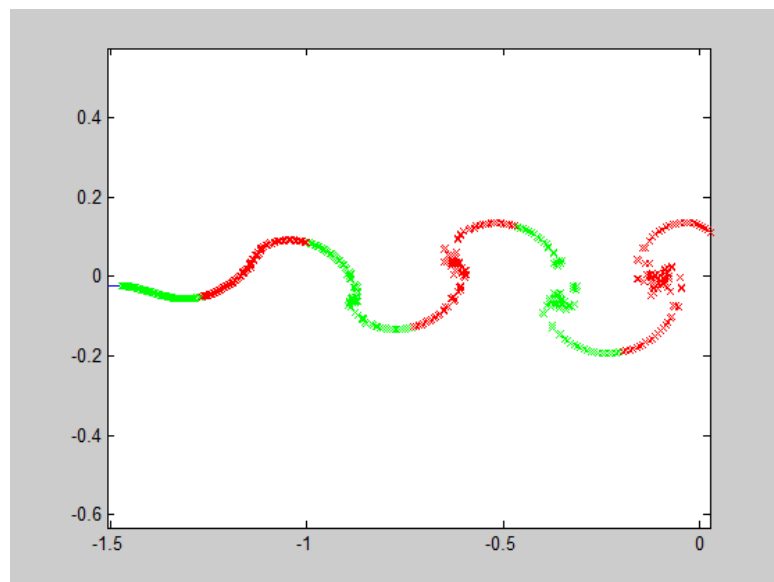


Figure 7.26 Flow Pattern obtained by mid-section (blue line) of Calliphora Wing
($A=85.90^\circ$, $f=5.85\text{Hz}$, $U= -3$ [m/s])

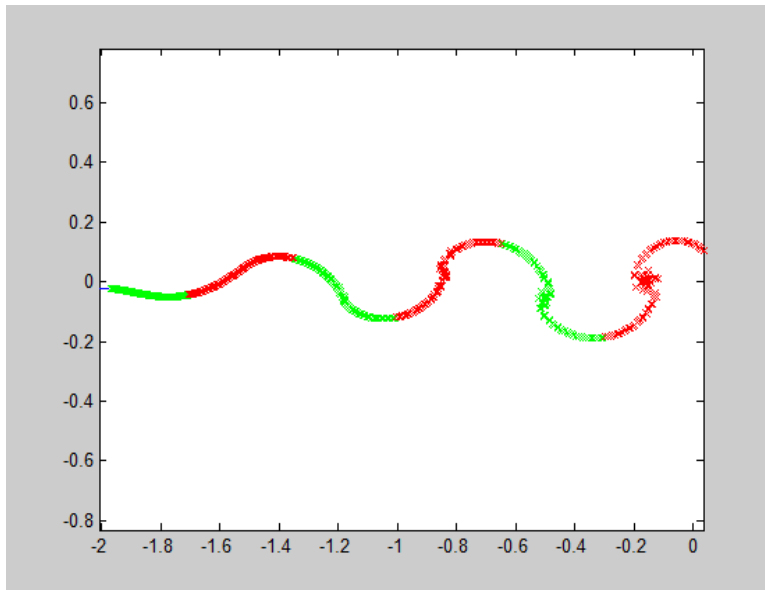


Figure 7.27 Flow Pattern obtained by mid-section (blue line) of Calliphora Wing
 ($A=85.90^\circ$, $f=5.85\text{Hz}$, $U= -4$ [m/s])

Figure 7.28 gives comparisons for lift coefficients for different forward velocities. Double the forward velocity results in nearly four times the value of maximum peak in lift coefficient results.

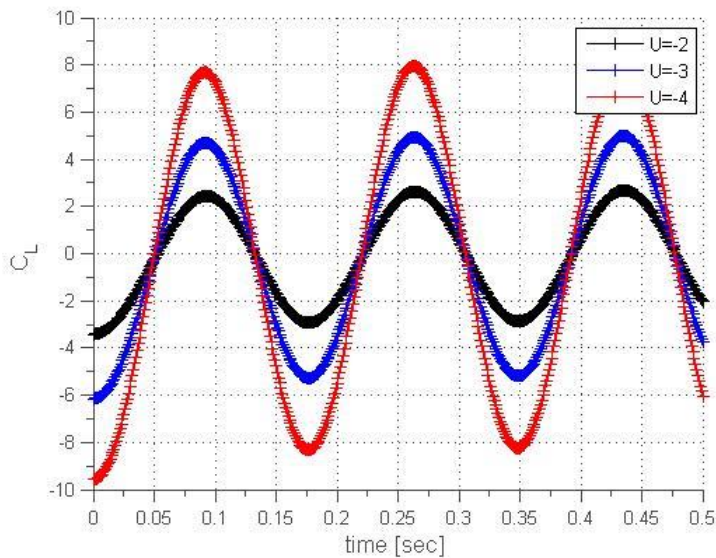


Figure 7.28 Comparison of Total Lift Coefficient on Calliphora having different forward velocities ($A=85.90^\circ$, $f=5.85\text{Hz}$) ($U=-2, -3, -4$ [m/s])

In Figure 7.29, the drag force coefficients are shown for different forward velocities.

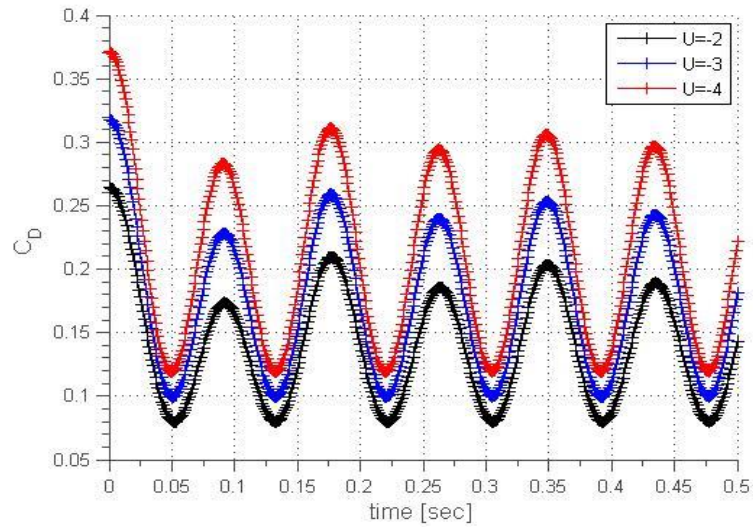


Figure 7.29 Comparison of Total Drag Coefficient on Calliphora having different forward velocities ($A=85.90^\circ$, $f=5.85\text{Hz}$) ($U=-2, -3, -4$ [m/s])

7.3.3.3 Comparison of 2-D Flow Pattern and Total Force Coefficients for Near Hover Cases of Calliphora for First Case

Since the frequency of the motion is higher compared to previous comparisons, this time for near-hover cases the pattern is more complicated. Figures 7.30, 7.31 and 7.32 are belong to near-hover flow pattern obtained by the first case.

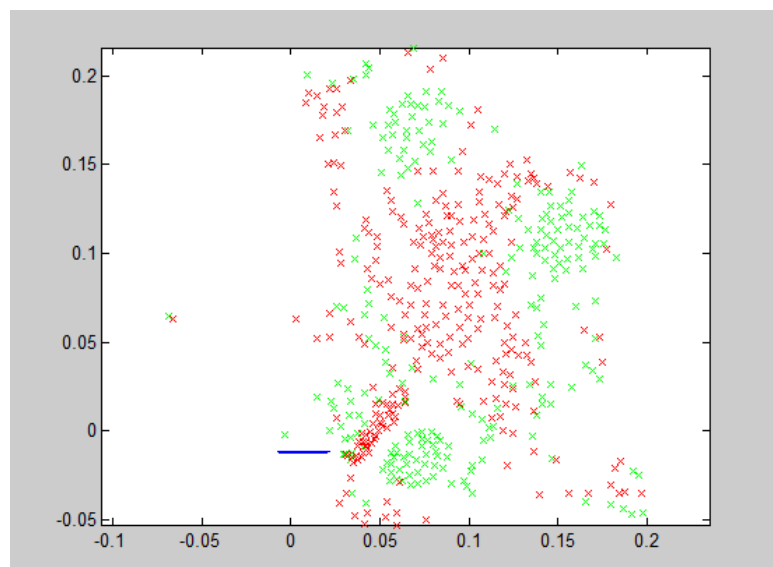


Figure 7.30 Flow Pattern obtained by mid-section (blue line) of Calliphora Wing ($A=41.52^\circ$,

$f=11.2 \text{ Hz}$, $U=0 \text{ [m/s]}$)

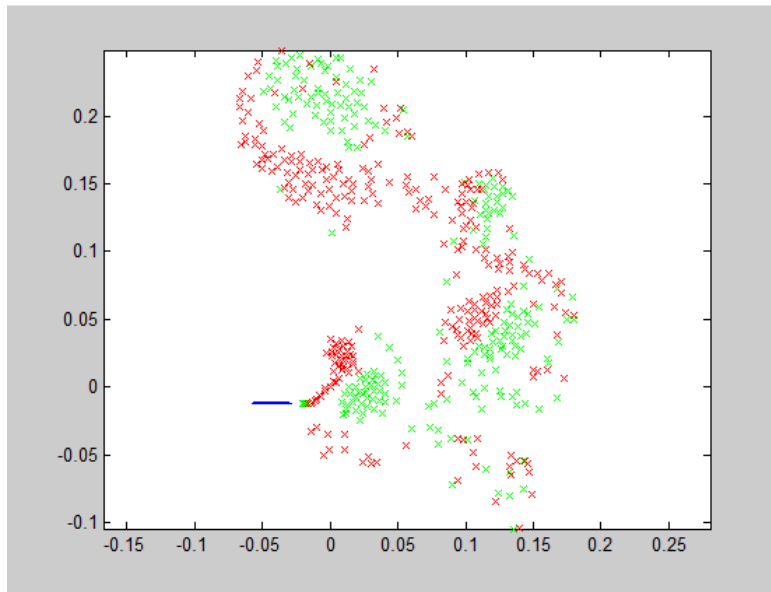


Figure 7.31 Flow Pattern obtained by mid-section (blue line) of Calliphora Wing
($A=41.52^\circ$, $f=11.2 \text{ Hz}$, $U=-0.1 \text{ [m/s]}$)

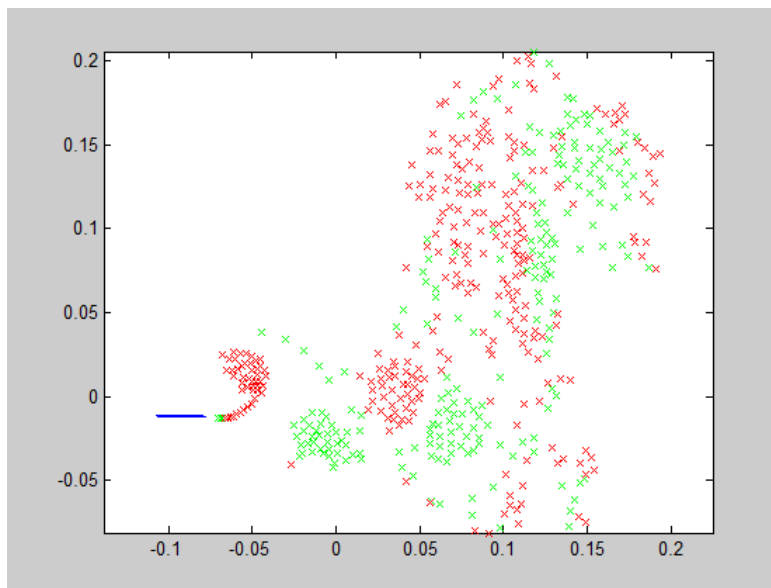


Figure 7.32 Flow Pattern obtained by mid-section (blue line) of Calliphora Wing
($A=41.52^\circ$, $f=11.2 \text{ Hz}$, $U=-0.2 \text{ [m/s]}$)

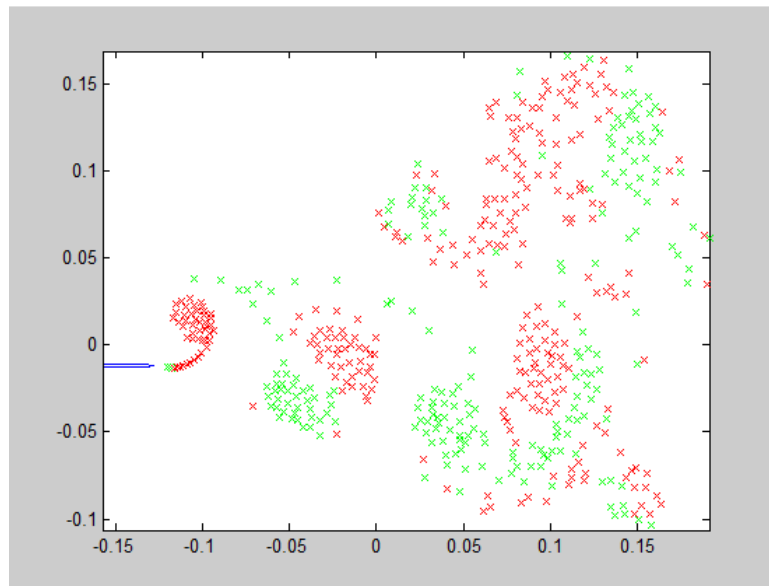


Figure 7.33 Flow Pattern obtained by mid-section (blue line) of Calliphora Wing
 ($A=41.52^\circ$, $f=11.2$ Hz, $U=-0.3$ [m/s])

Similarly, the lift and drag force coefficients were compared as seen in Figures 7.34 and 7.35. Lift force coefficients have smaller peaks earlier strokes than previously illustrated 10th stroke. However, for the drag force coefficients only peaks on the negative side show higher amplitudes. For more detailed comments, more cases should be tested by the analytical model and the model should be improved due to other unsteady effects.

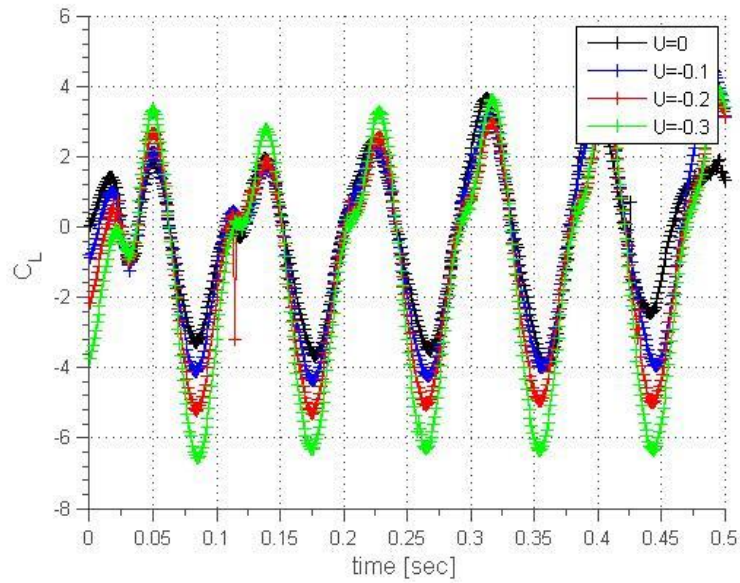


Figure 7.34 Comparison of Total Lift Coefficient on Calliphora having different near hover velocities ($A=41.52^\circ$, $f=11.2$ Hz) ($U=0, -0.1, -0.2, -0.3$ [m/s])

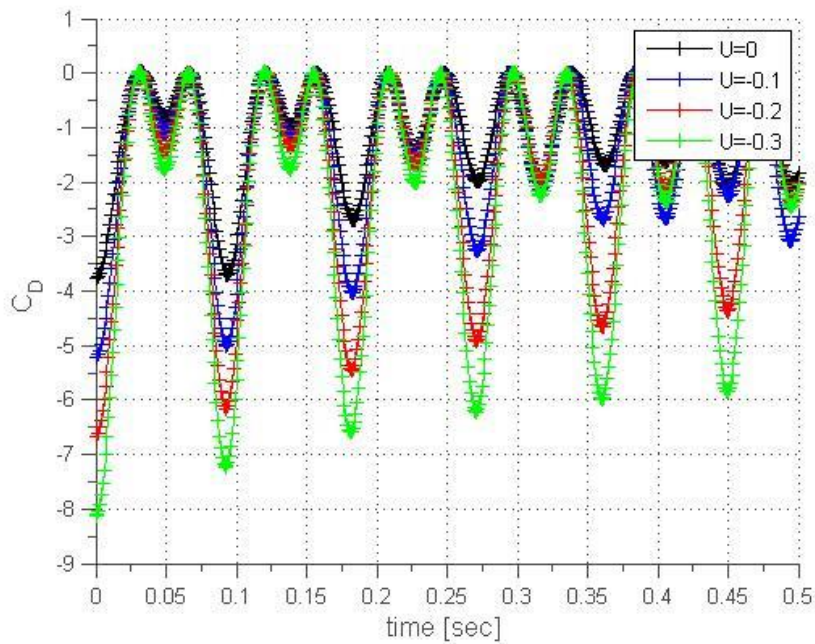


Figure 7.35 Comparison of Total Drag Coefficient on Calliphora having different near hover velocities ($A=41.52^\circ$, $f=11.2$ Hz) ($U=0, -0.1, -0.2, -0.3$ [m/s])

7.3.4 Comparison of Sectional Pressure Distributions from CFD and Simulink

7.3.4.1 Pressure Distribution Comparison with CFD Results for 10th period data of First Case for Hover ($A=41.52^\circ$, $f=11.2\text{Hz}$)

To explain the differences in force coefficients, sectional pressure distributions were compared for 3 span-wise stations of Calliphora wing. Figures 7.36, 7.37, 7.38, 7.39, 7.40, 7.41 and 7.42 are illustrating sectional pressure distributions obtained by the wing positions at specific times for hover for the first case from root to tip.

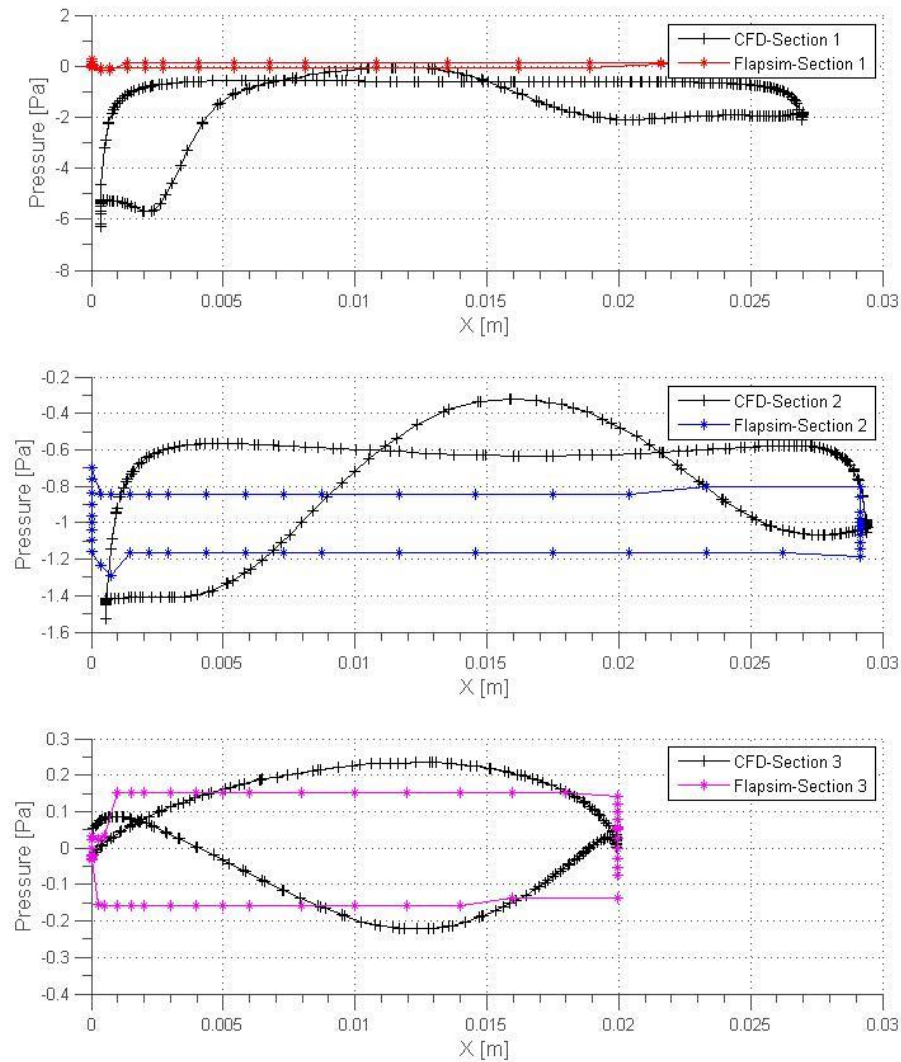


Figure 7.36 Pressure Distribution Comparison at 0.905 [sec]

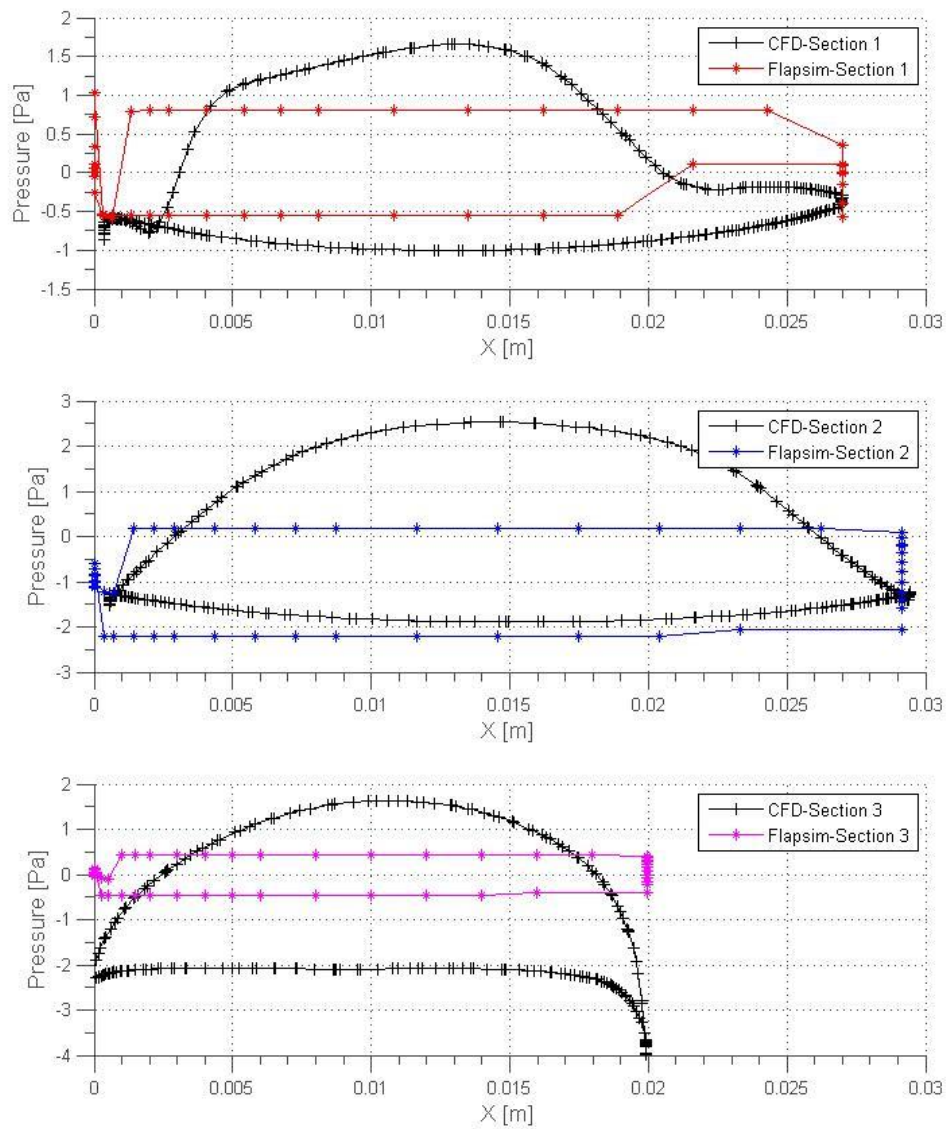


Figure 7.37 Pressure Distribution Comparison at 0.915 [sec]

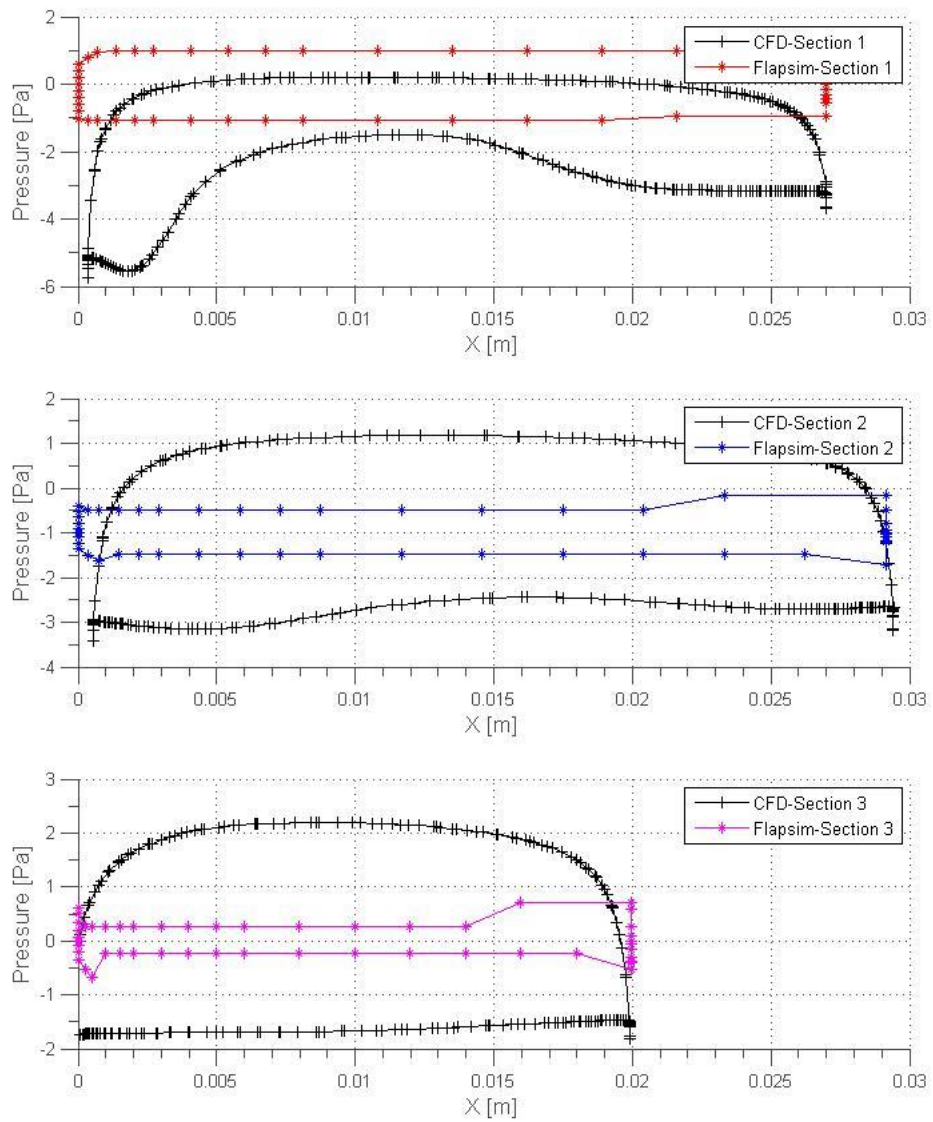


Figure 7.38 Pressure Distribution Comparison at 0.94 [sec]

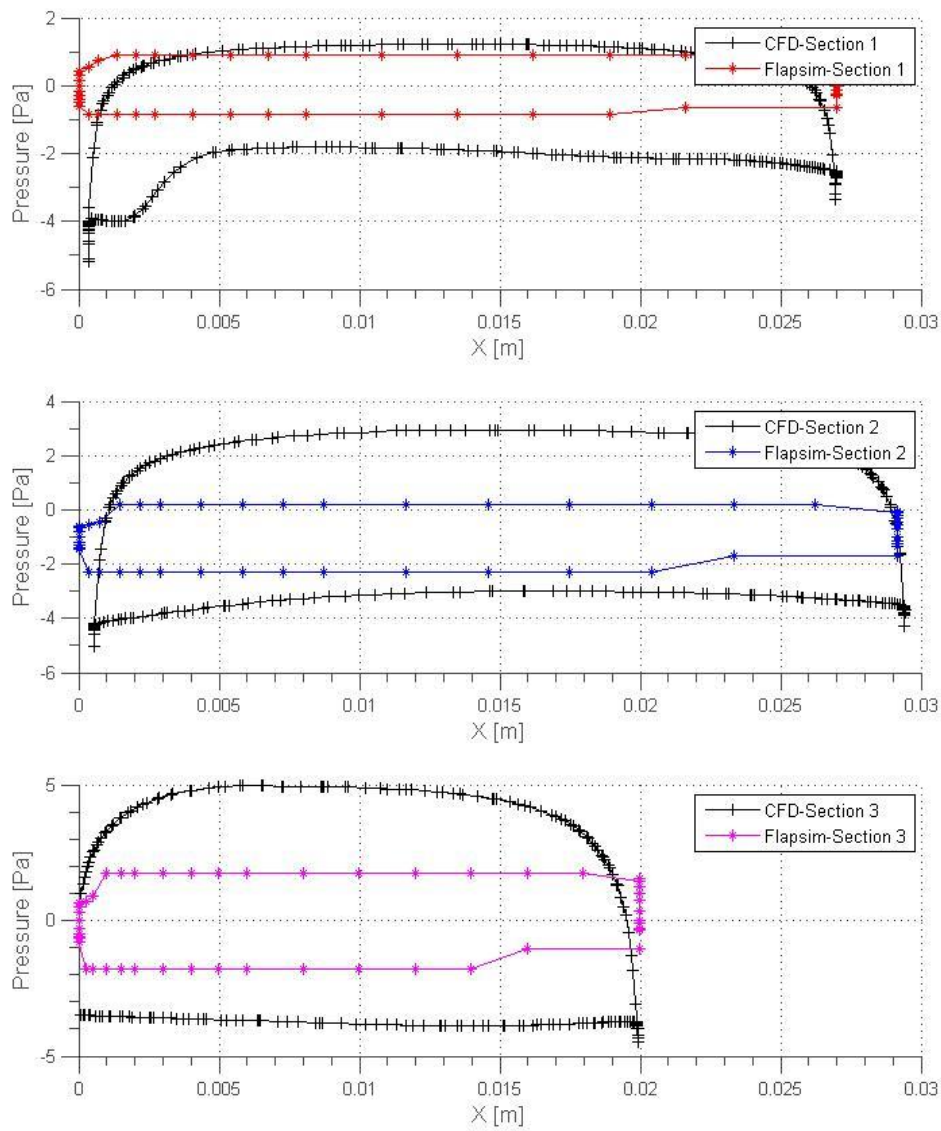


Figure 7.39 Pressure Distribution Comparison at 0.975 [sec]

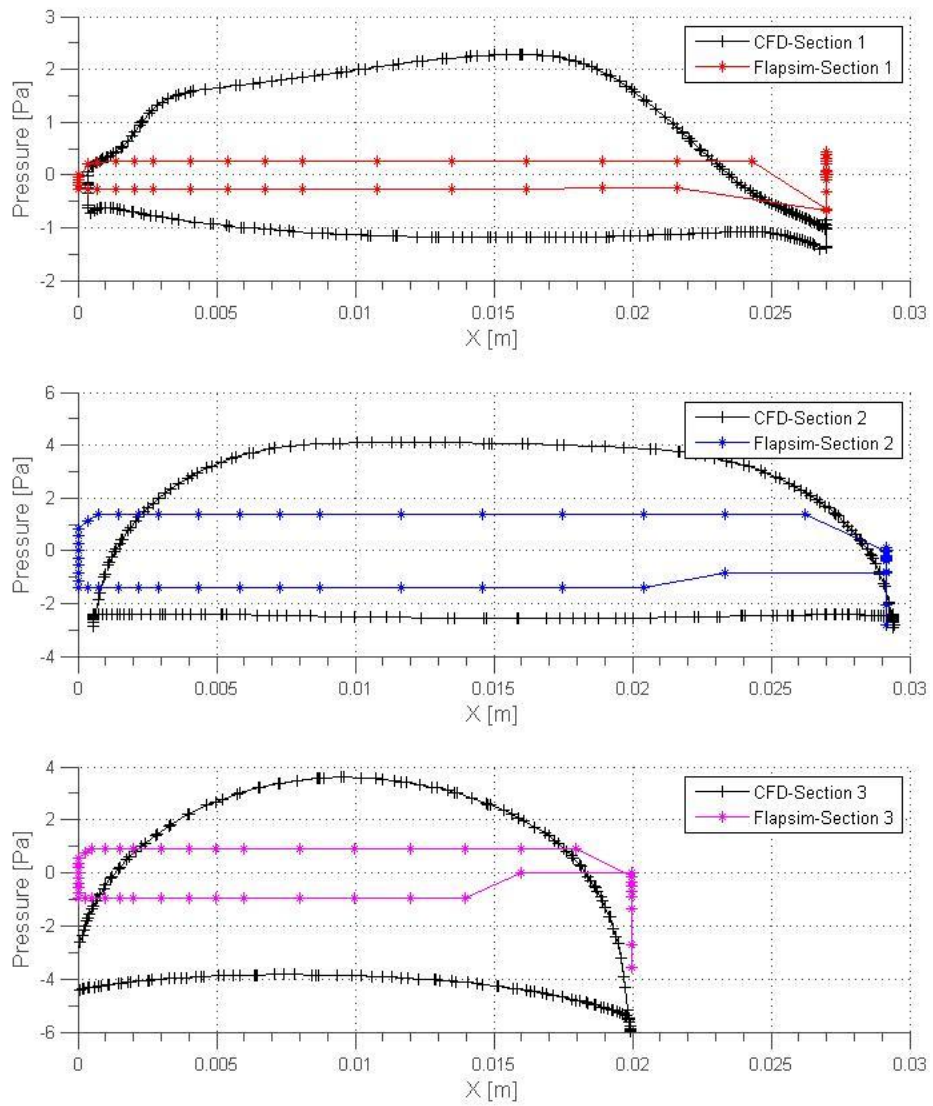


Figure 7.40 Pressure Distribution Comparison at 0.965 [sec]

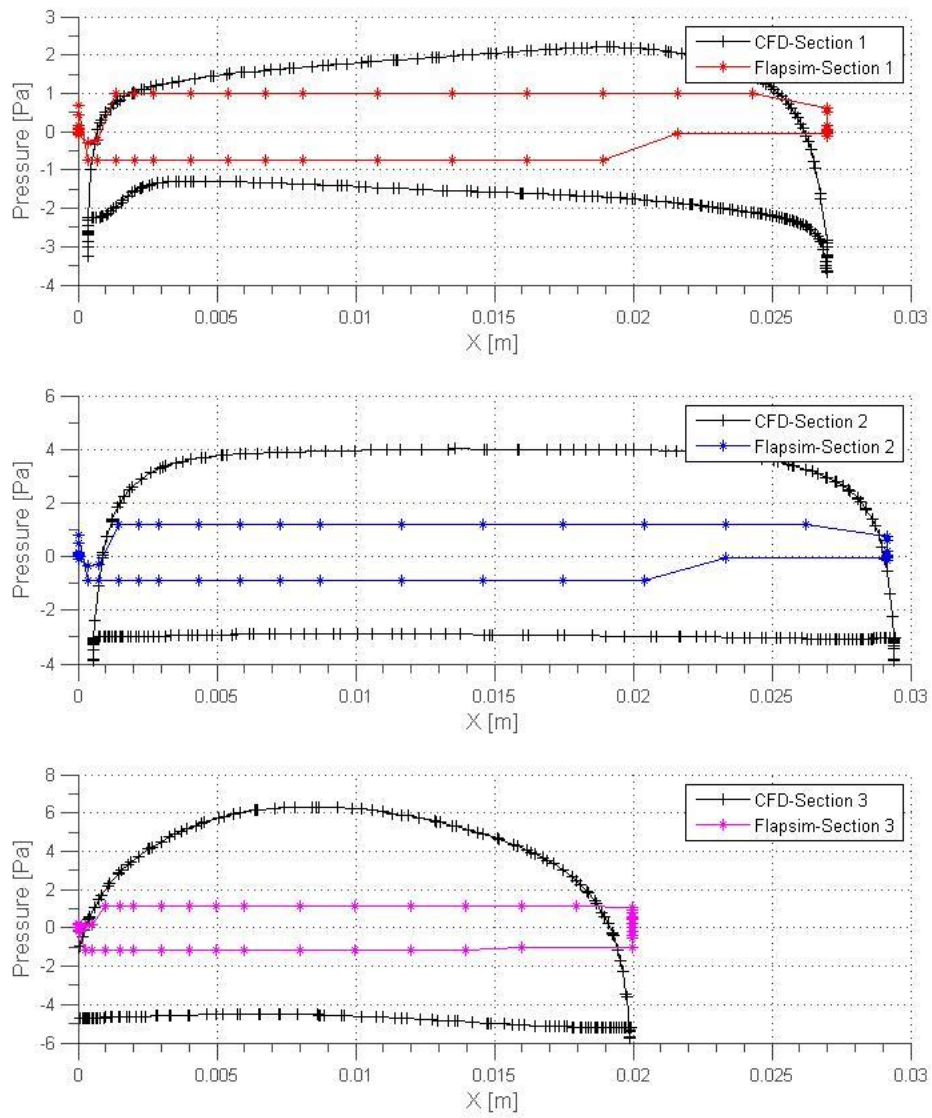


Figure 7.41 Pressure Distribution Comparison at 0.925 [sec] at C_L max

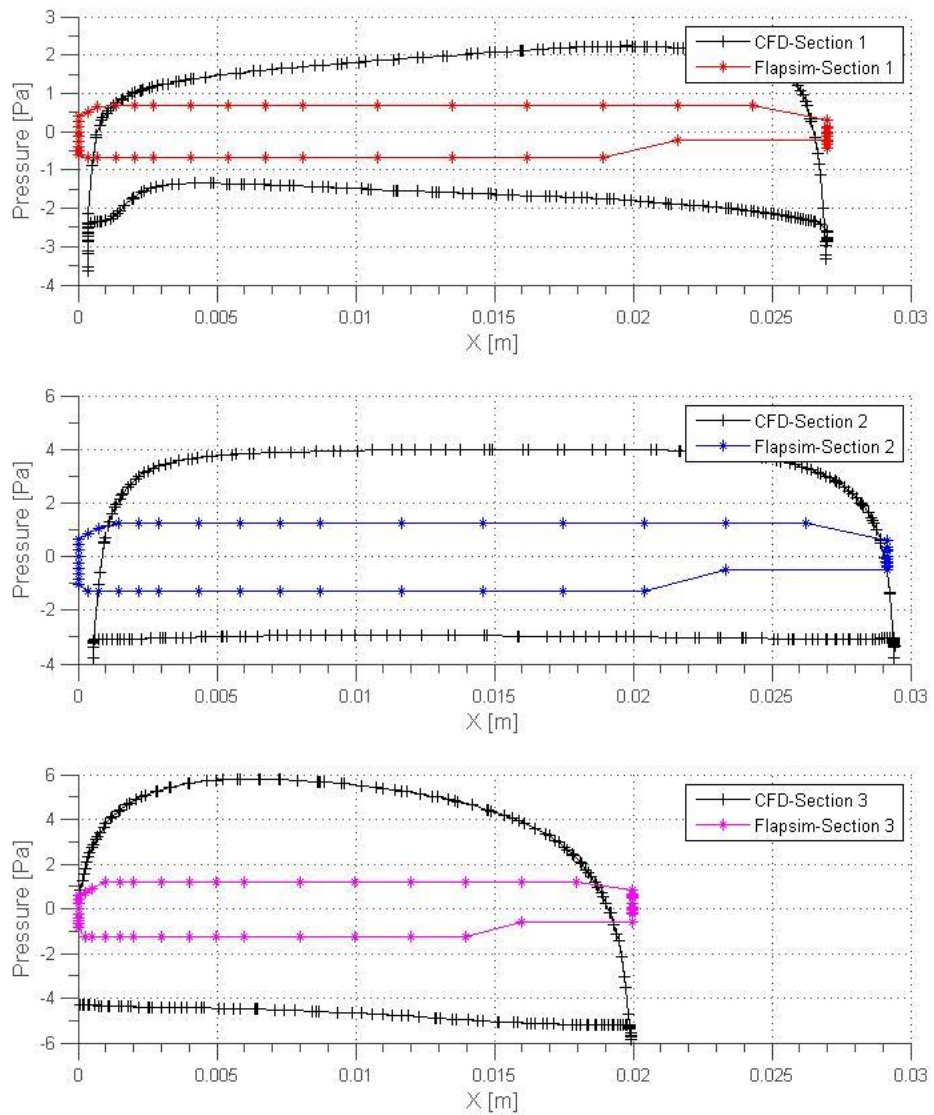


Figure 7.42 Pressure Distribution Comparison at 0.97 [sec] at C_L min

7.3.4.2 Pressure Distribution Comparison with CFD Results for 4th period data of Second Case for Hover ($A=85.90^\circ$, $f=5.85\text{Hz}$)

Similarly Figures 7.43, 7.44, 7.45, 7.46, 7.47 and 7.48 are showing sectional pressure distributions in hover for the second case from root to tip.

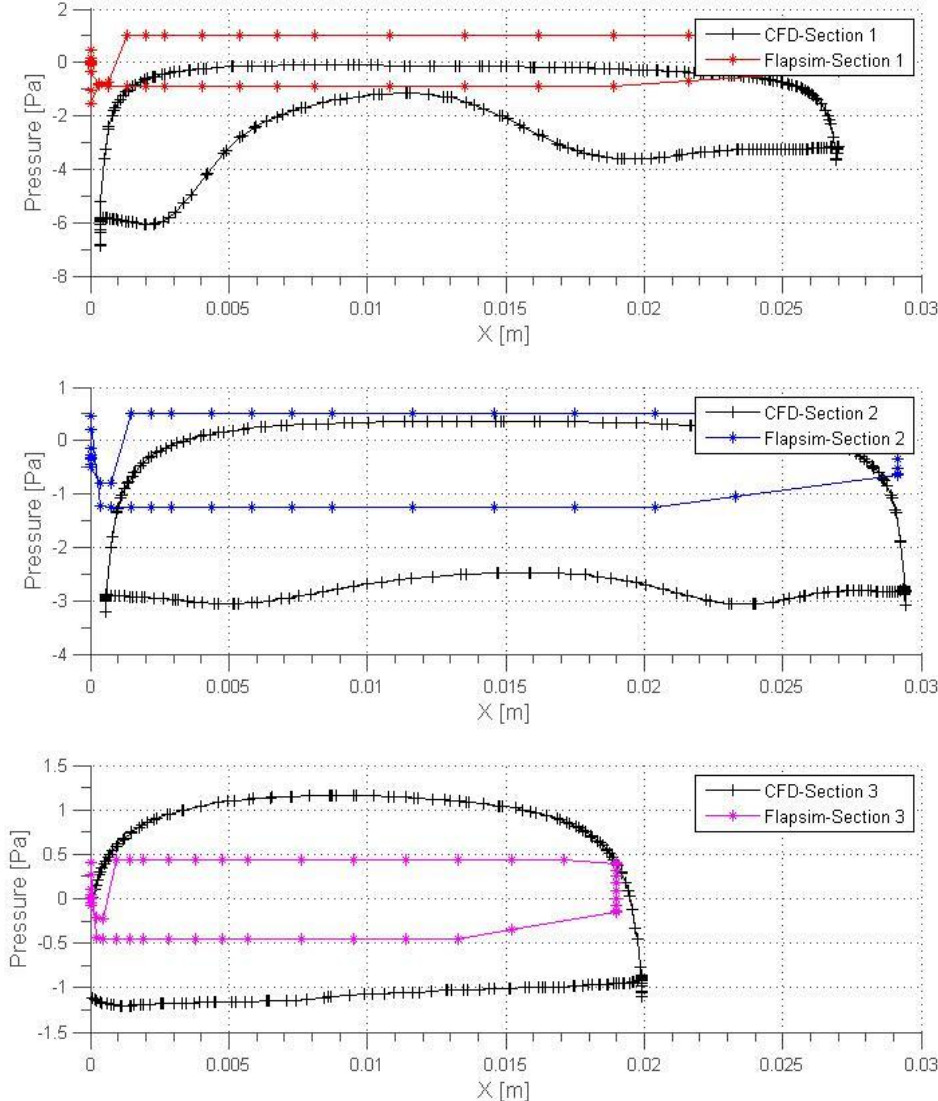


Figure 7.43 Pressure Distribution Comparison at 0.7 [sec]

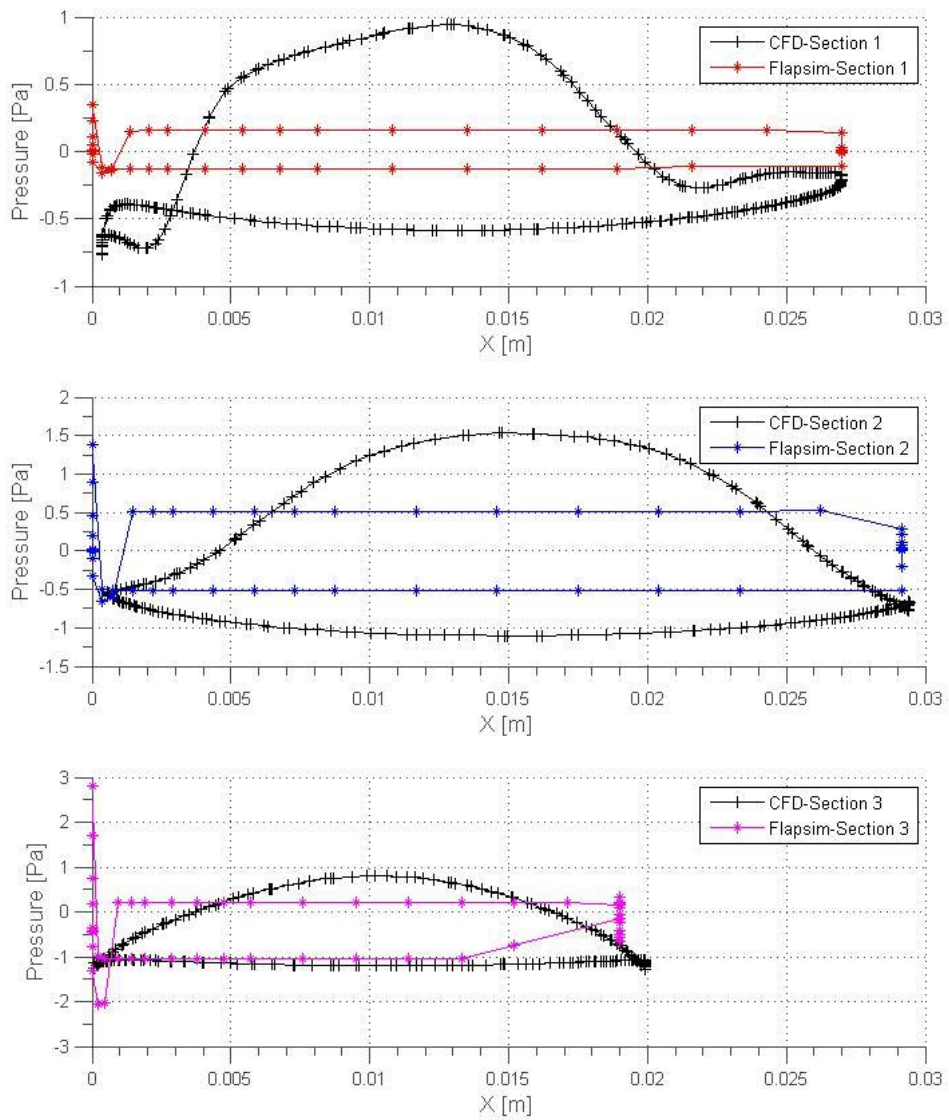


Figure 7.44 Pressure Distribution Comparison at 0.725 [sec]

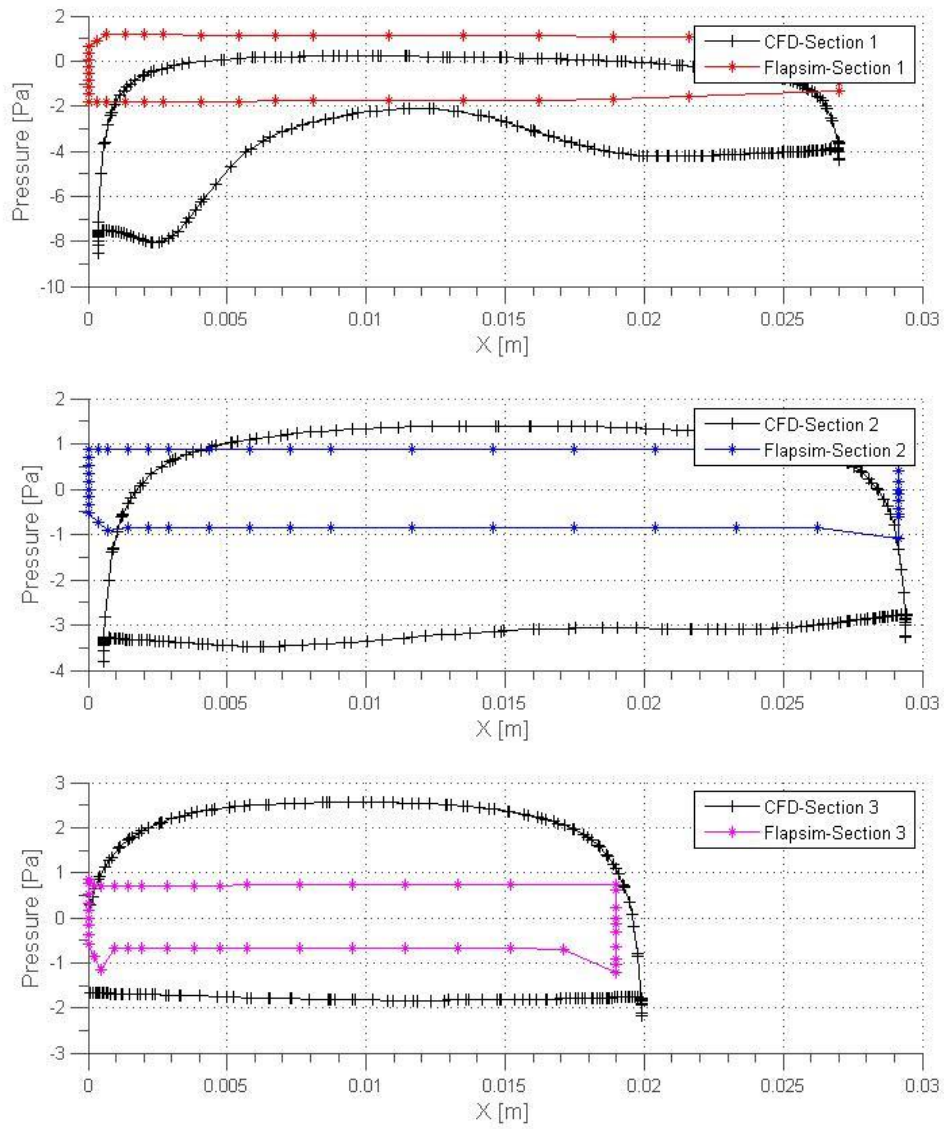


Figure 7.45 Pressure Distribution Comparison at 0.77 [sec] at C_L max

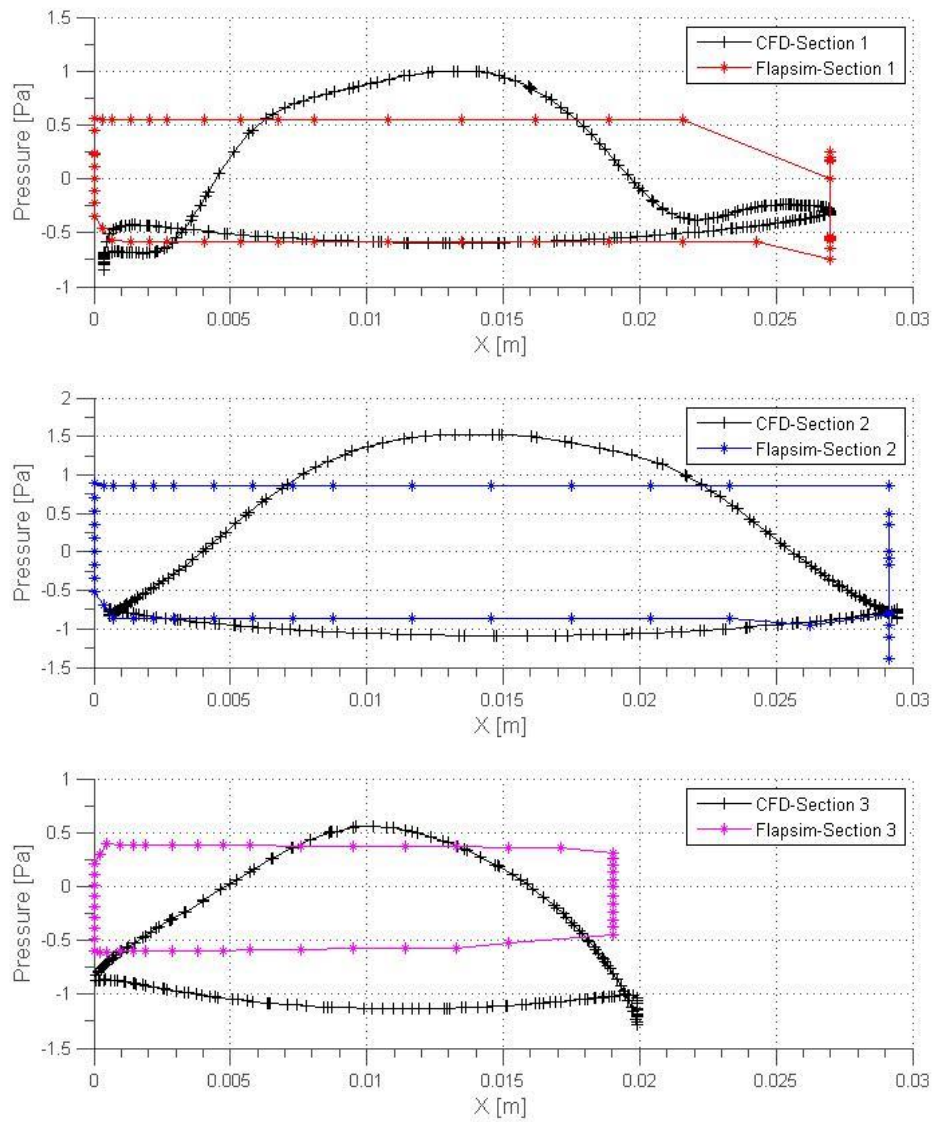


Figure 7.46 Pressure Distribution Comparison at 0.81[sec]

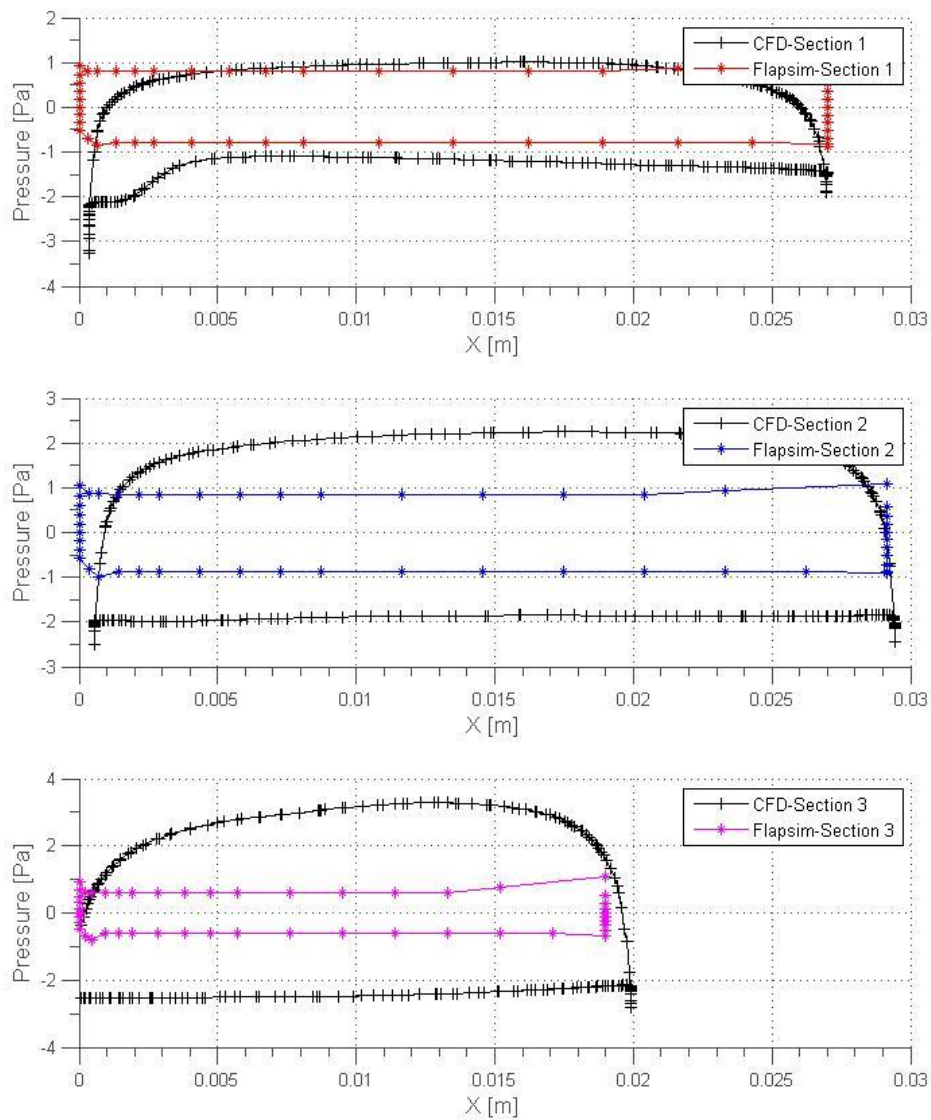


Figure 7.47 Pressure Distribution Comparison at 0.83 [sec]

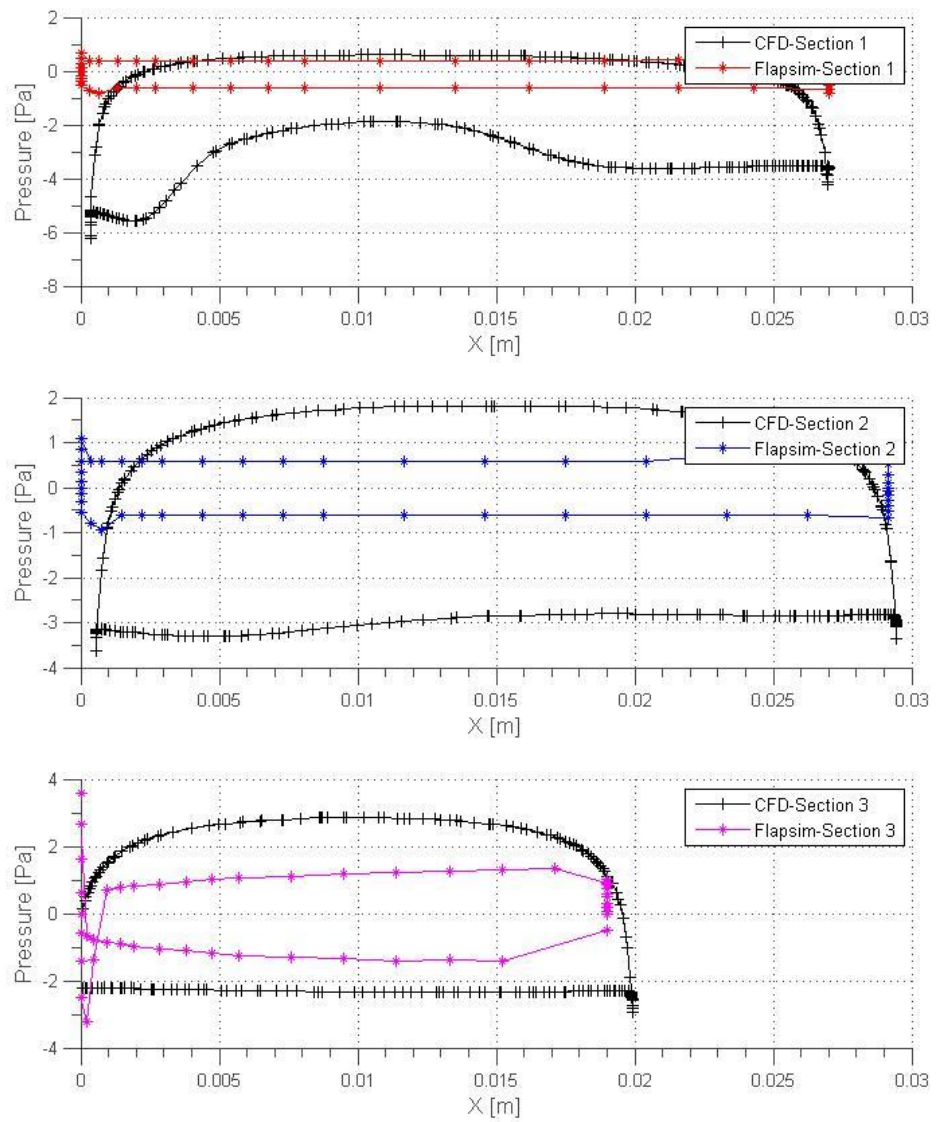


Figure 7.48 Pressure Distribution Comparison at 0.845 [sec] at C_L min

7.3.4.3 Pressure Distribution Comparison with CFD Results for 4th period data of Second Case for Forward Flight ($A=85.90^\circ$, $f=5.85\text{Hz}$)

Since the hover cases are affected by leading edge vortices strongly, it is decided to compare pressure results for forward flight. Figures 7.49, 7.50, 7.51, 7.52, 7.53, 7.54, 7.55, 7.56, 7.57 and 7.58 are illustrating sectional pressure distributions for forward flight ($U=-3\text{m/s}$) from root to tip.

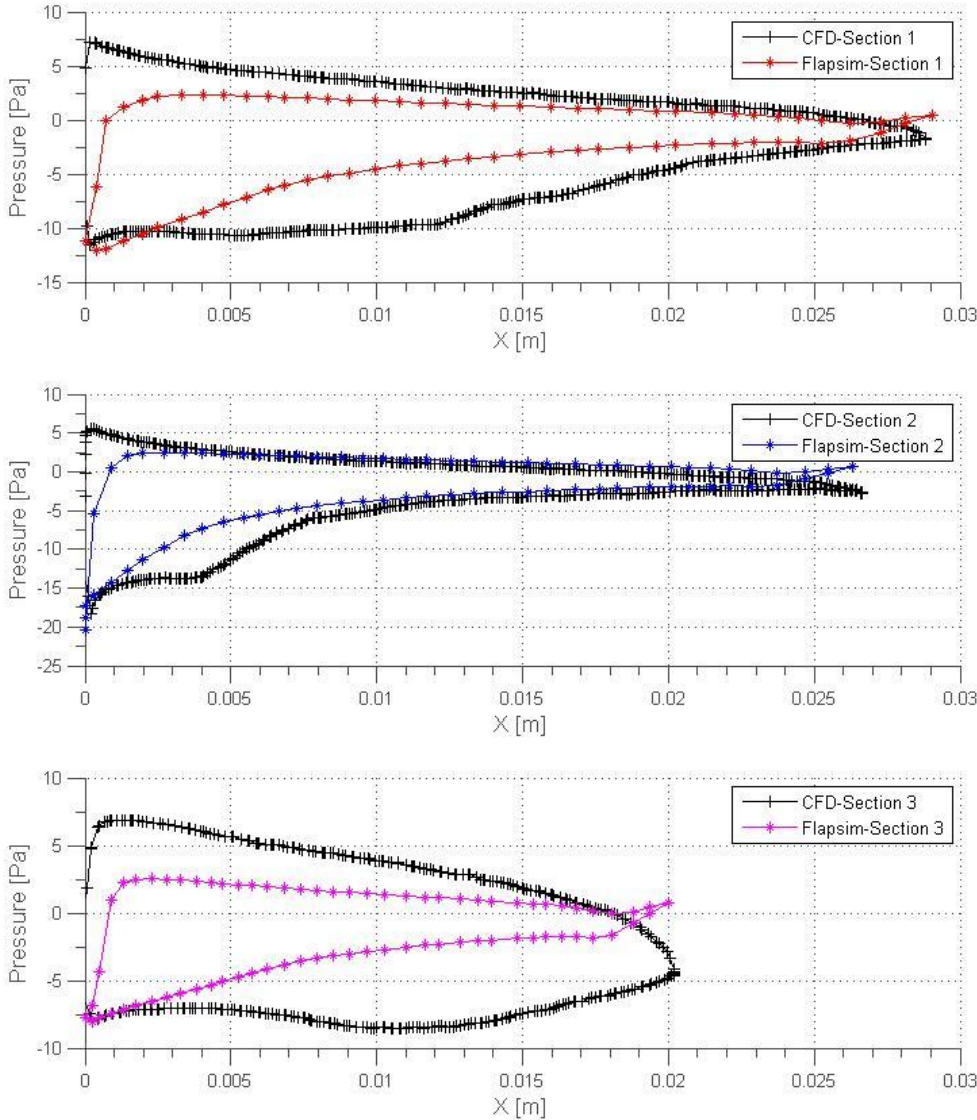


Figure 7.49 Pressure Distribution Comparison at 0.68 [sec]

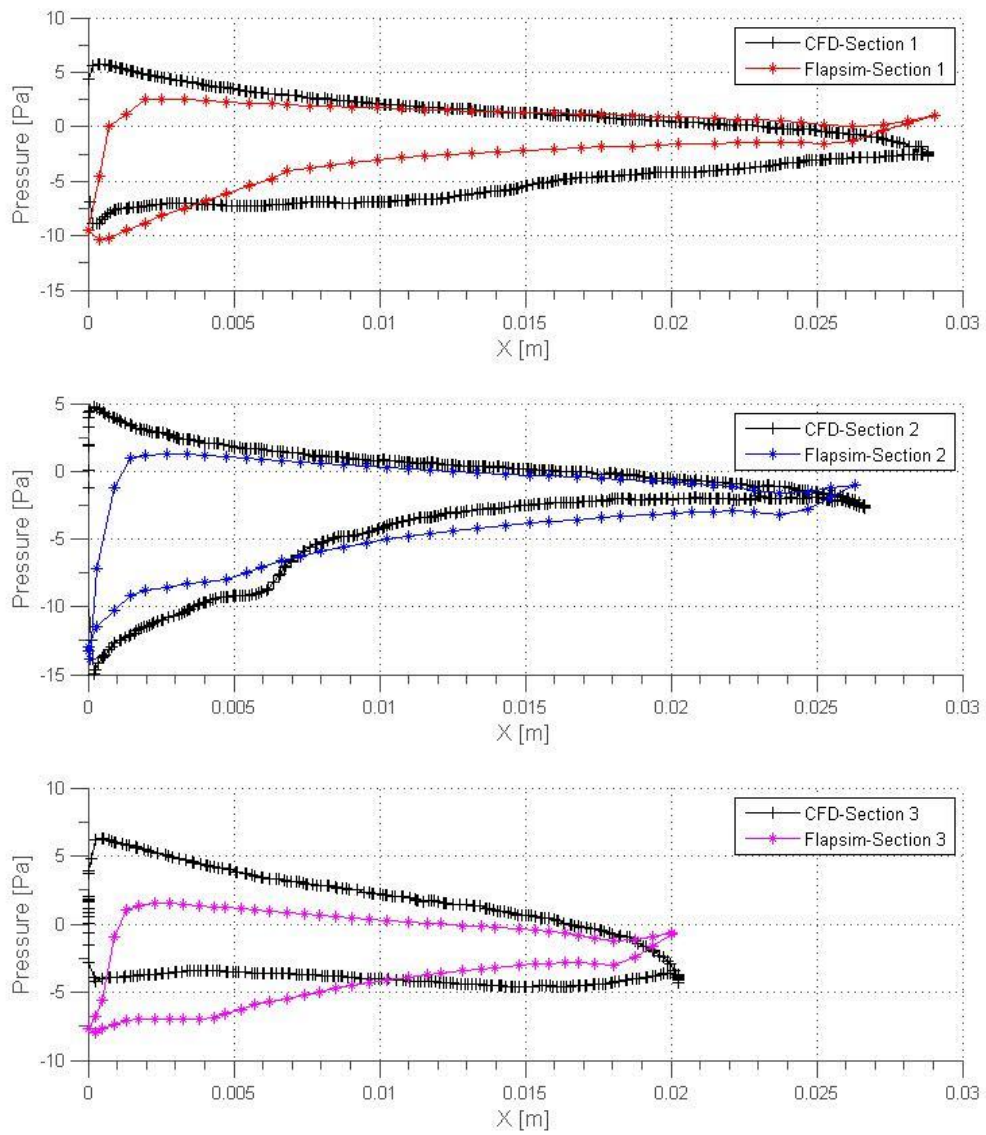


Figure 7.50 Pressure Distribution Comparison at 0.70 [sec]

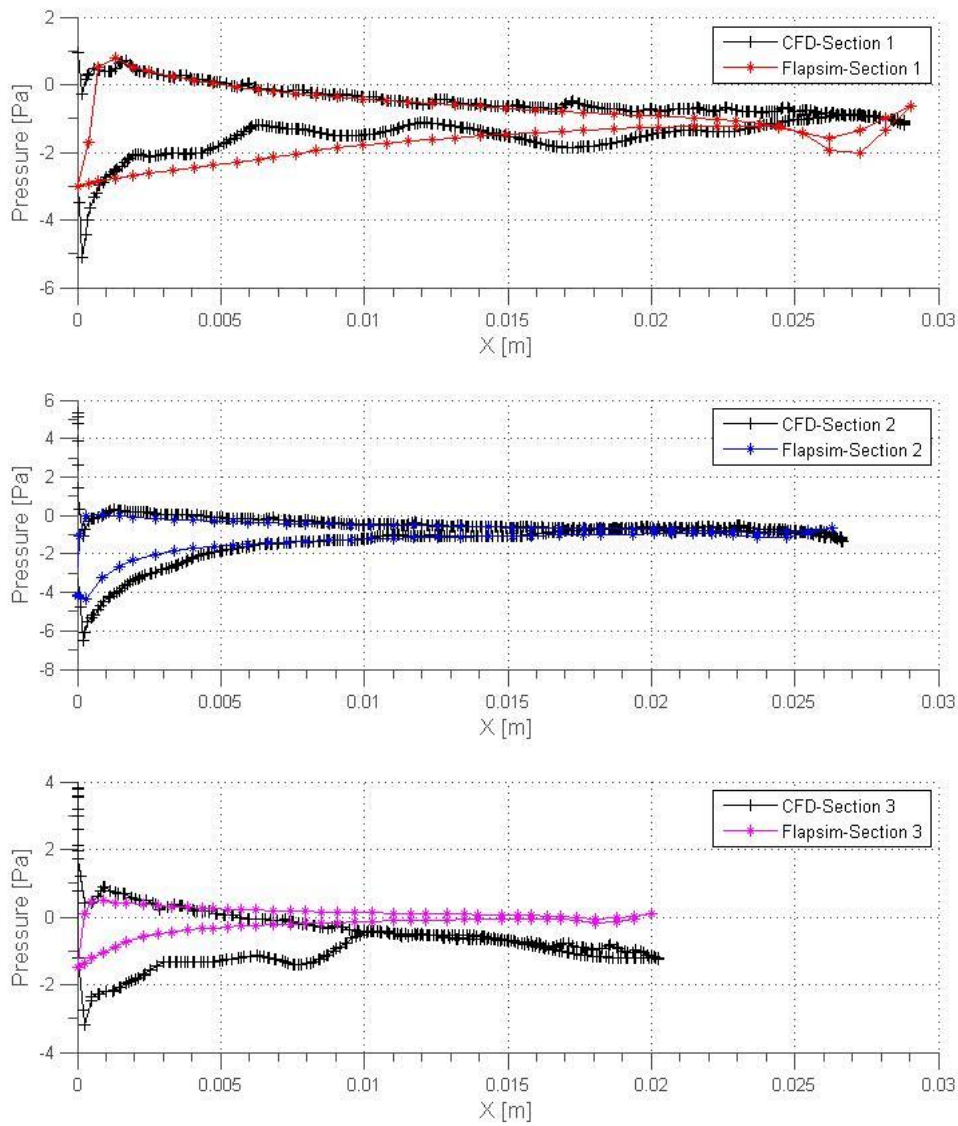


Figure 7.51 Pressure Distribution Comparison at 0.72 [sec]

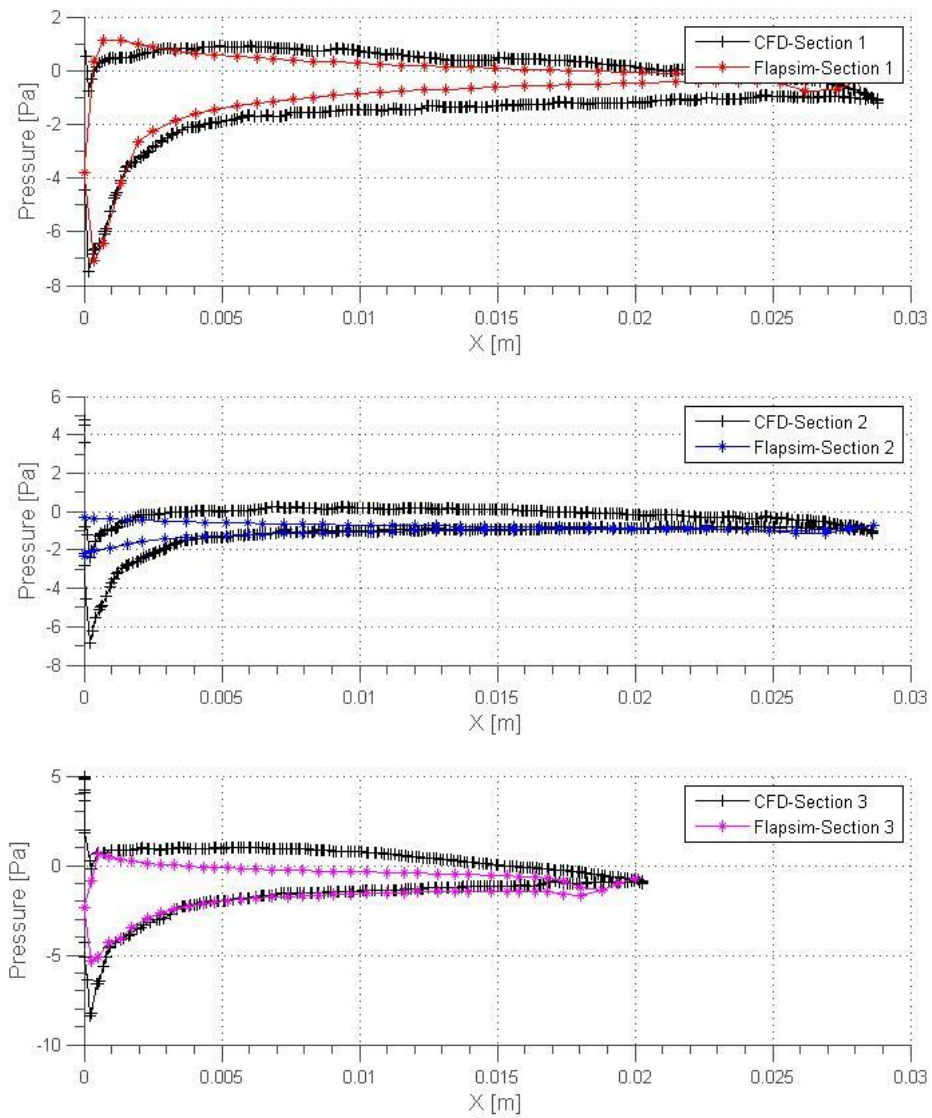


Figure 7.52 Pressure Distribution Comparison at 0.73 [sec]

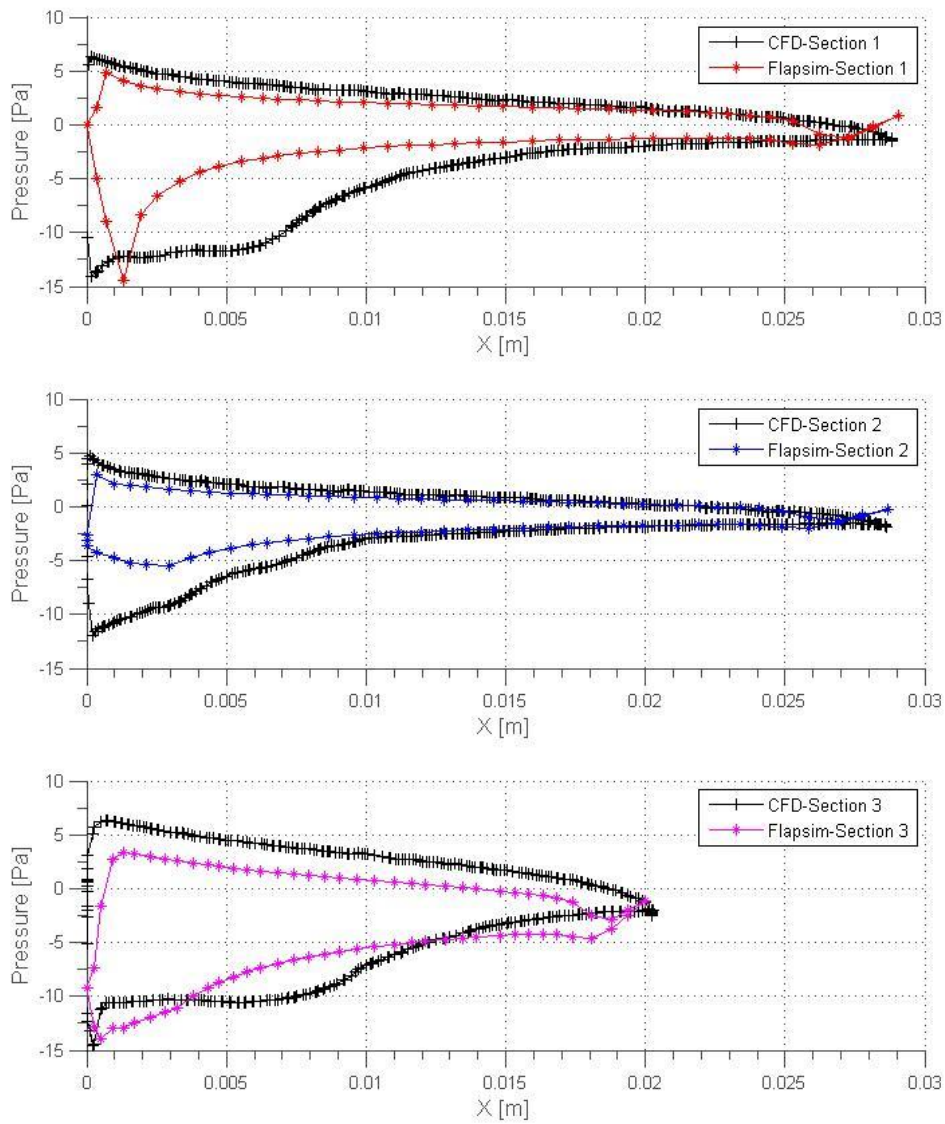


Figure 7.53 Pressure Distribution Comparison at 0.75 [sec]

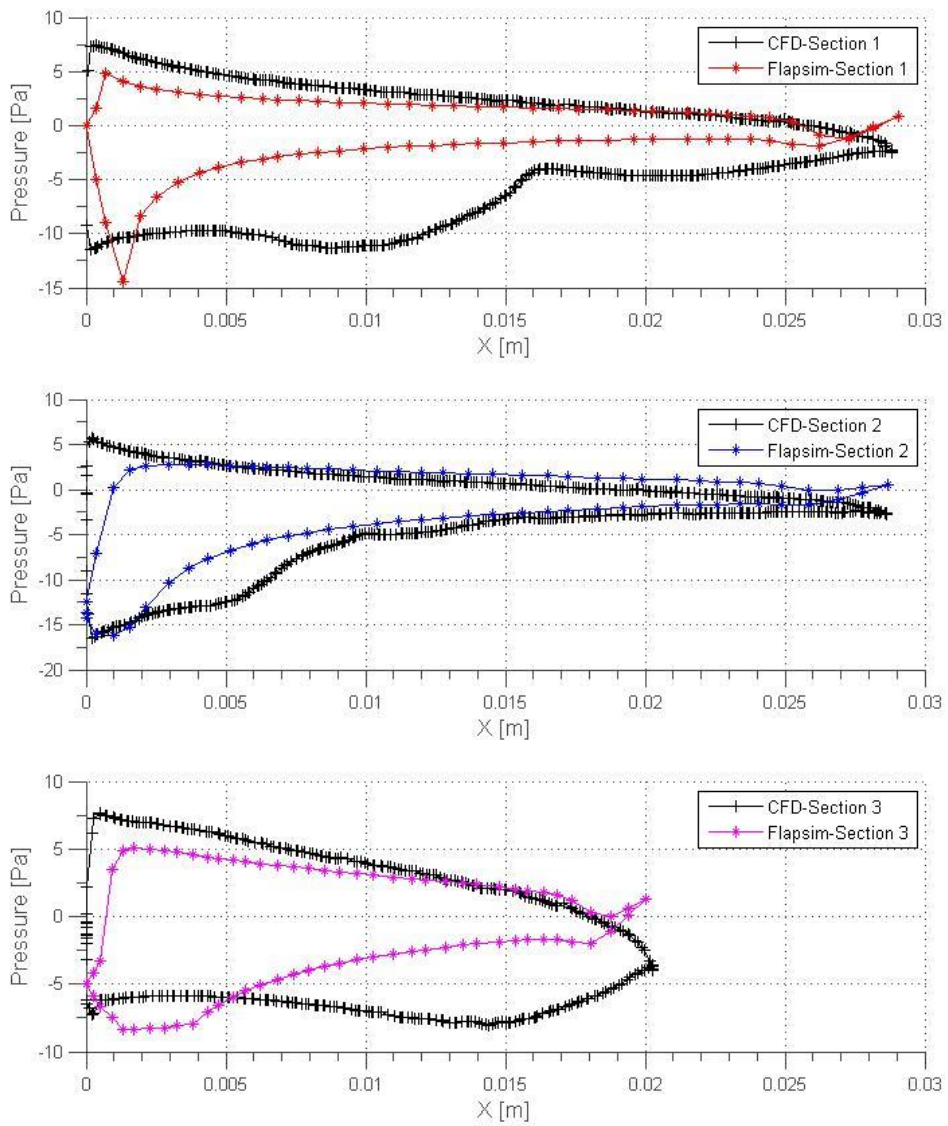


Figure 7.54 Pressure Distribution Comparison at 0.77 [sec] at C_L max

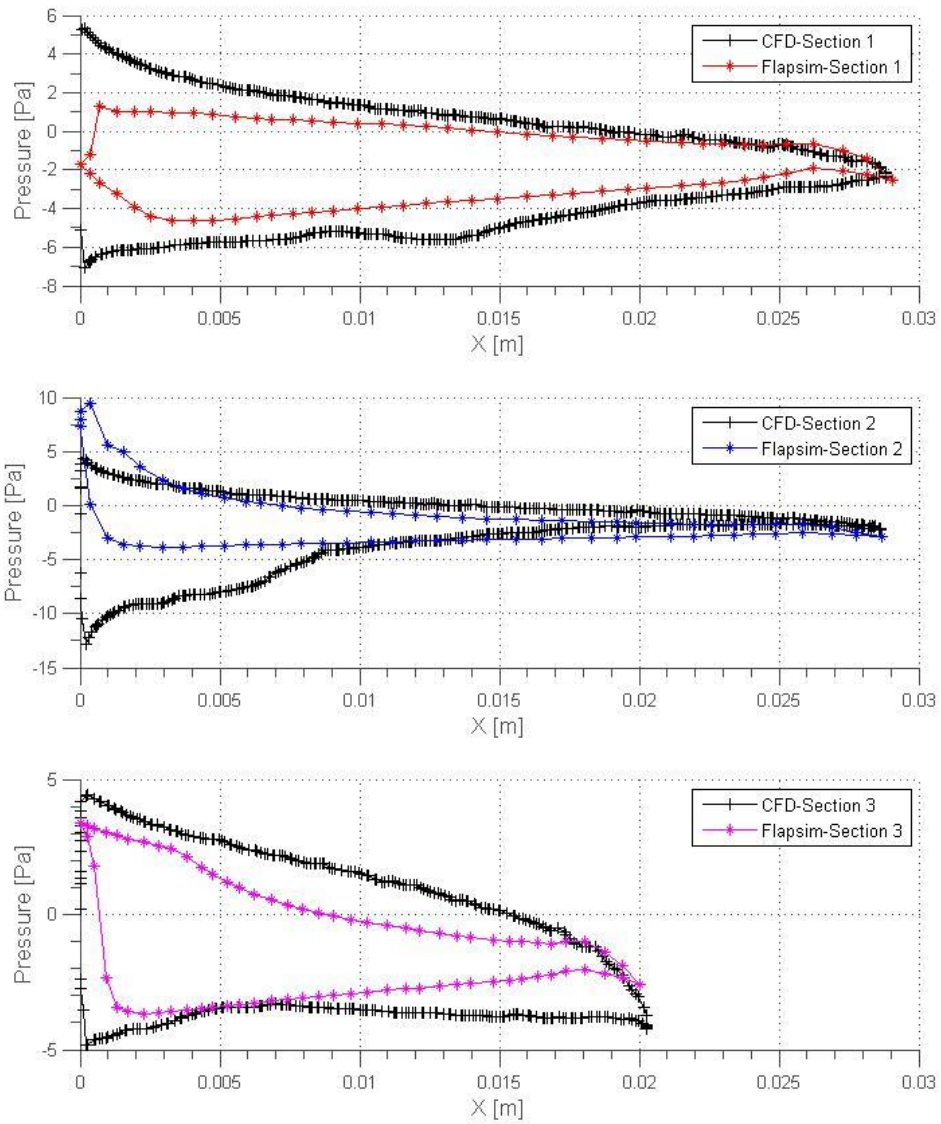


Figure 7.55 Pressure Distribution Comparison at 0.79 [sec]

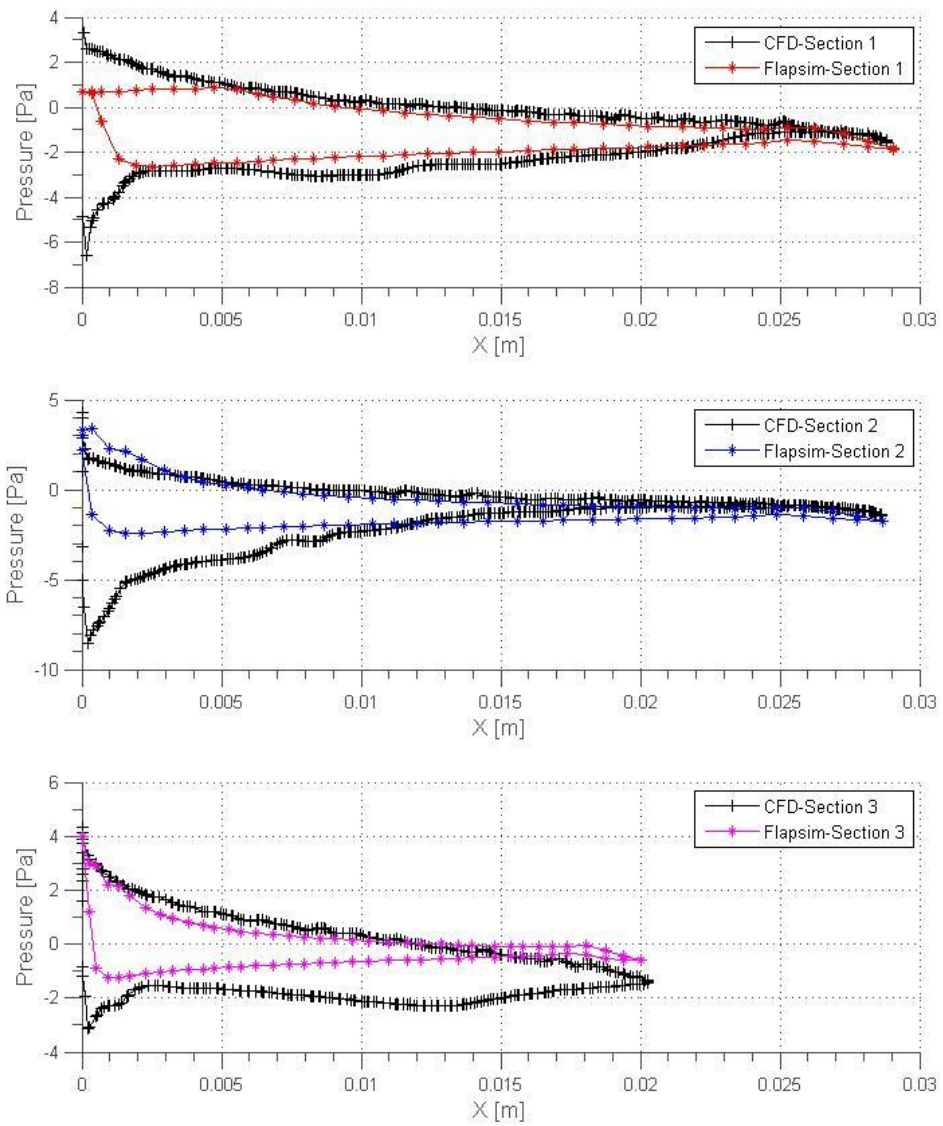


Figure 7.56 Pressure Distribution Comparison at 0.80 [sec]

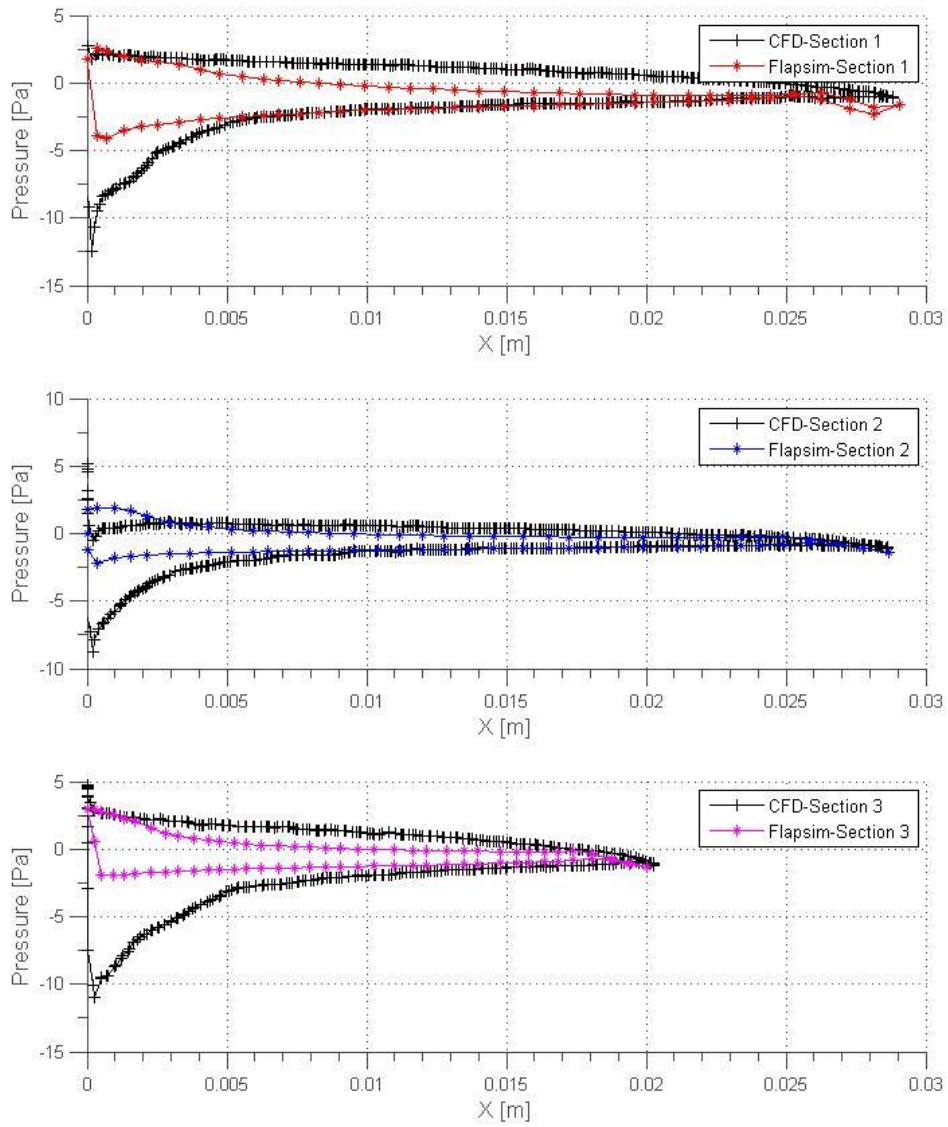


Figure 7.57 Pressure Distribution Comparison at 0.82 [sec]

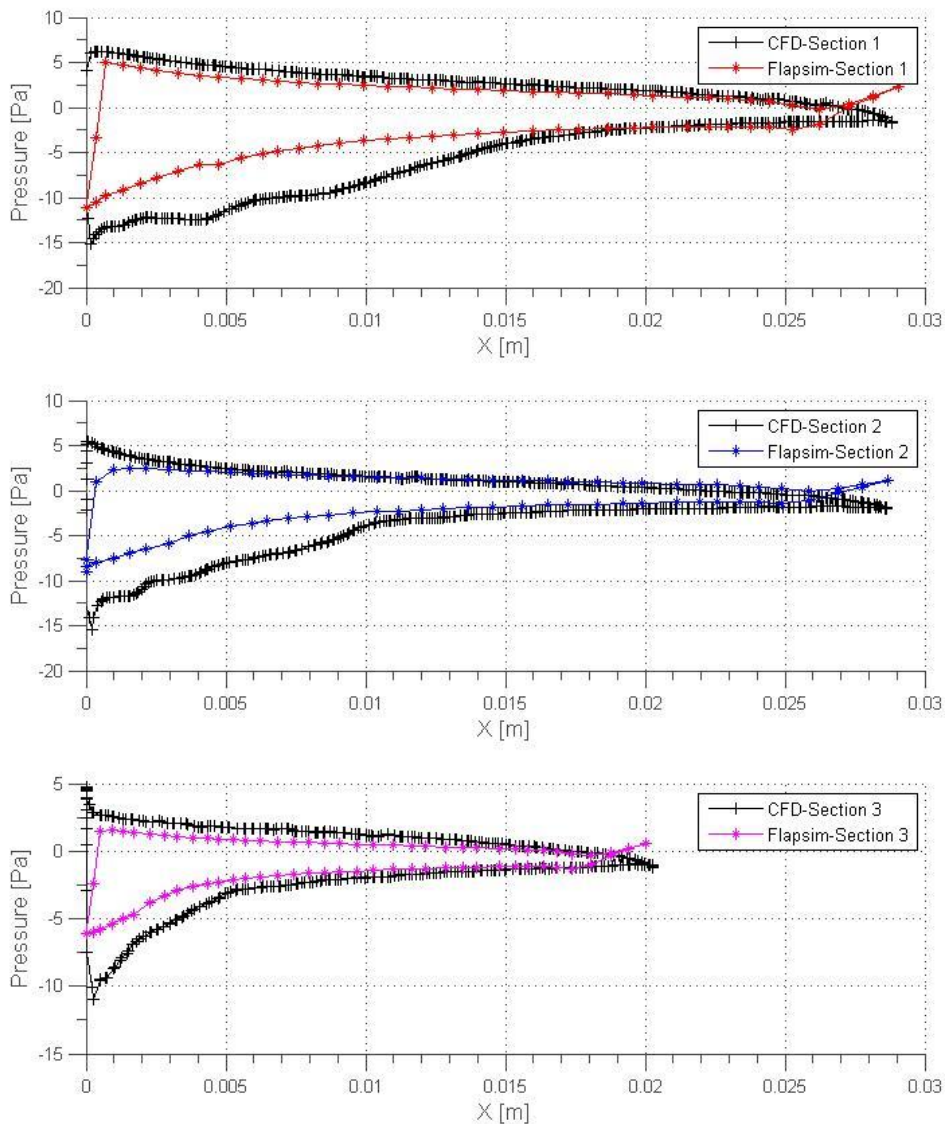


Figure 7.58 Pressure Distribution Comparison at 0.84 [sec] at C_L min

As seen in pressure distribution results for forward flight case, the more numbers of panel points compared to hover cases are used on the wing section to gather pressure data. The reason for that is; in the forward flight case, the distribution has fluctuations while in hover cases the pressure values are stable through upper and lower surface. Also the trailing edge is sharpened a little bit, to reach a converged results since the Kutta Condition should be satisfied.

The pressure distributions are typical for zero angle of attack case obtained by panel algorithm. Higher angle of attack causes the peak in leading edge to be higher.

7.4 Results for Heaving Flat Wing

The model parameters for Flat wing both defined in present Simulink model and UDF functions of Fluent Analysis by Senol [41], which the results are compared are shown in Table 7-5.

Table 7-5 Flat Plate Wing Parameters

Span	b= 0.05847 [m]
Surface Area	A=1.7044*10 ⁻³ [m ²]
Max Velocity	V=1.35 [m/s]
Density	ρ =1.225 [kg/m ³]

The lift coefficient is defined as;

$$C_L = \frac{L}{\frac{1}{2}\rho V^2 A} \quad (7.5)$$

The denominator of the Equation 7.5 is found as; 1.9023* 10⁻³N for Flat Wing Model. Therefore all force results found in Simulink model is divided by this value and multiplied with the trigonometric expression according to Figure 3.2 to compare with the results of aerodynamic force coefficients obtained by CFD.

As in Calliphora Case, the wing is divided into 3, 5 and 11 station-wise strips for span-wise force integration as in Figures 7.59-7.60 and 7.61. The results are compared with the CFD simulations given by Senol [41]



Figure 7.59 Flat Wing with 3 Span-wise Sections

Table 7-6 Chord values, Radial Distances and Unit lengths for Flat Wing for Case 1

Station #	1	2	3
c	0.02915m	0.02915m	0.02915m
R	0.034m	0.054m	0.074m
dx	0.01949m	0.01949m	0.01949

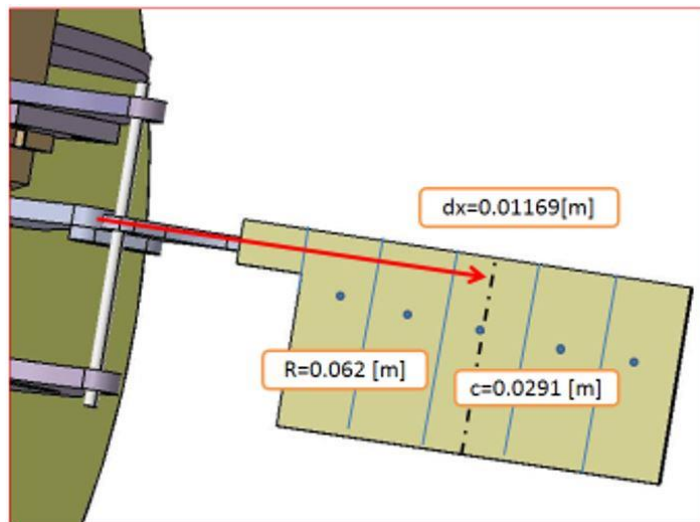


Figure 7.60 Flat Wing with 5 Span-wise Sections

Table 7-7 Chord values, Radial Distances and Unit lengths for Flat Wing for Case 2

Station #	1	2	3	4	5
c	0.02915m	0.02915m	0.02915m	0.02915m	0.02915m
R	0.029m	0.038m	0.005m	0.062m	0.074
dx	0.011694m	0.011694m	0.011694m	0.011694m	0.011694m

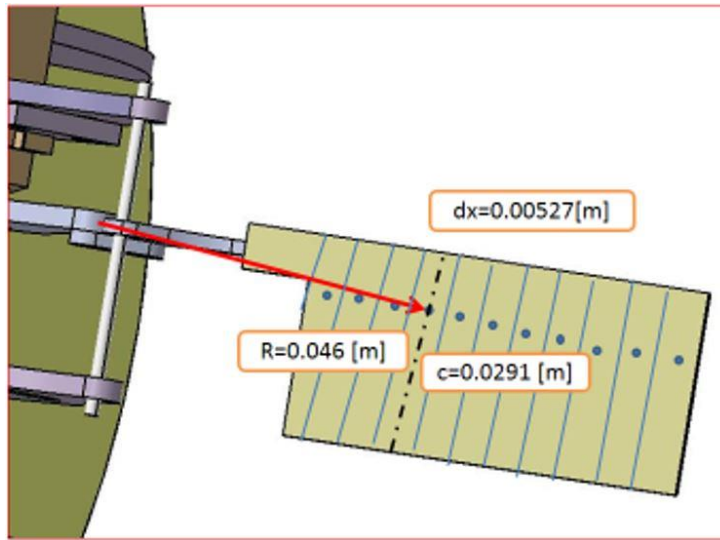


Figure 7.61 Flat Wing with 11 Span-wise Sections

Table 7-8 Chord values, Radial Distances and Unit lengths for Flat Wing for Case 3

Station #	1	2	3	4	5
c	0.02915m	0.02915m	0.02915m	0.02915m	0.02915m
R	0.031m	0.036m	0.041m	0.046m	0.051m
dx	0.005272m	0.005272m	0.005272m	0.005272m	0.005272m
6	7	8	9	10	11
0.02915m	0.02915m	0.02915m	0.02915m	0.02915m	0.02915m
0.056m	0.061m	0.066m	0.071m	0.076m	0.081m
0.0052727	0.0052727	0.005272m	0.005272m	0.005272m	0.005272m

Similar to the procedure performed for the Calliphora wing, Flat plate wing is divided into span-wise stations for the integration of pressure forces. However, this time the chord lengths were same for all stations but they differ in linear velocities due to radial positions of stations. The force comparison due to number of span-wise sections are not much different than comparison for Calliphora wing. This supports the idea that the pressure forces obtained by unsteady panel algorithm are not strongly affected by the chord length as also stated by Prosser [25].

Although the lift coefficients comparably agree well with CFD simulations, drag force does not fit properly. This is due to viscous effects and combination of other wake effects that are included in CFD Solver. Therefore, the validation of pressure values on a section at a time is performed as in Calliphora case. The results are very close to Calliphora since 2-D Panel algorithm is not affected by the chord length too much as also stated by Prosser [25].

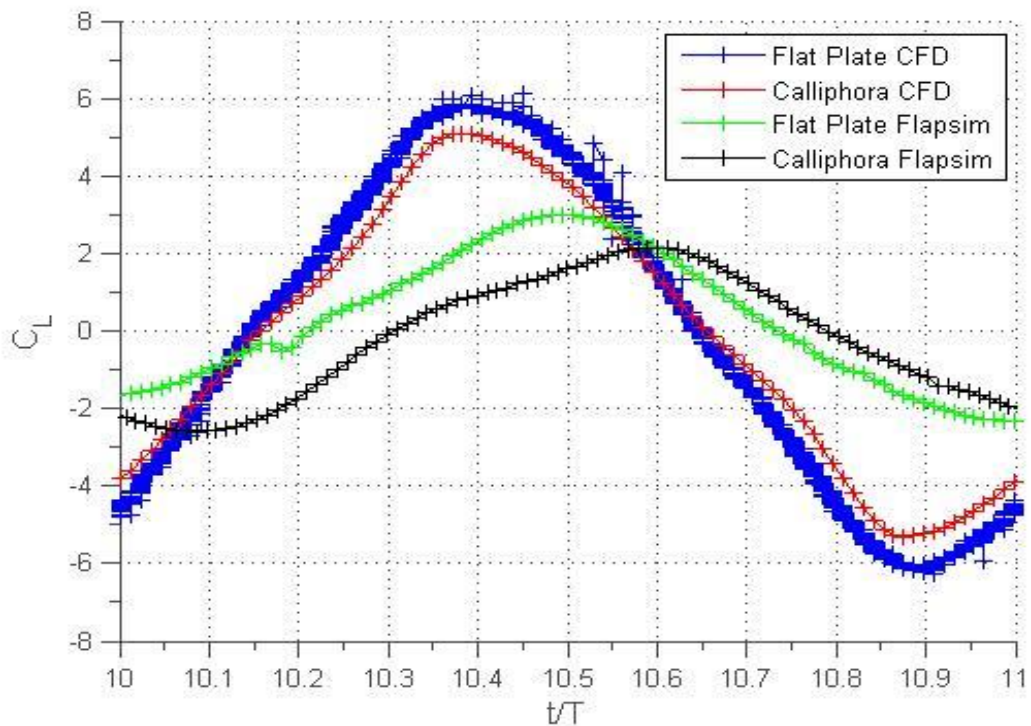


Figure 7.62 Comparison of Lift Coefficient for the First Case 10th period ($A=41.52^\circ$, $f=11.2$ Hz) in Hover due to Span-wise Wing Shape

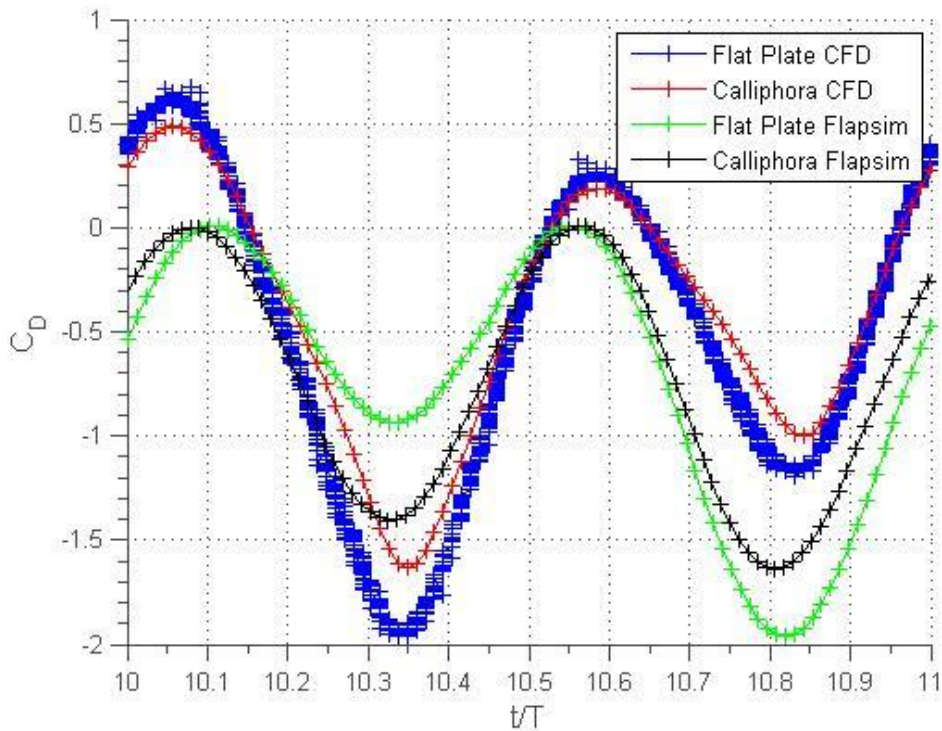


Figure 7.63 Comparison of Drag Coefficient for the First Case 10th period ($A=41.52$
 $^\circ$, $f=11.2$ Hz) in Hover due to Span-wise Wing Shape

7.5 Discussion

The present analytic model for flapping wings depends on unsteady panel method and capable of calculating pressure forces on the wing section and the moment about the quarter chord of the airfoil. The different airfoil shapes and motion kinematics are possible to analyze with the current study. Two linear velocities (parallel and perpendicular to the chord line) can be input as periodic or constant depending on the motion type. For example, the periodic motion defined in forward direction results in periodic sweeping motion.

The model is tested by comparing the results with the CFD Simulations given by Senol [41]. The same frequencies and amplitudes and wing parameters used as in CFD. The surface positions of the airfoil sections and wake points are updated during the motion period.

Results for two different periodic flapping motions (having different frequencies and amplitudes) are compared both in hover and forward flight. Since the force results obtained by the analytical model are pressure forces on the wing section, there are differences in the results mainly due to viscous effects, leading edge vortices and integration error. To explain these reasons; first the hover and forward flight cases were compared to understand the leading edge effect since leading edge vortices are expected to be stronger for hover case. As the airfoil section is rectangular and the angle of attack is zero, there occur leading edge vortices symmetrical to the trailing edge vortices. However, the leading edge vortices are not in the scope of this study. Therefore, it is expected to obtain nearly half of the result obtained by hover cases in CFD and the result of comparison was as expected.

In Figure 7.64, the clock-wise (green) and counter clock-wise (red) wake vortices are illustrated for 1 flapping cycle by the vorticities obtained by CFD simulations due to Equation 7.6. If there is no free stream for flapping motion, the free wake distribution is nearly symmetric on leading and trailing edges. Therefore to develop the analytic code, first the leading edge vortices have to be taken into consideration for pure plunging case. However, as seen in Figure 7.65, for the forward flight case the trailing edge vortices are dominating. Therefore, the performance of panel method is higher for high speed forward flight compared to hover cases.

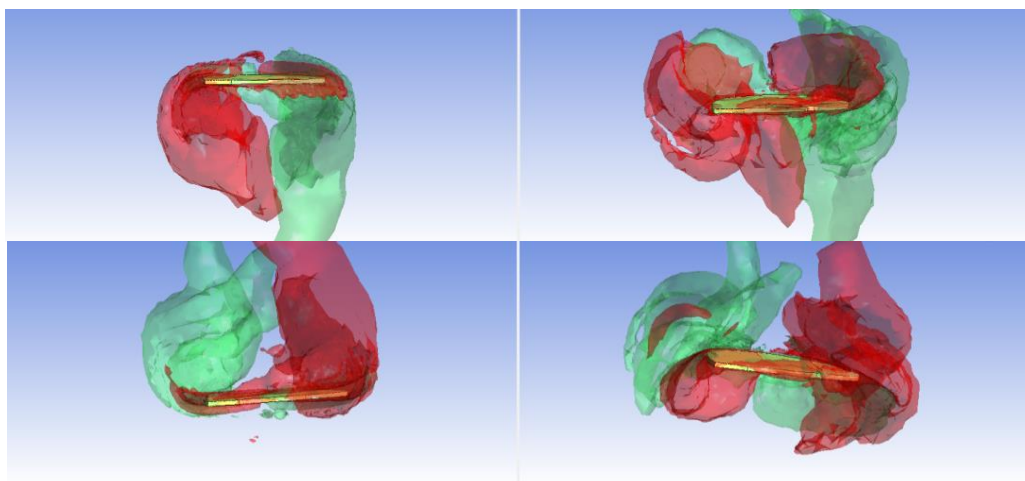


Figure 7.64 Iso-vorticity contours for hover visualized by CFD (green: cw, red: ccw)

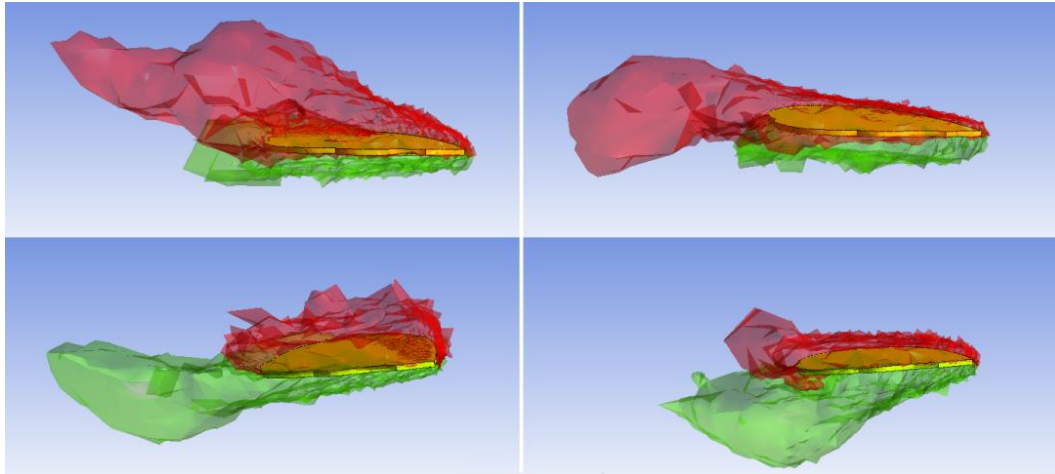


Figure 7.65 Iso-vorticity contours for forward flight visualized by CFD (green: cw, red: ccw)

$$\gamma_X = \hat{i} \left(\frac{dv}{dz} - \frac{dw}{dy} \right) \quad (7.6)$$

In forward cases, both the lift and drag graphs are closer to the CFD results compared to hover cases. Although the lift has periodic graph oscillating around zero as in hover cases, the drag has oscillations totally in positive side both in CFD results and the analytic model. This means the drag values are shifted by a positive value due to forward motion of the wing.

Second, to understand the effect of integration error, the results for different numbers of span-wise sections are compared. For the lift graphs, more the number of span-wise stations used in integration, closer the results are to the CFD Simulations. The chord length does not have strong effect on the results; however, all the stations have different linear velocities. Since execution speed is important for a model to be used in control applications, analyzing with more number of sections than 11 is thought not to be required.

When all these factors are taken into consideration although the lift forces show similarity, the differences in drag forces are difficult to explain. This is because, the viscous effect is stronger in horizontal direction as mentioned by the studies in the literature. In drag forces two peaks are observed. For hover cases, if the frequency is high, first peak in drag is obtained above, and second peak in drag is obtained under the CFD graph. However, if the frequency is low but amplitude is high, the drag

peaks both have equal peaks both in CFD results and results obtained by the current model.

Since there are many factors affecting the total force results, the analytic model has to be improved or the outputs can be tuned for the control applications especially for the hover cases. As can be seen from the visualization, the hover cases have dispersed flow patterns while the forward cases have regular mushroom-like patterns depending on wake- rollup algorithm included in the model. This is also affecting the results as the leading edge effect.

Comparison with flat plate wing shows that the reason of differences between results for different stations mainly is not the difference in chord lengths but the difference in linear velocities of different sections. Because, increasing the number of station for flat plate case, the results are closer to CFD results too.

Using ANSYS Fluent (2m dynamic mesh), unsteady data for 2-D pressure distributions, forces and moments are obtained. After comparing the force data, it is observed that although the lift value was more close to data gathered by CFD solver, the drag force was comparably very low. Therefore it was important to validate 2-D pressure distribution at a section and at a specific time on the wing. Because the idea was that since the drag force found by the present model is induced drag due to lift, which the corresponding component of force obtained by integrating pressure distribution on a 2-D surface, the difference could be due to parasite drag which is not calculated by this model. Hence, validating the sectional pressure distribution would provide validation of aerodynamic forces.

To do this, using CFD Post, comparison is made at sufficiently later period since initial periods are affected by impulsive start in CFD. For the first case ($f=11.2\text{Hz}$, $A=41.2^\circ$) the 10th period and for the second case ($f=5.82\text{ Hz}$, $A=82^\circ$) 4th period data are used. Loading all wing positions (0.005 sec apart) and defining iso-surfaces which are intersecting the wing walls at certain locations ($R=0.034745\text{ m}$, 0.054235 m , 0.073725 m) which are used by also Simulink model for 2-D sections to be integrated, the pressure distribution over a polyline of boundary intersections of iso-surfaces and wing walls are obtained.

Angular flapping is that the Flapping axis is fixed and allows only rotation; however, for linear motion, the wing is not rotating, but translating up and down. The two cases are obviously different for lift and drag production. Since the present model uses 2-D analysis and total force is found by span-wise integration, the angular flapping effect is provided by adjusting the linear velocities of 2-D sections depending on their span-wise locations.

The current model is also capable of changing the pitch angle during time period according to defined function; however, the cases for CFD results are all for constant angle of attack since the experimental mechanism used in the project does not have pitch control. Therefore, to follow same procedure, the fixed angle of attack is defined and the rate of change of pitch angle is taken as zero. Also since there is no free-stream for the hover cases, the velocity in x direction is also taken as zero.

For the comparison cases, since there is no time dependent pitching motion and the wing is a flat plate, while integrating pressure forces along the wing sections, there is no chord-wise component of normal vectors for upper and lower surfaces. Therefore the drag force is just obtained by sides of the wing sections and the lift force is obtained by upper and lower surfaces only. Because of this, the drag forces are also affected by the trailing edge re-shape procedure for satisfying the Kutta Condition.

CHAPTER 8

CONCLUSION

8.1 General Conclusions

In this thesis, an analytical model to calculate the unsteady aerodynamic force is developed and implemented on a single degree of freedom model that represents the roll dynamics in MATLAB / Simulink Tool. In addition, this model simulates the test setup which is designed to study the control by flapping wing mechanisms. The present analytic model uses unsteady panel method algorithm and span-wise integration of these 2-D results. The unsteady lift and drag force coefficients are verified with the CFD data obtained by ANSYS Workbench v14.0 Package Software.

The model developed is able to obtain the total forces for different kinds of wing sections (different NACA profiles), however; the main aspect of this thesis is to work with MAVs. Different cases are investigated using both Calliphora Wing Model and Flat Plate Model with 1mm thickness, having frequencies 11.2 Hz and 5.85 Hz, and amplitudes 41.52° and 85.90° .

The wing forces were obtained for two-wing system to analyze roll motion of the flapping body. Then the Rigid Body Dynamics equations were used to obtain body angular accelerations and velocities.

The solid model was designed by CATIA package software. Then each part of the model was cut by LASER machine. The mini servos were used to provide input motion to the flapping mechanisms. Total angular velocity and acceleration along the roll motion of the manufactured flapping body are aimed to be used to correct the instability along roll axis by the help of an IMU contains accelerometer and gyro

combination. The resultant instability is planned to correct by changing the frequencies and amplitudes of the motion of the wings during the runtime.

In addition, Instead of using sensors, the simulation outputs will be used for balancing the forces and moments at roll center.

The calculation method for Panel Algorithm and CFD Solver are totally different. The Panel Algorithm calculates only pressure forces on the wing; however, the CFD solver included laminar viscous effects too. Therefore, the more detailed comment on the results can be done by comparing more cases. However, in this study, also the pressure distributions are compared and verified with the explanations.

In this thesis, the study is limited to analysis of trailing edge wake vortices since unsteady panel method algorithm is used. The effect of leading edge vortices are planned to be modelled for improvement in future studies which is very important especially for hover cases.

The comparison cases include pure plunge or plunge with forward velocity although the model is capable of other motions like periodic sweeping, pitching or combined motions like figure of eight motion. This is because, this study is a part of TUBITAK Project which is based on application of piezoelectric materials in flapping wing MAV design. Therefore, the input motions are determined due to piezoelectric actuator capability. Nevertheless, in further studies, other type of motions will be analyzed and the model will be improved.

Additionally, Calliphora and Flat Shaped wings are manufactured using plexi glass. However, in analytic model other types of wing sections (NACA profiles) can be analyzed to obtain pressure forces on the wing. However for future experimental tests with force sensors of manufactured flapping mechanism, the results are obtained for these rectangular (or modified rectangular) wing sections.

8.2 Recommendations for Further Studies

- Different software tools such as C++, FORTRAN or PYTHON can be used while modeling unsteady panel methods to obtain faster executions.

- A new aspect of the study can be conducted by combining both closed loop control algorithms with the current model.
- The wing dimensions can be optimized by using the present algorithm to manufacture efficient MAVs.
- In order to reduce the weight of the total body, different materials can be used to manufacture the flapping design.
- The control mechanisms can be developed to give inputs to the wing mechanisms in 3-Dimensions.
- The model can be improved due to aerodynamics interactions between right and left wings.
- Ground effect in flapping motion can be studied.

REFERENCES

- [1] Brodsky, L. M. (1988). Ornament size influences mating success in male Rock Ptarmigan. *Anim. Behav* 36:662
- [2] Spedding, G.R., Rosén, M., Hedenström, A. (2006) Variations in wing kinematics and wake signatures in bird flight experiments, *Journal of Biomechanics*
- [3] Rayner, J. M. V. (1979a). A vortex theory of animal flight. II. The forward flight of birds *J. Fluid Mech.* 91, 731-763.
- [4] Fogh W. T. (1973) Quick estimates of flight fitness in hovering animals, including novel mechanisms for lift production. *J Exp Biol*1973; 59:169–230.
- [5] Ellington, C. P. (1984). The aerodynamics of hovering insect flight. I. The Quasi-Steady Analysis, *Phil. Trans. R. Soc. Lond. B* 305, 1-15.
- [6] Osborne, M. F. M. (1950) *Aerodynamics of Flapping Flight with Application to Insects*
- [7] Kawachi K. (1981). An extension of the local momentum theory to a distorted wake model of a hovering rotor. NASA, TM 81258
- [8] Betteridge, D.S., Archer, R.D. (1974) “A Study of the Mechanics of Flapping Wings,” *Aeronaut Quarterly*, May, pp. 129-142.
- [9] Philips P.J., East R.A., Pratt N.H., “An unsteady lifting-line theory of flapping wings with application to the forward flight of birds,” *Journal of Fluid Mechanics*, Vol. 112, pp. 97-125.philipzargan

- [10] Beddoes, T. S. (1981), “A Wake Model for High Resolution Airloads,” Second International Conference on Basic Rotorcraft Research, 1985, Research triangle Park, North Carolina.
- [11] Zbikowski, R., (2002). On aerodynamic modelling of an insect-like flapping wing in hover for micro air vehicles. *Philosophical Transactions of the Royal Society A* 360, 273–290.
- [12] Ansari S.A., Zbikowski R., Knowles K. (2006), Aerodynamic modelling of insect-like flapping flight for micro air vehicles, *Progress in Aerospace Sciences* 42,129–172
- [13] M. J. Smith, (1996). Simulating moth wing aerodynamics: Towards the development of flapping-wing technology, *AIAA J.* 34, 1448
- [14] Kamali, R., & Ravesh, S. R. (2008). Numerical Analysis of MAV’s Flapping Wings in Unsteady Conditions.
- [15] Jiménez, R. A., & López, O. D. (2011). Computational Model for the Dynamic Analysis of a Two- Dimensional Airfoil with a Control Surface, 2011–3846.
- [16] Persson, P.O., Willis, D. J., Peraire, J. (2011). Numerical Simulation of Flapping Wings using a Panel Method and a High-Order Navier-Stokes Solver
- [17] Anmar, A. H. (2008). Computational Method for Unsteady Motion of Two-Dimensional Airfoil. *Journal of Engineering*, 14(4).
- [18] Mantia, M. La, & Dabnichki, P. (2011). Added mass effect on flapping foil. *Engineering Analysis with Boundary Elements*, 36, 579–590. <http://doi.org/10.1016/j.enganabound.2011.11.002>
- [19] Mantia, M. La, & Dabnichki, P. (2008). Unsteady panel method for flapping foil. <http://doi.org/10.1016/j.enganabound.2008.08.001>

- [20] Smith, M., Wilkin, P., Williams, M. (1996) The advantages of an unsteady panel method in modelling the aerodynamic forces on rigid flapping wings. <http://jeb.biologists.org/cgi/content/abstract/199/5/1073>.
- [21] Sunada, S., Kawachi, K., Matsumoto, A. and Sakaguchi, A. (2001). Unsteady forces on a two-dimensional wing in plunging and pitching motion. *AIAA J.* 39, 1230 -1237
- [22] Vest, M.S., and Katz, J. (1996), Unsteady aerodynamic model of flapping wings, *AIAA J.* 34, 1435
- [23] Vest, M.S., and Katz, J. (1999), “Aerodynamic Study of a Flapping Wing Micro-UAV,” 37th AIAA Aerospace Sciences Meeting and Exhibit, Reno, NV January 11-14,
- [24] Katz, J. and Plotkin, A. (1991). *Low-speed Aerodynamics: From Wing Theory to Panel Methods*. New York: McGraw-Hill, Inc.
- [25] Prosser, D.T. (2011) *Flapping Wing Design for a Dragonfly-Like Micro Air Vehicle*
- [26] Garrick, I. E. (1937). Propulsion of a flapping and oscillating airfoil. NACA report 567,419 427.
- [27] Theodorsen, T., (1935). General theory of aerodynamic instability and the mechanism of flutter. Tech. Rep. 496, NACA.
- [28] Wagner, H., (1925). Über die Entstehung des dynamischen Auftriebes von Tragflügeln. *Zeitschrift für Angewandte Mathematic und Mechanik* 5 (1), 17–35.
- [29] Syaifuddin, M., Park, H. C., goo N. S. (2006) Design and Evaluation of a LIPCA-actuated flapping device, *Smart Materials and Structures*, 5764
- [30] Ristroph, L., Ristroph, G., Morozova, S., Bergou, A. J., Chang, S., Wang, Z. J., Guckenheimer, J. (2013). Active and passive stabilization of body

pitch in insect flight Active and passive stabilization of body pitch in insect flight.

- [31] Cheng, B., & Deng, X. (2010). Near-hover dynamics and attitude stabilization of an insect model. American Control Conference (ACC), 2010, 39–44. <http://doi.org/10.1109/ACC.2010.5530672>
- [32] Chang, S., & Wang, Z. J. (2014). Predicting fruit fly's sensing rate with insect flight simulations. Proceedings of the National Academy of Sciences of the United States of America, 1–6. <http://doi.org/10.1073/pnas.1314738111>
- [33] Teoh, Z. E., Fuller, S. B., Chirarattananon, P., Prez-Arancibia, N. O., Greenberg, J. D., & Wood, R. J. (2012). A hovering flapping-wing microrobot with altitude control and passive upright stability. IEEE International Conference on Intelligent Robots and Systems, 3209–3216. <http://doi.org/10.1109/IROS.2012.6386151>
- [34] Fearing, R. S., Chiang, K. H., Dickinson, M. H., Pick, D. L., Sitti, M., & Yan, J. (2000). Wing transmission for a micromechanical flying insect. Proceedings 2000 ICRA. Millennium Conference. IEEE International Conference on Robotics and Automation. Symposia Proceedings (Cat. No.00CH37065), 2. <http://doi.org/10.1109/ROBOT.2000.844811>
- [35] Karásek, M., Hua, A., Nan, Y., Lalami, M., & Preumont, A. (2014). Pitch and Roll Control Mechanism for a Hovering Flapping Wing MAV. International Journal of Micro Air Vehicles, 6(4), 253–264. <http://doi.org/10.1260/1756-8293.6.4.253>
- [36] Orłowski, C., Girard, a., & Shyy, W. (2010). Open loop pitch control of a flapping wing micro-air vehicle using a tail and control mass. American Control Conference (ACC), 2010, (2), 536–541. <http://doi.org/978-1-4244-7427-1/10>

- [37] Yan, J., Wood, R. J., Avadhanula, S., Sitti, M., & Fearing, R. S. (2001). Towards flapping wing control for a micromechanical flying insect. Proceedings 2001 ICRA. IEEE International Conference on Robotics and Automation, <http://doi.org/10.1109/ROBOT.2001.933225>
- [38] Dickinson, M. H., Lehmann, F. O. and Sane, S. P. (1999). Wing rotation and the aerodynamic basis of insect flight. *Science* 284, 1954 -1960
- [39] Küssner H.G. (1936), "Zusammenfassender Bericht über den instationären Auftrieb von Flügeln (Summary report on the instationary lift of wings)", *Luftfahrtforschung* (in German) 13 (12): 410–424
- [40] Azuma, A., Watanabe, T. (1988). Flight performance of a dragonfly. *J. Exp. Biol.* 137, 221–252.
- [41] Senol, M. G., Comez F. Y., Kurtuluş D. F., Arıkan K. B. (2015) Testing of Flapping Wing Four-Bar Mechanism
- [42] Orłowski, C. T., & Girard, A. R. (2011). Modeling and Simulation of Nonlinear Dynamics of Flapping Wing Micro Air Vehicles. *AIAA JOURNAL*, 49(5). <http://doi.org/10.2514/1.J050649>
- [43] Güngör, B., Aker, B., Günay, G. Arıkan, K. B., (2013), "Özgün Uçan Robotların Geliştirilmesi" 4. Mekatronik Mühendisliği Kongresi (MeMÖK2013), Atılım Üniversitesi, Ankara
- [44] Thomson, S. L., Mattson, C. A., Colton, M. B., Harston, S. P., Carlson, D. C., and Cutler, M., (2009), Experiment-Based Optimization of Flapping Wing Kinematics, 47th AIAA Aerospace Sciences Meeting and Exhibit, Orlando, Florida, AIAA Paper 2009-0874
- [45] Duan H, Qingwei Li (2009) Dynamic Model and Attitude Control of Flapping Wing Micro Aerial Vehicle, IEEE International Conference on Robotics and Biomimetics, Guilin, China.

- [46] L. Hines, D. Campolo, M. Sitti, (2010) Control Performance Simulation in the Design of a Flapping Wing Micro-Aerial Vehicle, IEEE/RSJ International Conference on Intelligent Robots and Systems October 18-22, 2010, Taipei, Taiwan
- [47] Deng, X., Schenato, L., and Sastry, S., (2004) Flapping Flight for Biomimetic Robotic Insects - Part II: Flight Control Design, Tech. Rep. UCB/ERL M04/34, EECS Department, University of California, Berkeley
- [48] Bhatia, M., Patil, M. J., Woolsey, C. A, Stanford, B. K., and Beran, P., (2014) "Stabilization of Flapping-Wing Micro-Air Vehicles in Gust Environments," Journal of Guidance, Control, and Dynamics, Vol. 37, pp. 592-607
- [49] J Zhang, B Cheng, JA Roll, X Deng, B Yao (2013) Direct drive of flapping wings under resonance with instantaneous wing trajectory control Robotics and Automation (ICRA), IEEE International Conference on, 4029-4034